IMPERIAL COLLEGE LONDON

GUIDED WAVE HEALTH MONITORING OF COMPLEX STRUCTURES

by

Thomas Clarke

A thesis submitted to Imperial College London for the degree of

Doctor of Philosophy

Department of Mechanical Engineering

Imperial College London

London SW7 2AZ

July 2009

Abstract

Structural Health Monitoring (SHM) systems are widely regarded as capable of significantly reducing inspection costs of safety-critical structures in industries such as aerospace, nuclear, and oil and gas, among others. Successful SHM systems can be considered those which combine good sensitivity to defects, preferably with the capability of localization and identification, with a low sensor density. Techniques based on sparse arrays of sensors which generate and receive guided waves are among the most promising candidates. Guided waves propagate over large distances and certain modes have the ability to transmit through a variety of structural features leading to a relatively small number of distributed sensors being able to cover the structure.

In complex structures, which contain high densities of structural elements, the time-traces obtained are often too complex to be directly interpreted due to the large number of overlapping reflections. In this case, the Baseline Subtraction technique becomes attractive. In this method a current signal from the structure is subtracted from a signal which has been acquired during the initial stages of operation of the structure. This eliminates the need for interpretation of the complex raw time signal and any defects will be clearly seen provided the amplitude of the residual signal obtained after subtraction of the baseline signal is sufficiently low when the structure is undamaged. However, it is well known that environmental effects such as stress, ambient temperature variations and liquid loading affect the velocity of guided waves; this modifies the time-traces and leads to high levels of residual signal if a single baseline, taken under different conditions, is used. Of these effects, temperature variations are the most commonly encountered and are critical since they affect not only the wave propagation but also the response of transducers.

The present work aims to demonstrate the potential of guided wave health monitoring of large area complex structures. It starts with a general literature review on inspection and monitoring of large area structures, in which the advantages and disadvantages of this technique compared to other well-established SHM techniques

are presented. The design and behaviour of two different temperature-stable transducers generating high A0 or S0 mode purity in the sub-200kHz frequency region are described. The efficiency of different signal processing techniques aimed at reducing or eliminating the influence of temperature on wave propagation is evaluated and a temperature compensation signal processing strategy is proposed. Finally, a large metallic structure is used to demonstrate a sparse-array SHM system based on this signal processing strategy, and imaging algorithms are used to combine the information from a large number of sensor combinations, ultimately leading to the localization of defects artificially introduced in the structure.

Acknowledgements

A number of people have contributed to my personal and professional development and to my well-being during this period.

My deepest thanks to Prof. Peter Cawley for his time, guidance and support, and for his unfaltering professionalism and devotion in his activities both as an academic and as a supervisor. My thanks to Prof. Mike Lowe for his dedication to the NDT group and for all the valuable discussions.

To all the people in the NDT Group, thank you for your companionship and support. My thanks to Francesco Simonetti, Frederic Cegla, Daniel Hesse for their help and openness, and to Jacob Davies, Ken Ma, Tino Cicero, Pierre Belanger, BuByong Kang, Prabhu Rajagopal, Giuseppe Sposito and Matthew Flemming for their friendship.

Many thanks to Prof. Stan Rohklin for his guidance and friendship, to Dr. Paul Wilcox and Dr. Anthony Croxford from the University of Bristol for their accessibility and for the fruitful collaboration, Dr. Paul Fromme for his valuable assistance in several occasions, and Prof. Jennifer Michaels from the Georgia Institute of Technology for the interesting discussions.

To the Brazilian Government agency CAPES for its vital support and to Mrs. Vanda Lucena for her zealous and excellent work.

For inspiration and for their unyielding support, I would like to thank my father, Prof. Robin Clarke, my mother, Prof. Nara Rosauro, and my little sister Julia Clarke.

Finally, I could not have ever come this far without the contagious happiness and strength of my haven, my wife Antonela - this thesis is dedicated to her courage and to her smile.

Contents

List of Figures

List of Tables

Chapter 1

Introduction

1.1 Motivation

The main objectives of non-destructive evaluation (NDE) are to improve the reliability, integrity and safety of critical industrial components, thus reducing the costs and the environmental impact of a catastrophic failure. NDE techniques in their various forms are crucial for the infrastructure, power generation, chemical and transport industries, and the use and applications of certain techniques are well-established. Technological development in the area means that new methods, based on the most varied natural phenomena, are constantly being incorporated in routine industrial inspection and becoming one of the "traditional" NDE methods.

In the last 10 years the ultrasound NDE method based on guided wave propagation in the 20-100kHz frequency region has seen a gradual transfer from scientific and technological development to the commercial and industrial environments. Successful commercial application was achieved by use of deployable arrays of transducers generating and receiving guided waves in pipelines and rail [4–7], allowing fast screening of these structures and evaluation of loss of cross sectional area, which is then complemented by one of the traditional techniques for exact sizing. Pipeline inspection with such equipment has become widespread and most large oil companies are developing protocols of usage. Pipes and rail are commonly called 1D

structures because they are much larger in the axial or longitudinal than in the other dimensions. In a simplified perspective, interpretation of signals in such structures is based on the conventional ultrasonic testing (UT) approach of attributing a recorded reflection to a feature, such as a weld or a support, or to a defect.

With the fast development of electronics and computation facilities, NDE is following the move of many other areas towards automation and elimination of time-consuming methods and procedures. This is where pipe and rail inspection with guided waves, and indeed other techniques such as PIGs, gained significance, since as well as allowing inspection of inaccessible areas of the structures from an accessible point, they eliminated the need for point-by-point inspections which are necessary with other traditional techniques. The area is now moving towards Structural Health Monitoring (SHM), which consists in having permanently attached sensors which can provide on-demand or continuous inspection of structures. This will save additional time and operator costs and will allow remote and inaccessible areas, such as buried or sub-sea pipelines, to be inspected. Guided wave inspection remains on the forefront of SHM, particularly of pipelines, due to its ability to cover large distances with good sensitivity to defects, thus leading to a small number of sensors and low cost.

However, the challenge of effectively inspecting 2D structures such as panels, where propagation through large areas is required, remains. This is mainly because reflections are received from all directions in the panel, increasing significantly the difficulty in identifying which signal should be related to which structural feature or determining the the exact angular position of a defect. Most real 2D structures are also significantly more complicated than pipes or rail in the sense that they have a high density of structural features such as ribs, rivets, welds, holes, etc. These cause the signals to be complex, with many overlapping reflections which cannot be interpreted in the same way as other ultrasound techniques.

With the move of NDE towards SHM in recent years, the inspection of 2D structures has also moved from the concept of detachable single unit arrays of sensors, such as those used in pipe and rail inspection, to that of sparse-arrays of permanently-

attached individual sensors which have the capability of transmitting and receiving guided waves omni-directionally and thus can triangulate to detect defects (similar to what is done in, for example, seismology, when locating the epicentre of an event from an array of monitoring stations [8]). For such a system to succeed it is necessary to develop robust signal processing strategies and transduction techniques, with the objective of eliminating the large amount of coherent noise obtained in signals from complex structures, so that defects are seen reliably. Locating defects also requires a significant amount of data processing when combining the information recorded by all transducer combinations in a sparse-array. These are the areas explored in this thesis as will be described in the next section.

1.2 Thesis outline

This thesis will follow the sequence of topics described below.

Initially a review of guided wave SHM and its application to inspection and monitoring of large area complex structures is given in Chapter 2.

Chapter 3 demonstrates the development and the behaviour of two temperature-stable piezoelectric-based transducers generating low-frequency, high mode purity A0 mode in the 20-50kHz range and substantially pure S0 mode in the 100-150kHz frequency range. This was done by finite element modelling of the transducers and the results were validated by experimental measurements. These were the transducers used to obtain experimental results shown in subsequent chapters of the thesis. The material of this chapter is the basis of a paper published in the IEEE Transactions in Ultrasonics, Ferroelectrics and Frequency Control [P2 in the list of publications].

Chapter 4 evaluates the concept of baseline subtraction, which is intended to eliminate the coherent noise coming from multiple overlapping reflections in structures with high feature density. Signal processing techniques aimed at eliminating or reducing the effect of temperature on signals are introduced and evaluated experi-

mentally; the influence of signal complexity on these methods was evaluated experimentally and additional analytic simulations were used to demonstrate the influence of mode purity. The techniques were tested on a real section of an airframe panel and the effectiveness of the system in detecting artificial damage in the panel was tested. The material of this chapter is the basis of a paper published in the Journal of Sound and Vibration [P1 in the list of publications].

Chapter 5 sees the application of the techniques investigated and proposed in Chapter 4 to a real large area complex structure in an uncontrolled environment. Finite element analysis was used to simulate propagation of each mode in the structure and their interaction with the main feature in the structure as a function of incidence angle; this supported experimental results and defined the most adequate mode for testing. The entire strategy of transducer attachment and array construction, and signal acquisition and processing was tested. Artificial defects were introduced at different locations and signals were acquired for this state of the structure. Imaging algorithms were used to combine the information from multiple transducer pairs in the sparse-array, and the capability of the system in detecting and locating defects was verified. The material of this chapter is the basis of a paper submitted to the IEEE Transactions in Ultrasonics, Ferroelectrics and Frequency Control [P3 in the list of publications].

Finally, the conclusions and major contributions of the thesis are outlined in Chapter 6.

Chapter 2

Structural Health Monitoring

A system which can provide reliable continuous or on-demand assessment of the integrity of a structure regarding the presence of defects of critical size, or preferably below critical size, is of clear importance for the continuity of production lines and safety of crucial structures. Application of such systems may result in the elimination or reduction of time-consuming manual inspections thus leading to significant reductions in maintenance cost. This inspection concept can be termed Structural Health Monitoring (SHM) and attention to this topic has been growing continuously, particularly in the aerospace industry, but also in the oil and gas, nuclear, shipping and civil engineering industries.

SHM systems are usually based on permanently attached sensors strategically positioned on vulnerable areas of the structure. To be successful and competitive, a SHM system should have good sensitivity to defects, preferably with the capability of detection and localization, with a small number of sensors [9]. Low sensor density is crucial since it defines the cost of the system; system complexity is also reduced and in some applications, such as in the aerospace industry, it is important because of the extra weight imposed by sensors and cabling. Wireless communication would be a way of significantly reducing the overall weight of the system but it is clear that the amount of transmitted data would be far more manageable if few sensors were used.

Figure 2.1: *Examples of possible applications of SHM systems (clockwise from top left) airframe, oil and gas storage tanks, shipping containers.*

Each SHM technique is based on the measurement of a given property of the structure and this is what usually defines the optimal relationship between coverage and sensitivity to a given type of defect. In general, the coverage area of each individual transducer is inversely proportional to the sensitivity to defects of the system and a compromise between the two effects is necessary when designing a sparse-array of sensors. An example of this are strain measurements which are effective in detecting large deformation of the structure (i.e. buckling), but if small cracks are to be localised a very dense array would be necessary. A few examples of SHM techniques currently being considered are strain gauges [10] and fibre optic Bragg grating sensors [11] measuring strain, vibration measurement based methods, often combined with fatigue life-time predictions [12, 13], acoustic emission [14] and ultrasound-based methods [15].

SHM techniques can be classified as active or passive depending on their operational strategy. Passive SHM systems are generally based on detecting changes in a chosen property which usually occur as a result of an event (e.g. strain [16] or acoustic emission [17]) or on monitoring an intrinsic response of the structure (e.g. vibration

monitoring in cyclically-operating structures [18, 19]). Active SHM systems differ from passive systems in the sense that an excitation is applied to the structure, causing a response which is then measured and evaluated (e.g. modal analysis methods based on excitation [20] or ultrasound [21]).

Guided wave SHM is an active technique which has many similarities with the passive acoustic emission method. Both are based on low frequency ultrasound waves which are known to propagate long distances in structures, often across several structural features, resulting in good coverage. Furthermore both techniques use a permanently attached sparse-array of piezoelectric-based sensors and both have their range of coverage restricted by structural complexity and environmental conditions. Acoustic emission is a well established technique which has been studied for many years, but interest in guided wave SHM of complex structures has increased significantly in recent years due to the commercial success of deployable systems for pipe and rail inspection and permanently-attached systems monitoring relatively small and simple plate-like structures [4–7, 22].

This chapter will start by a brief review of acoustic emission SHM where the advantages and disadvantages of the method will be identified and where the similarities with guided wave SHM will be described. A general review of work on large area inspection with guided waves will follow. Finally, work on guided wave monitoring of complex plate-like structures with sparse-arrays will be reviewed and the different approaches used by different authors regarding the processing of signals will be presented.

2.1 SHM techniques based on low frequency acoustics

2.1.1 Acoustic emission SHM

Acoustic emission (AE) is energy in the form of elastic waves which is released when a material is deformed. Initially it was associated with crack growth within the material but it was later found that many other events could also be a source of elastic waves [1]. Some examples are corrosion in metals [23], delaminations in composites [14] and fracture and friction in most materials [1]. The NDE technique which is based on attempting to detect such events with sensors has been studied for over 40 years and it has widespread application in many areas, with well established protocols of usage. The method is attractive because it can be applied to structures with limited access and it can cover long distances even in complex structures. Examples of this are that AE systems have been employed on aircraft structures for almost 20 years [24] and by the Royal Air Force to monitor events during pressure testing of aircraft [25, 26]. AE has been applied in monitoring of pressure vessels detecting discontinuities, in aerospace to detect fatigue failures and in monitoring of numerous sorts of materials behaviour [1], and reports on the effectiveness of the technique in detecting the defects of interest in each case vary significantly from one author to another.

The AE system will usually consist of an array of piezoelectric sensors distributed throughout the structure. When an event occurs within the structure, it will be detected by a number of sensors of the array and will be flagged if its amplitude is above a pre-determined threshold level. Figure 2.2 shows the damped sinusoid which can be used to represent a sudden acoustic emission [1], which in this case is detectable above the trigger (or threshold) level; it also shows the level of noise which in this case would be sufficiently below the threshold level to allow detection of the signal. Once the signal is detected it is processed to give information on the location and identification of the source. Several parameters can be considered

in the processing stage: the maximum amplitude itself, the energy of the burst, the number of times a given burst crosses the threshold level (also called number of counts), signal duration or decay time, among others. Much of the early work on the subject was dedicated to characterization of defects by simple evaluation of changes in signal amplitude and shape of wave packets detected but more complex signal processing strategies can also be applied [27]. Figure 2.2 also reveals the main problem with the technique: often the source of the acoustic emission is a non-repeatable event and to ensure detection of such an event the threshold level must be low; such a low trigger level increases significantly the probability of false calls due to transient noise. In addition, the need for capture of a non-repeatable event means that simple methods of eliminating incoherent noise, such as averaging of signals in ultrasound, cannot be used and in most industrial applications the noise level is known to be high [1].

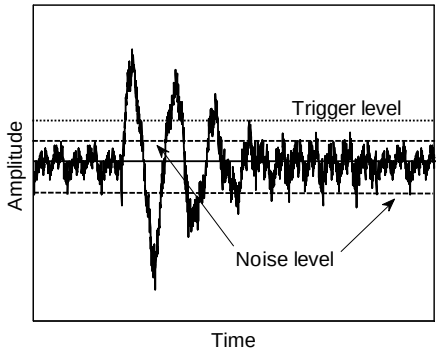

Figure 2.2: *Typical acoustic emission signal with pre-defined trigger level and background noise level [1].*

The elastic waves generated by an event within the structure propagate as guided waves as was shown in [28]. In this work the authors simulated acoustic emission signals by breaking pencil leads on the surface and on the edge of an aluminium plate; this is thought to be a satisfactorily way of simulating the sudden release of energy associated with crack growth. Differences in the arrival times of the signals were found depending on the position at which the lead was broken, the fundamental flexural (A0) or extensional (S0) modes being predominant when the lead was broken on the surface or on the edge of the plate respectively. Another study of the modes

involved in AE was made in [26]. Experiments were undertaken on a 1.2 mm thick aluminium plate, and waves were generated by lead breaks as in [28]. The authors also evaluated the frequencies in which the energy of the signals was concentrated. For both modes, the peak energy of the signal was at 65 - 70kHz with significant energy up to 600kHz for the S0 mode and only up to 100kHz for the A0 mode.

At this point it becomes important to understand each of the Lamb wave modes and their characteristic displacements. Figure 2.3(a) shows dispersion curves for flexural and extensional modes as a function of the frequency-thickness product up to 10MHz-mm. The results described in [26, 28] suggested that the energy of the signal arrivals recorded after lead-breaking at each position on the plate was concentrated below a frequency-thickness product of 1MHz-mm. Figure 2.3(a) shows that this is below the cutoff frequency of the A1 mode, where only the A0, S0 and the fundamental shear-horizontal mode (SH0) exist. The SH0 mode is not readily excited during acoustic emission, and the velocity of the arrivals during each lead-break made it possible to identify the other two modes. The S0 and A0 mode shapes are shown in Figure 2.3(b) at a frequency-thickness of 100kHz-mm. These mode shapes can be defined at each point through the thickness by their out-of-plane and in-plane displacement components. Constant in-plane displacement and negligible values of out-of-plane displacement are seen through the thickness of the plate for the S0 mode; for the A0 mode the out-of-plane displacement is close to constant through the thickness of the plate and some in-plane is found at the surface.

These modes are capable of propagating long distances, across several structural features, and are the reason for the good coverage obtained with AE in complex structures. An active technique could take advantage of this property by exciting these modes in the structure, and some of the disadvantages of AE could be reversed, as will be discussed in the next section.

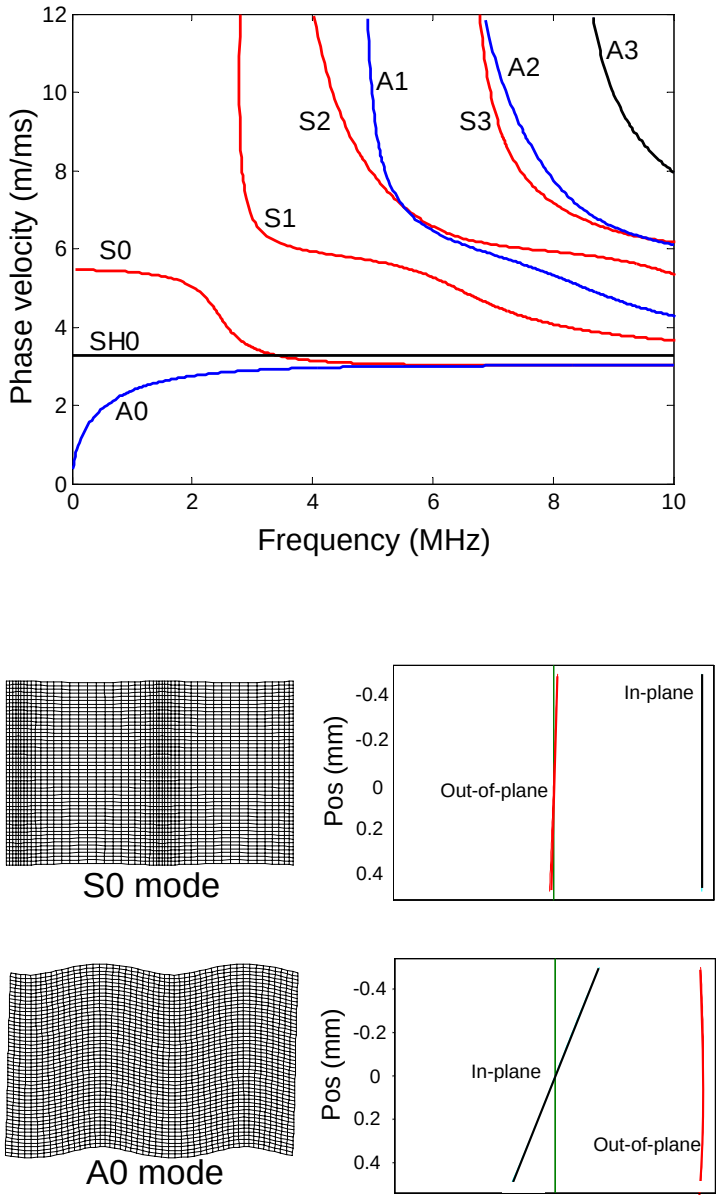

Figure 2.3: *(a) Dispersion curves for steel; (b) Modes shapes for the S0 and A0 modes at 100kHz-mm. Figures generated by the software DISPERSE [2].*

2.1.2 Guided wave SHM

Guided wave SHM is based on actively generating the the fundamental Lamb wave modes shown in Figure 2.3, in this way taking advantage of their long distance propagation in complex structures. Active excitation has many advantages: it allows control of mode purity which leads to considerable simplification of data processing compared to signals obtained with mixed mode excitation; the knowledge of the dominant mode allows the use of dispersion curves [29] which underpin a range of data treatment possibilities from precise time-to-distance conversions to dispersion compensation [30]. Signals are also significantly less complicated due to reduction in coherent noise [7, 31]. Another advantage of the active system is that it becomes possible for the operator to repeat measurements and confirm or not the detection of a defect; a transmitter can also be excited a number of times and the signals recorded at the receiver can be averaged, in this way eliminating incoherent or transient noise. The system can also operate on-demand or continuously; this is of particular importance if wireless communication is used since it increases substantially the battery life of each transducer, as opposed to the continuous operation of AE systems.

One of the traditional ways of generating a selected Lamb wave at a given frequency has been to have transducers whose length in the propagation direction is of 3-5 times the wavelength of the mode, which impose periodically varying forces, the period being the desired wavelength; examples of this are wedged piezoelectric transducers, some EMATs and interdigital transducers [7, 32]. The direction of the imposed forces is important, in-plane forces and out-of-plane forces being more effective in generating extensional and flexural modes, respectively. This technique is particularly useful when generating higher frequency modes, above the A1 mode cutoff frequency, where several modes exist. In the low frequency region, where the fundamental modes are present, the wavelengths are large and the transducer size becomes impractical [7]. However, wavelength controlled transduction is not necessary below the A1 mode cutoff frequency, because of the limited number of modes existing in this frequency region. This means that a point source generating a pure force on the surface of the structure in the direction of the predominant displacement

of the mode of interest is enough to generate each of the modes with high purity [33]. Piezoelectric sensors are very effective point-sources which can readily excite the A0 and S0 modes omni-directionally by exerting surface out-of-plane or in-plane forces respectively (see characteristic displacements for each mode in Figure 2.3). Chapter 3 will describe piezoelectric-based sensors generating both the A0 and S0 modes in this way.

An array of point-sources in a single unit can be used to simulate the behaviour of a single monolithic transducer [7]; this is important in pipe inspection, for example, where a ring with many transducers with the correct inter-element distance around the circumference can generate a circumferentially uniform wave propagating along the pipe. The successful commercial application of pipe inspection was highly influential in initial work on large area inspection; hence, several authors tested single-unit phased arrays [34–36] and good results were obtained in trials. The basic principle of these is that each element acts as a transmitter and receiver and if the response at all sensors is measured when each element in turn acts as a transmitter, synthetic focusing techniques can be used to "look" in each direction around the array.

In [34], a self-contained array of 32 receivers and 16 transmitters in concentric rings was used. This simulated the operation of a monolithic, wavelength selective guided wave transducer, operating in pulse-echo mode which is rotated through 360°. The transducers were non-contact pancake coil point-source EMATs producing omni-directional S0 mode at around 900kHz-mm. For validation, experiments on several plates with different thicknesses, surface finish conditions and artificial defects were undertaken. The sensitivity of the equipment allowed the authors to distinguish defects with half the plate thickness in depth and roughly three times the thickness of the plate in diameter. Another prototype of an array of transducers was designed in [35], this time exciting the A0 mode at frequencies below the A1 mode cutoff frequency, more precisely in the 500kHz-mm to 1.2MHz-mm range. It can be seen in Figure 2.3 that this mode at these frequencies is highly dispersive, but its much shorter wavelength compared to the S0 mode is an advantage since it improves

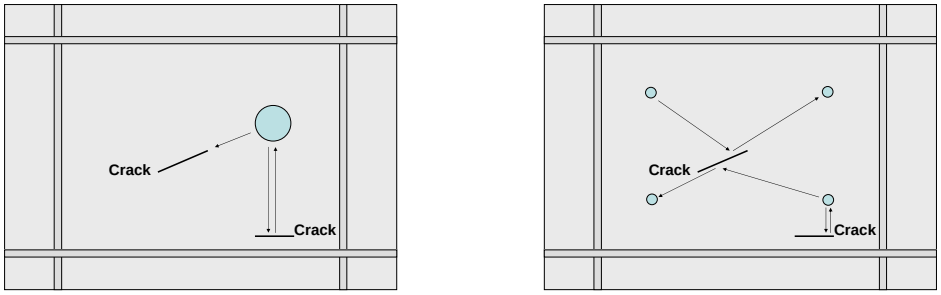

Figure 2.4: *(a) Single unit phased array; (b) Sparse-array.*

the resolution and sensitivity to defects. The system in [35] was designed to be permanently attached to the structure, while the previous was a detachable array. It consisted of 32 piezoelectric discs deployed in a circumference with 70 mm diameter. Results were also promising, and several different simulated defects were detected.

Several factors led to an increase in attention to health monitoring and permanently attached sparse-arrays of sensors. One of the advantages of having such systems is that while a permanently attached array would imply detection problems for defects in certain orientations (e.g. orientations parallel to the inspection direction), and in the case of a detachable array would require several different inspection positions to identify this defect, a sparsely distributed array would allow many different transmitter-receiver combinations, thus covering every crack orientation (see Figure 2.4). Also, an element in a sparsely distributed array is a single channel device which requires much less sophisticated electronics than the single unit arrays described above. In addition, a smaller number of sensors would be necessary to cover a given area. As described in [34], the beam steering for a single unit array requires the unit to be several wavelengths in diameter, and the exciting and receiving routines can be complex. A sparsely distributed array could work in triangulation and as few as three transducers could be used for a large area. Because of the already mentioned similarity with AE, it would be possible for the guided wave SHM system to operate actively, transmitting and receiving signals, or passively, just receiving signals produced by events within the structure.

Sparse-arrays of sensors generating and receiving guided waves have been successfully commercialised by Accelent Technologies, a spin-off from Stanford University. These systems consist of an array of piezoelectric elements mounted on a flexible printed circuit board (PCB) which can be embedded in a composite structure or placed on the surface of a small structure or a region of a large structure. This equipment has been applied to a few small and simple structures including solid rocket motor cases and liquid fuel bottles [22, 37]. The PCB has the advantage of being flexible and contains the electrical connections for the sensors, but the size of this flexible PCB sheet limits its application for large complex structures, which would each require a different array design.

Guided wave SHM with sparse-arrays has been investigated by several groups [38–47], the main difference between the systems tested being the signal processing strategy, which in general is aimed at improving the signal to noise ratio and the resolution and localization of defects. A considerable amount of work is based on the use of baseline comparison or subtraction. A baseline is a benchmark signal taken from the undamaged structure at initial stages of operation, when the presence of defects due to construction has been eliminated or acknowledged by use of conventional NDT techniques. Signals taken during inspection are compared to the baseline and any differences can then be attributed to a change in the structure (either the appearance of a new discontinuity or the growth of an existing defect). Baselines are of particular interest for monitoring of complex structures: signals from complex undamaged structures will usually consist of a large number of interfering reflections so the traditional ultrasound approach of identification of individual reflections, which can then be attributed either to benign structural features (e.g. stiffeners, welds, supports, etc.) or to defects, cannot be applied. In this case the large number of reflections from structural features is coherent noise which needs to be eliminated if defects are to found; theoretically, this can be done by subtracting a signal taken during inspection from a baseline. This will be discussed in detail in Chapter 4.

While some groups consider it fundamental [48] and advantageous to use baselines, since it can lead to detection of 1% reflectors even in complex structures if per-

formed adequately [9, 46], others consider it to be problematic, mainly due to its sensitivity to environmental changes, stressing and liquid loading of the structure. These effects cause variations of the elastic properties and density of the propagating medium, leading to changes in wave velocity which cause baselines taken under different conditions to be ineffective in reducing the coherent noise to levels below the amplitude of a reflection from a defect.

Methods to compensate for temperature effects exist and they are either based on a large and detailed look-up database of signals taken during initial stages of operation of the structure [9, 45, 46] which represent common environmental conditions of the structure, on synthetically compensating for the temperature-induced change in velocity [46, 49–51], and combinations of the two [46, 52]; Chapter 4 will introduce these techniques in more detail. Studies suggest stress [53] and liquid loading [54] can be compensated by the same techniques, but combinations of the three effects would lead to unrealistically large databases since many signals would be needed to cover all possible cases. Another environmental issue which could be detrimental to the effectiveness of the baseline approach is temperature gradients; however, a straightforward method of distinguishing a homogenous temperature change from a gradient is proposed in [55], which could allow the system to take measurements only at a given temperature distribution, and work leading to results presented in this thesis suggests gradients are minimum if sunlight exposure is avoided, either by night-time inspection or by protection of the structure (e.g. on-demand inspection of an airplane in a hangar).

Few alternatives to the use of baselines exist and their applicability to real structures and their effectiveness in locating defects are questionable. Some authors have proposed the use of time-reversal methods in which a wavepacket is transmitted between two sensors in pitch-catch and the arrival recorded at the receiver is reversed in time and sent back to the sensor initially acting as a transmitter [43, 44]. Theoretically, sending the time-reversed received signal back to its origin would reverse any changes imposed by the system to the original input signal, such as dispersion, transducer response and reflections from features, and if the input signal is exactly

reconstituted, the structure is considered to be undamaged; the system would rely on deviations in the shape of the initial signal to detect the presence of a defect. However, this method is far from being a practical solution to the SHM problem since to succeed, the complete signal recorded at the receiver, until energy is totally dissipated within the structure, needs to be reversed. Besides being inconvenient, the long acquisition time means the method is not instantaneous and temperature fluctuations could take place. As will be shown in Chapter 4, even very small temperature changes are enough to cause significant changes to the signals which would be disastrous for time-reversal methods, especially in structures with high density of reflectors. Experiments conducted on simple plates in laboratories, were conditions are practically constant, show that it is difficult to reproduce the input signal shape exactly [43,44]. It is also unclear how a change in shape of the reversed signal would help in locating a defect. Work in [56] also shows that reproduction of the exact shape of the input becomes significantly challenging as excitation frequency increases due to the frequency dependence of transduction efficiency; the authors also propose an alternative method based on synthetic time-reversal which is shown to work in an ideal demonstration experiment consisting of a large plate with an artificial defect. The method would however become impractical in a more complex structure with a real defect. However, when used in combination with baseline techniques this method gave interesting results concerning lowering of noise levels [57].

Imaging is an efficient way of combining information from the several transducer combinations available in a sparse-array. This improves the reliability of detection and localisation of defects compared to analysis of results from individual transducer pairs. Two imaging algorithms based on the time of arrival of reflections for each transducer pair ("ellipse algorithm" [58–61]) and on the difference in time arrival for combinations of transducers ("hyperbola algorithm" [59–61]) will be presented and applied to experimental results in Chapter 5. Examples of other imaging methods are the energy arrival method [62], which is a way of concentrating on the first reflection from the defect in order to avoid coherent noise from distant regions of the structure, and the RAPID method [63], which is based on attributing a coefficient based on the drop in correlation between a signal and a baseline, in this way

weighting the quality of the baseline subtraction to produce an optimised image.

Another pressing issue is the design of the sparse array in order to optimise transducer positioning to maximise coverage with a reduced number of sensors. Several approaches have been used including pattern recognition in the form of biologically-inspired algorithms based on Darwinian natural selection [64], evolutionary strategy [65] and other genetic algorithms [66]. In [9] a different approach is used which is based on the different geometries of the areas adequately covered by a sensor in pulse-echo or pitch-catch and also takes into account the reflection coefficient of the expected damage, the residual level after baseline subtraction with a temperature difference between the current signal and the baseline, and beam spreading effects. However, this method does not take into account the presence of features within the designated area and their angular-dependent reflection coefficient; as will be shown in Chapter 5 this could lead to poor detection capability even for transducers positioned in the vicinity of a defect.

This thesis will concentrate on the issues of temperature stable transduction of pure modes, evaluation of baseline subtraction and temperature compensation methods and the factors influencing their efficiency. From this study a signal processing strategy will be proposed. These findings will be associated with imaging algorithms, which will also be investigated and applied to data obtained in realistic conditions from a real complex structure.

Chapter 3

Transduction

3.1 Introduction

An important issue to be addressed if a functional guided wave SHM system is to be developed is mode selection and the appropriate transduction technique which will be used in order to excite a single mode. The excitation of a single mode simplifies the post-processing treatment of the data obtained because the received signals become increasingly complicated as the number of modes excited increases [31].

As will be shown in the next chapters, poor mode selectivity has a great influence on the effectiveness of signal post-processing techniques aimed at reducing the influence of environmental effects on signals, which are currently being considered for use in SHM systems [3, 46, 48–50]. Furthermore, the advantages of single-mode excitation, in particular the A0 mode, at low frequencies for post-processing techniques based on time-reversal of signals obtained in pitch-catch configuration are shown in [43], and it is clear that a transducer generating signals with these characteristics would be useful in work by other authors using the same technique [44]. A simplified method of generating high-purity A0 mode would also be useful for work shown in [67]. It was demonstrated in [68] that S0 mode wavefronts generated by deployable phased arrays of EMATs in the 100-200 kHz frequency region provided good coverage of large areas of plate-like structures; sparse array SHM systems could benefit from

the long-distance propagation of this mode, and a simple piezoelectric element-based transducer could generate signals with higher signal-to-noise ratio while using simpler electronics for excitation.

This chapter describes two different types of transducers which were used in experimental work described in the following chapters. The first transducer was designed to produce high-purity A0 mode at low frequencies; these results were presented in [61] and the transducer was used to obtain results published in [3, 46, 69, 70]. During the development stage of this transducer, a parametric study was undertaken through finite-element analysis. The influence of the dimensions of a backing mass and a soft front layer on the frequency-response function (FRF) of a piezoelectric disc was evaluated. It was also found that the thickness of the plate on which the transducer is operated is of great importance and these effects will be described in detail. The transducer diameter was the final dimension to be studied; the optimal diameter is strongly related to plate thickness and led to the need to establish the optimal transducer geometry for each plate thickness range of interest. Experimental results were used to verify the results obtained through finite-element analysis. The influence of temperature on the FRF of the transducer was evaluated and the excitation frequency which optimizes temperature stability of the transducer was defined.

The second transducer generates substantially pure S0 mode in the 100-150 kHz frequency region. This transducer was used in [9, 46, 70] and consists of a piezoelectric disc which is directly attached to the surface of the structure. The behaviour of this transducer was studied through finite-element analysis and experimental measurements, which also assessed its temperature stability.

Many of the parameters of the experimental procedures adopted will be found in the text of this chapter. Appendix B gives a more detailed description of the procedures.

3.2 A0 mode transduction

3.2.1 A0 mode selectivity and modification of the frequency-response of a piezoelectric disc

Mode selectivity is more easily obtained in the low-frequency region, below the A1 mode cut-off frequency, where there is a choice between the fundamental antisymmetric (A0), symmetric (S0) and shear-horizontal (SH0) modes. Of these, the A0 mode is the easiest to excite omni-directionally since a point-source exerting a pure out-of-plane force on the surface of the structure is sufficient to generate the characteristic displacements of this mode. It is also the mode which has the smallest wavelength for a given frequency in this frequency region, therefore offering better resolution to defects when compared to the S0 mode in the same frequency region; however the 20-35 mm wavelength of the A0 mode in the frequency range of interest on thin plates still imposes a limit on the size of defect which the system could detect. The A0 mode is highly dispersive at these frequencies but signal processing techniques can be used to compensate for dispersion effects [30]; furthermore, dispersion is not a major concern when SHM-oriented signal processing techniques currently under development are applied (baseline subtraction, compensation for temperature-induced change in wave velocity and time-reversal methods [3, 43, 44, 46, 48–50]). However, the mode has the disadvantage that its attenuation increases dramatically if the structure is fluid-loaded.

Excitation of guided waves is commonly achieved by use of piezoelectric elements (PZTs) because they are cheap, compact, are operated through relatively simple and inexpensive electronics, and generate signals with good signal to noise ratios. Such elements are especially effective in generating an omni-directional A0 mode since a simple disc-shaped piezoelectric element with through-thickness polarization and a diameter substantially smaller than its wavelength at the operating frequency can easily act as a quasi point-source generating the A0 mode at low frequencies. However, the force applied to the surface of the plate by a through-thickness po-

larized PZT element is not purely out-of-plane since Poisson's ratio effects lead to the exertion of radially polarized in-plane forces on the surface of the plate, causing excitation of the S0 mode in the structure. This effect should be suppressed if high mode purity is to be obtained.

The aim of this work is to design a transducer which can operate in the low frequency region (20-40kHz) since, as will be shown later, mode purity is more easily achieved at low frequency-thickness products. Generating waves with adequate amplitude at frequencies as low as these with an unmodified PZT disc is difficult because of the large wavelengths associated with this frequency region. Reasonably sized commercial discs have a through-thickness resonance at frequencies substantially higher than our target, and therefore have a poor response at low frequencies. Attempts to lower the through-thickness resonance of the disc make the size of the element impractical; for example, if a lead zirconate titanate ceramic disc, such as the one used in this work, is considered in the free-free state, to reach a through-thickness resonance frequency of 50kHz the thickness of the disc should be around 38 mm. It should also be noted that a common piezoelectric disc such as the one used in this work, which has a through-thickness resonance at around 1MHz, will give practically no response in the frequency region of interest (20-40kHz).

Backing masses are commonly used to modify the behaviour of a PZT element. A backing mass lowers the resonance frequency, although there is a limit beyond which this is ineffective [32], and also reduces the transducer bandwidth. Front layers are also widely used to modify the frequency-response of PZT discs. In [35], a thin soft rubber interlayer was used to suppress the transmission of the radial displacements of the disc which lead to the excitation of the S0 mode at resonance of a through-thickness polarized PZT disc. Soft front layers can also be used to provide electrical insulation from the structure and, as will be seen, to lower the resonance frequency of a PZT-backing mass system to even lower frequencies.

Backing masses and front layers were used to modify the behaviour of a piezoelectric disc in this work. A parametric study was carried out to determine the dimensions of each component needed to reach the low frequency resonance frequencies estab-

lished as a target, to generate high A0/S0 mode ratios and to generate signals with sufficient amplitude in different plate thicknesses. The idealised transducer geometry is shown in Figure 3.1 along with the dimensions which will be varied in the parametric study. For convenience, the thickness of the PZT disc used in this work was chosen to be 2 mm; however the same design procedure demonstrated here can be used to obtain similar results for discs of other dimensions.

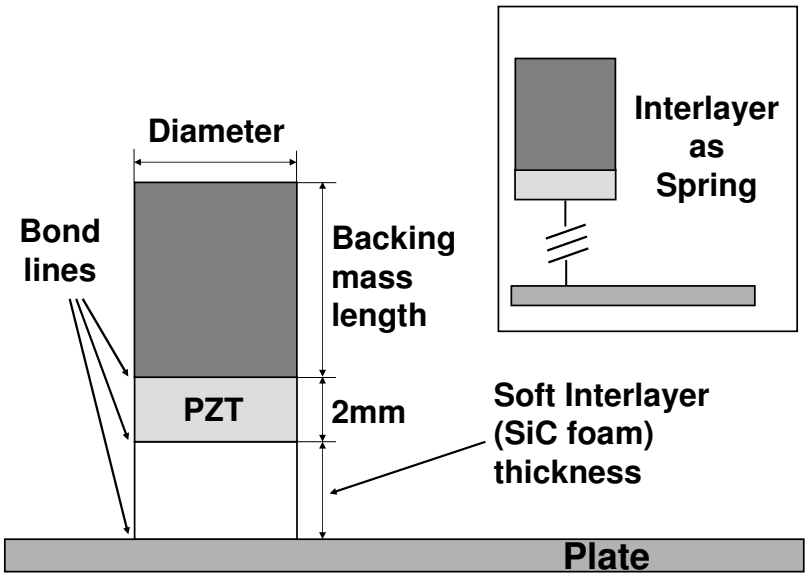

Figure 3.1: *Schematic diagram of idealised transducer geometry showing variables in parametric study and the system as a simple grounded spring-mass model.*

3.2.2 Modelling

Finite element analysis parametric study

The objective of the finite element (FE) simulations was to obtain the frequency-response function (FRF) of the system comprising the transducer attached to a plate, for different transducer geometries. The analysis was carried out in the commercial FE software ABAQUS in the steady-state dynamics mode. The model was built as an axisymmetric cross section of the system and the piezoelectric behaviour of the

element was included in the model. The input to the top face of the piezoelectric element was a potential of amplitude 1V at all frequencies, while the bottom face was kept at 0V (grounded). The frequency-response function in terms of displacement per Volt at different monitoring points in a plate of 1 m radius was obtained. Figure 3.2 shows a sketch of the model; the variables of the parametric study were plate thickness, interlayer thickness, backing mass length and transducer diameter. Table 1.1 gives the range of values used for each variable during the parametric study; the study was performed by changing one of these variables while holding the others constant.

Table 3.1: Values of variables in finite-element parametric study.

Variable	Measure (mm)
Plate thickness	1 - 30
Transducer diameter	0.5 - 180
Interlayer thickness	1, 2, 3
Backing mass length	3, 6, 12

By analysing the displacement frequency-response function at certain monitoring nodes in the plate, the resonance frequency of the system could be identified for each of the transducer geometries. Monitoring points were located at 5mm and at 500 mm from the transducer at the mid-thickness node in the plate, where the out-of-plane and in-plane displacements can be entirely attributed to the A0 mode and to the S0 mode (see Figure2.3), respectively, and on the top surface of the plate, to allow comparison with experimentally measured signals (as will be described in later sections). By normalizing these displacements by the characteristic power flow for each mode, which was taken from the commercial software DISPERSE [2], the ratio of the A0 to the S0 mode power flow could be obtained. The power flow of a mode indicates the rate of energy propagation along the structure; it is defined as the integral of the power flow density over the thickness of the plate, which in its turn is the product of the stress tensor by the velocity vector for each point through the thickness of the plate.

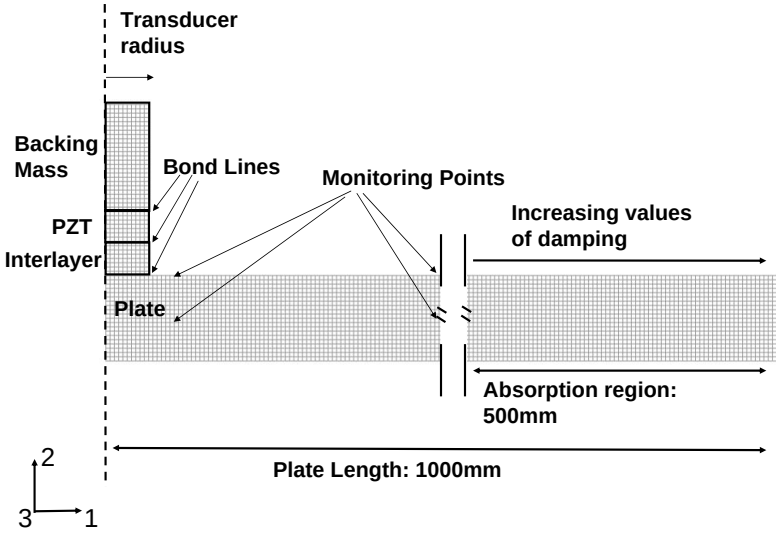

Figure 3.2: *Schematic diagram of transducer-plate system modelled in finite-element.*

To avoid reflections from the edge of the plate an absorption region was used as shown in Figure 3.2. This was implemented by modelling the outer region of the plate as a visco-elastic material with the same density and elastic properties as the material of the rest of the plate, but with increasing values of damping with radial position. The displacement amplitude of the wave will therefore diminish while it propagates towards the edge. The absorption region used had a total length of 500 mm. A more detailed explanation of absorption regions and the FE parameters used to generate such a region can be found in [71].

In all models the element used was 0.25 mm square with four nodes. This guaranteed good sampling of all wavelengths of interest. For both the transducer and the plate, linear elements were used to reduce computation time; the bond lines were modelled with a single line of quadratic elements of the same dimension and the material properties used in the bond lines were those of epoxy; the bond lines were therefore 0.25 mm thick. It was found that small changes in bond line thickness did not significantly influence the predictions. This is thought to be because the elastic properties of epoxy are similar to those of the interlayer material (see Table 3.2); a change in bond line thickness therefore had a similar effect to a small change in the

thickness of the interlayer.

Table 3.2: Material properties used in finite-element models.

	Material	Young's Modulus (GPa)	Density (Kg/m^3)	Poisson's ratio
Backing mass	Brass	108	8400	0.333
Interlayer	SiC foam	2.5	258	0.222
Bond lines	Epoxy	2.8	1200	0.345
Plate	Steel	217	7980	0.286
	Aluminium	73	2780	0.333

Material Properties

Table 3.2 gives the material properties used in models; the properties of the piezoelectric ceramic Pz27 (Ferroperm) which was used in the models and experiments are given in Appendix A. Brass was chosen as the material for the backing masses due to its relatively high density and silicon carbide foam (SiC, 8% relative density, 70-90 pores per linear inch (PPI)) was the material chosen for the interlayer. Besides being a good electrical insulator and having low stiffness, SiC foam has good thermal stability which is crucial if signal processing techniques such as baseline subtraction are to be used. It also has good mechanical resistance and experience shows that transducers built with it are sturdy; under impact the weaker region is the bond between the transducer and the plate. Plastic materials such as Polyoxymethylene (POM) were also tested as interlayers and gave adequate results although the temperature stability of transducers with such layers was poor and this material was finally discarded since stability is an important issue if baseline subtraction techniques are to be applied. The transducers were modelled attached to steel and aluminium plates (material properties shown in Table 3.2). Since the damping coefficients of the SiC foam are negligible, no damping was included in the interlayer in the FE models, but damping was included in the bond lines. For this, the values

of G_l / G_∞ = 0.3 and E_l / E_∞ = 0.3 were used, where G and E stand for the shear and Young's moduli respectively, and the subscripts l and ∞ stand for the loss modulus and the long-term modulus respectively (for further details see [72]; material properties obtained from [73]).

Simple spring-mass model

Given that the stiffness of the interlayer is significantly lower than that of the other components of the transducer and neglecting its mass, if we consider that the PZT and backing mass comprise a single point mass and that the plate has high flexural stiffness, the system in Figure 3.1 can be modelled as a simple spring-mass system on a rigid base whose resonance frequency, ω_n, will be given by:

$$\omega_n = \sqrt{\frac{E}{((\rho_{bm} l_{bm}) + (\rho_{pz} l_{pz}))t}} \tag{3.1}$$

where, E and t are the Young's modulus and thickness of the soft interlayer respectively, ρ is the density and l is the thickness of the backing mass (represented by the subscript bm) or of the PZT (represented by the subscript pz).

3.2.3 Parametric study: finite element results

Effect of backing mass length

Three different lengths of backing mass (3, 6 and 12 mm) on a 2 mm-thick, 5 mm-diameter PZT element were investigated. The interlayer thickness was kept at 2 mm and the aluminium plate thickness was 5 mm. Figure 3.3 shows the FRF of each transducer-plate system obtained by monitoring the out-of-plane displacement at the mid-thickness point of the plate at 5 mm from the transducer; a clear resonance can be seen in all cases. Dark vertical lines indicate the resonance frequency predicted by the grounded spring-mass system model, obtained from Equation 3.1.

The resonance frequencies of the systems obtained by FE analysis agree well with the values predicted by the simple spring-mass model, indicating that it describes the behaviour of the system adequately in these cases. It is interesting to note that the agreement between the two models is better for longer backing masses and as the mass is lowered in the FE model its behaviour can no longer be described by an ideal spring-mass system.

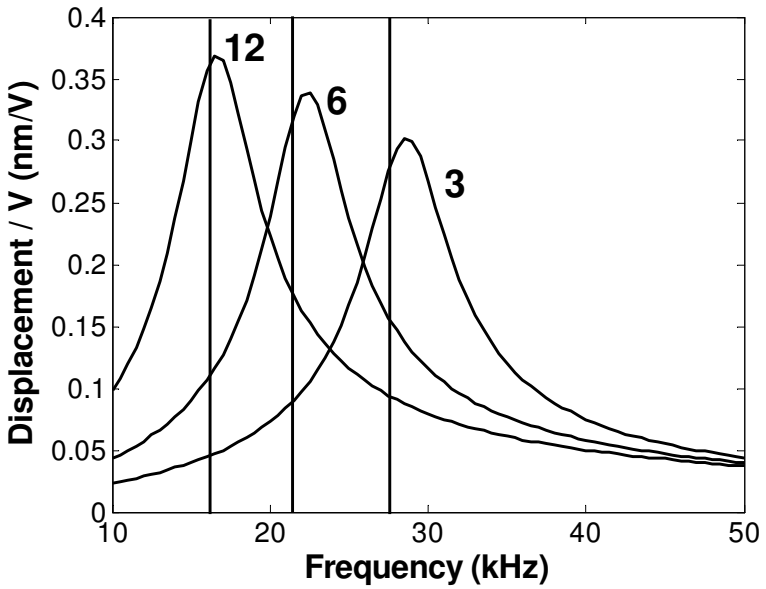

Figure 3.3: *Frequency-response functions for 5 mm-diameter transducers with a 2 mm-thick interlayer on a 5 mm-thick aluminium plate, with different backing mass lengths, shown in mm. Out-of-plane displacement monitored at 5 mm from transducer on the mid-thickness point of the plate. Vertical lines represent resonance frequency predicted by spring-mass system with equivalent vertical geometry.*

The thickness of the interlayer was varied so that 9 systems consisting of different combinations of backing mass lengths and interlayer thicknesses were obtained. The values of the resonance frequencies for each system are shown in Table 3.3; of these, the values for the transducer with a 6 mm-long backing mass fall within a reasonable frequency region if the target operating frequency is to be around 20-40 kHz. This was chosen as the ideal backing mass length and this was therefore the size used in all parametric studies shown in the subsequent sections.

Table 3.3: Resonance frequencies predicted by the simple grounded spring-mass system for varying backing mass length-interlayer thickness combinations.

Interlayer thickness	Resonance Frequency (kHz)		
	Backing mass length		
	3mm	6mm	12mm
1mm	39.5	31	23.3
2mm	27.9	22	16.5
3mm	22.8	17.9	13.5

Influence of interlayer thickness

The three different interlayer thicknesses shown in Table 1.1 were applied to transducers with a 6 mm-long backing mass and a 2 mm-thick, 5 mm-diameter PZT element, attached to a 5 mm-thick aluminium plate. Figure 3.4 shows the resulting FRF obtained for transducers with 1-, 2- and 3 mm-thick interlayers; the out-of-plane displacement was monitored at 5mm from the transducer at the mid-thickness point in the plate, and the vertical lines indicate the predicted values of resonance frequency for a grounded spring-mass with similar vertical dimensions. Again, the resonance frequencies predicted by the FE models agree well with the predictions of the spring-mass model; however, the agreement is better at low frequencies where stiffness is low, and as the stiffness of the interlayer is increased in the FE model its response deviates from the prediction of the spring-mass model.

Influence of plate thickness

Figure 3.5 shows the FRFs for systems consisting of a transducer with 5 mm-diameter and 2 mm-thick interlayers on different aluminium plate thicknesses. Again, the vertical dark line indicates the resonance frequency predicted by the simple grounded spring-mass model (22 kHz). It was clear from Figure 3.4 that the be-

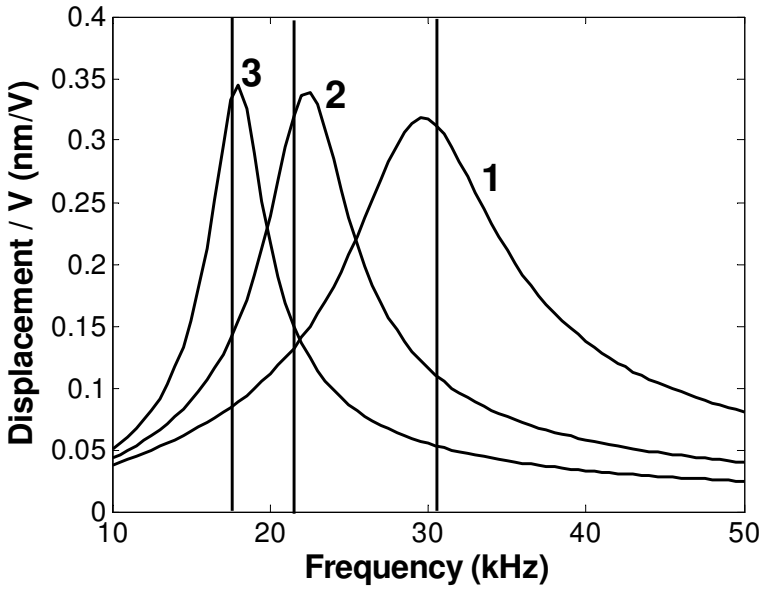

Figure 3.4: *Frequency-response functions for 5 mm-diameter transducers with a 6 mm-long backing mass on a 5 mm-thick aluminium plate, with different interlayer thicknesses, shown in mm. Out-of-plane displacement monitored at 5 mm from transducer on the mid-thickness point of the plate. Vertical lines represent resonance frequency predicted by spring-mass system with equivalent vertical geometry.*

haviour of transducers operating on a 5 mm-thick aluminium plate is well described by the spring-mass model; Figure 3.5 shows that as the plate thickness decreases the transducer-plate system behaviour starts to deviate from the predicted response of a spring-mass system on a rigid base: the FRF obtained on a 1 mm-thick aluminium plate has a very low Q and a resonance is seen at around 75-80kHz, beyond the range seen in Figure 3.5. The explanation for this is that as the plate thickness decreases, its rigidity decreases and so the base of the transducer is no longer effectively grounded, so invalidating the simple spring-mass model. The bandwidth reduced markedly as the plate thickness increases; it is undesirable to have very narrowband transducers as typical input signals have significant bandwidth (around 50%) and, as discussed below, their output tends to be more affected by temperature changes.

The effect of the flexural stiffness of the plate can be seen more clearly in Figure 3.6 which shows the value of the resonance frequency as a function of aluminium or steel

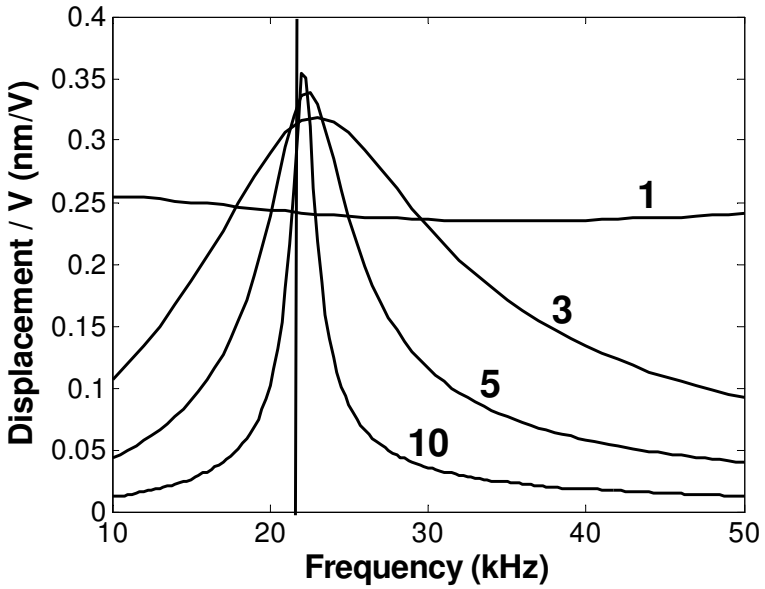

Figure 3.5: *Frequency-response functions for 5 mm-diameter transducers with a 6 mm-long backing mass, 2 mm-thick interlayer on aluminium plates of different thicknesses, shown in mm. Out-of-plane displacement monitored at 5 mm from transducer on the mid-thickness point of the plate. Vertical line represents resonance frequency predicted by spring-mass system with equivalent vertical geometry.*

plate thickness for transducers with different interlayer thicknesses. The horizontal lines indicate the resonance frequency predicted by the simple grounded spring-mass model computed for each interlayer thickness. The grounded spring-mass model is appropriate with aluminium plates over 5 mm thickness at all the interlayer thicknesses; with steel plates, convergence to the spring-mass resonance frequency is quicker, due to the higher modulus of steel which increases the flexural stiffness; the higher density also contributes to making the base of the system more massive and so a better approximation of "ground".

Mode Purity and the Influence of the Frequency-Thickness Product

The excitability of a guided wave mode is defined as the ratio of the surface displacement of the mode to the amplitude of the harmonic force generating it, the

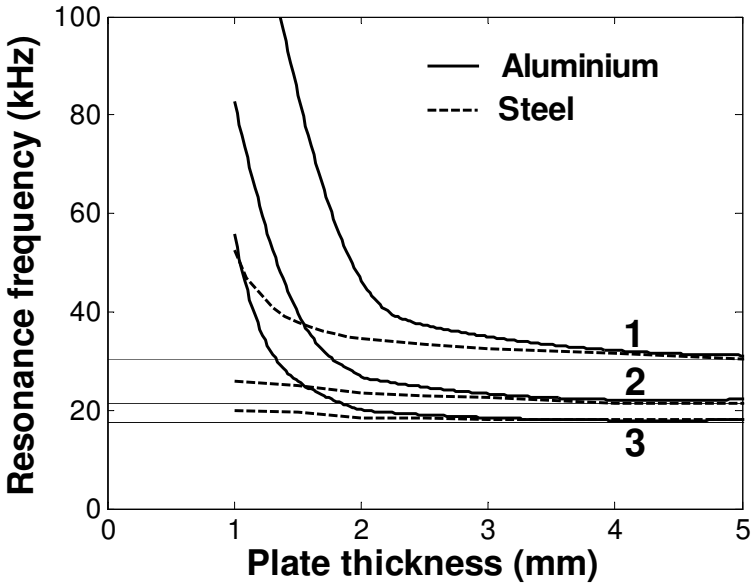

Figure 3.6: *Predicted variation in resonance frequency values of transducer-plate systems of different interlayer thicknesses (shown in mm) as a function of aluminium or steel plate thickness. Horizontal lines represent resonance frequency predicted by spring-mass system with equivalent vertical geometry. Transducer diameter:5 mm.*

displacement being measured in the same direction as the force. As shown in [33], the excitability of axisymmetric circular-crested Lamb waves by a pure out-of-plane point force (E_z) is given by:

$$|E_z| = \frac{k.\omega}{8} m_z^2 \tag{3.2}$$

where the subscript z stands for the out-of-plane direction, k is the wavenumber of the mode considered, ω is the angular frequency of the out-of-plane point force, and m_z is the power-flow normalized surface displacement component of the mode shape. In the low frequency-thickness region, below the cut off frequency of the A1 mode, the value of m_z for the A0 mode, which is the mode readily excited by an out-of-plane point force in this frequency region, increases rapidly with diminishing values of frequency-thickness product. Since the excitability of out-of-plane Lamb waves is proportional to m_z^2 it is clear that higher A0 mode excitability will be

obtained as the frequency-thickness product decreases, thus leading to higher A0 mode purity. Figure 3.5 showed that for most transducer-plate systems the resonance frequency of a spring-mass system of equivalent vertical geometry is the point at which maximum out-of-plane displacement generation in the plate is obtained; in the case where the transducer is operated on a 1 mm-thick plate and a flat response is obtained, any choice of excitation frequency in the frequency range considered would produce a similar displacement in the plate. The spring-mass resonance frequency was therefore chosen as a point of comparison between A0/S0 mode power flow ratios for different geometries of the transducer-plate system. Figure 3.7 shows the A0/S0 mode power flow ratio as a function of interlayer thickness for several aluminium plate thicknesses at the grounded spring-mass resonance frequency. Increasing values of interlayer thickness lead to lower values of resonance frequency, as predicted by the simple spring-mass system, and consequently higher mode purity. For comparison, a transducer with the same dimensions, but without the interlayer, on a 5 mm-thick aluminium plate would have a A0/S0 mode power flow ratio of 18 dB at the resonance of the system (100 kHz). The values shown in Figure 3.7, and indeed all values of A0/S0 mode ratios given in this work, are doubled if two transducers are used in pitch-catch due to reciprocity in transmission and reception.

Figure 3.8 shows an example of the deformed shape of a transducer when operating at the spring-mass resonance frequency. It is interesting that the interlayer is heavily deformed in the radial direction and this flexibility helps to limit the transmission of in-plane forces to the plate, so reducing the excitation of the S0 mode.

As it is important to keep the transducer as compact as possible, an interlayer thickness of 2 mm was chosen as this gives high mode purity and is thick enough for variations in the 0.1 mm-thick bond lines to have only a small effect on the resonance frequency of the system.

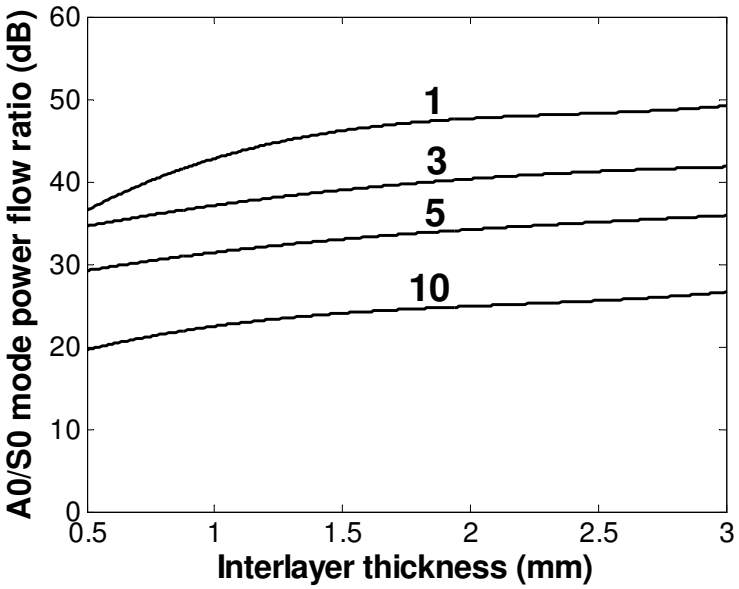

Figure 3.7: *A0/S0 mode power flow ratio at 22 kHz (resonance frequency of spring-mass system of equivalent geometry) as a function of interlayer thickness (shown in mm), for 5 mm-diameter transducers with a 6 mm-long backing mass on aluminium plates of different thicknesses.*

Influence of transducer diameter

Resonance frequency of the system

Figure 3.9 shows the resonance frequency of a transducer with 2 mm-thick interlayer and 6 mm-long backing mass as a function of the ratio between the transducer diameter (D) and the A0 mode wavelength (λ) at 22 kHz, which is the resonance frequency of a spring-mass system of equivalent vertical geometry (indicated by the horizontal line), on 3-, 5- and 10 mm-thick aluminium plates; for these plates, the A0 mode wavelength at 22 kHz is 36, 46 and 63 mm respectively. It was found that the ratio D/λ is a controlling parameter of transducer performance and the results are therefore plotted as a function of this non-dimensional variable. Figure 3.9 shows that the resonance frequency of transducer-plate systems of all plate thicknesses converges to that predicted by the spring-mass model at values below D/λ=0.1.

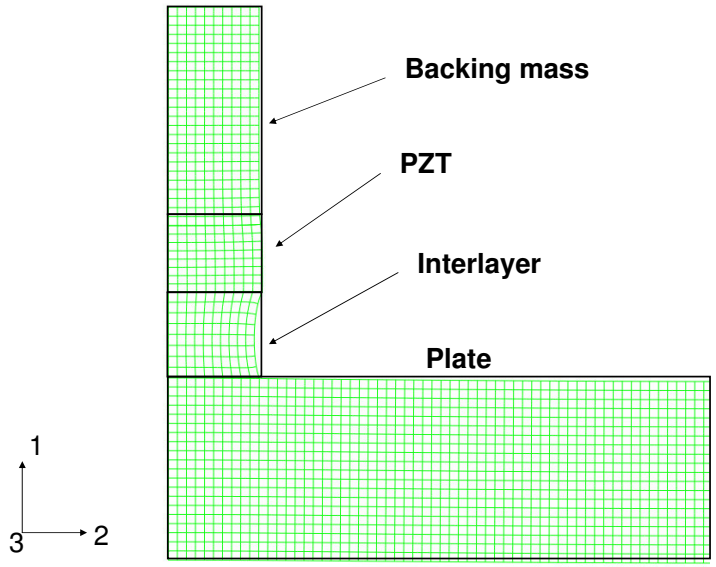

Figure 3.8: *Example of deformed shape of a 5 mm-diameter transducer with a 6 mm-long backing mass and 2 mm-thick interlayer on a 5 mm-thick aluminium plate at resonance frequency of spring-mass system of equivalent vertical geometry.*

This is consistent with the results of Figure 3.5 which showed that when a 5 mm-diameter transducer was used on a 5 mm-thick plate (D/λ=0.1), or on thicker plates ($D/\lambda < 0.1$), the resonance of the transducer-plate systems occurred at the same frequency as the resonance of a spring-mass system of equivalent vertical geometry. In thinner plates, the spring-mass model is not valid. Again this is consistent with the results of Figure 3.9 since the A0 mode wavelength at 22 kHz decreases with decreasing plate thickness. Hence, D/λ exceeds 0.1 and so is in the region where the resonance frequency is higher than the spring-mass prediction.

A0 mode amplitude

Figure 3.10 shows the variation of the A0 mode displacement amplitude generated in aluminium plates of different thicknesses by transducers of different diameter; the transducer diameter is again normalised by the wavelength of the A0 mode at the resonance frequency of a grounded spring-mass system of equivalent vertical geom-

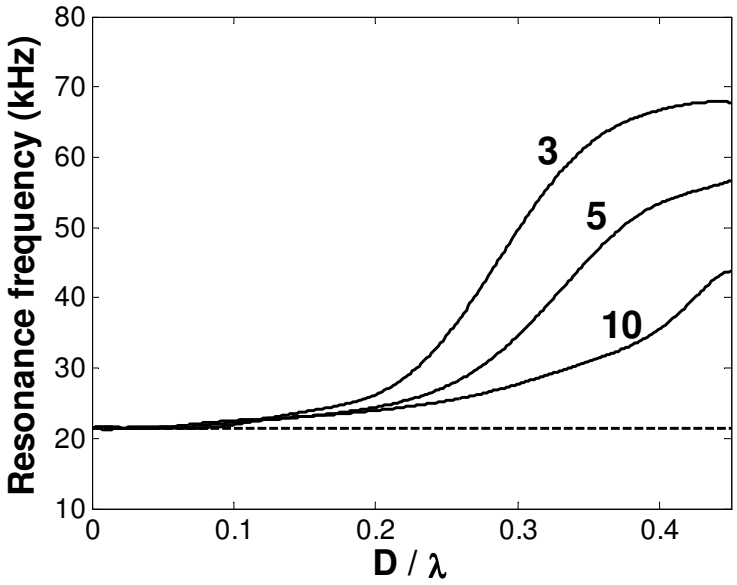

Figure 3.9: *Transducer-plate system resonance frequency as a function of the ratio of transducer diameter (D) and A0 mode wavelength (λ) at 22 kHz (resonance frequency of spring-mass model of equivalent vertical geometry) for different aluminium plate thicknesses (shown in mm). Horizontal line indicates resonance frequency predicted by a spring-mass model of equivalent vertical geometry (6 mm-long backing mass, 2 mm-thick interlayer).*

etry (22 kHz) and this is also the point of the FRF of each transducer-plate system at which the displacement is considered. The displacements were monitored at 500 mm from the transducer, at the mid-thickness point. In all curves in Figure 3.10 a displacement plateau is seen at D/λ values from 0.1 to 0.5. The values of displacement found on this plateau are lower for the 3 and 5 mm-thick plates; this is thought to be because at these D/λ values the transducer diameters are substantially higher in the 10 mm-thick plate case than in the other plates due to the larger A0 mode wavelength; the larger transducer generates a higher force which leads to a larger displacement, even though the plate is stiffer.

The large increase in displacement seen after the plateau is due to the first radial resonance, which occurs when the D/λ ratio is around unity. This can be seen in Figure 3.11 which shows the FRF obtained for transducers of 46, 58, and 74 mm-

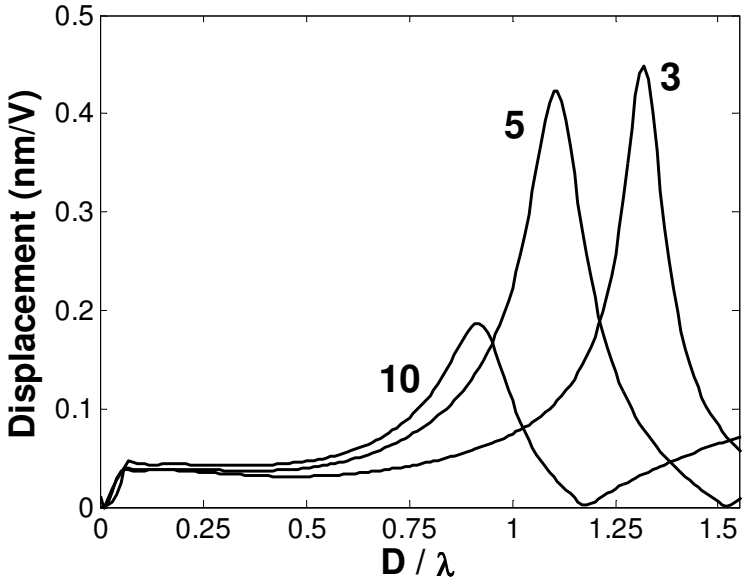

Figure 3.10: *A0 mode displacement amplitude generated by transducers with varying diameter on different plate thicknesses (shown in mm), monitored at 500 mm from transducer at the mid-thickness point of the plate, as a function of the ratio between the transducer diameter (D) and the A0 mode wavelength (λ) at 22 kHz (resonance frequency of spring-mass model of equivalent vertical geometry; 6 mm-long backing mass, 2 mm-thick interlayer).*

diameter on a 10 mm-thick aluminium plate (corresponding to D/λ =0.74, 0.93, and 1.2 in Figure 3.10, respectively). Only one frequency is considered in Figure 3.10, so λ is constant and the D/λ axis corresponds to varying transducer diameter only. In contrast, Figure 3.11 shows the variation of response with frequency at constant transducer diameter. The maximum displacement in Figure 3.10 occurs when the radial resonance of Figure 3.11 is 22 kHz; for a 10mm-thick plate, Figure 3.11 shows that this corresponds to a transducer diameter of 58 mm. The null point in Figure 3.10 occurs when the null of the frequency-response of Figure 3.11 occurs at 22 kHz, as can be seen for the transducer with D=74 mm in Figure 3.11.

The initial points of the displacement plateau of Figure 3.11 would be the preferred points of operation, since adequate displacement values are obtained with relatively small transducers. The mode purity is also higher at these points as shown in

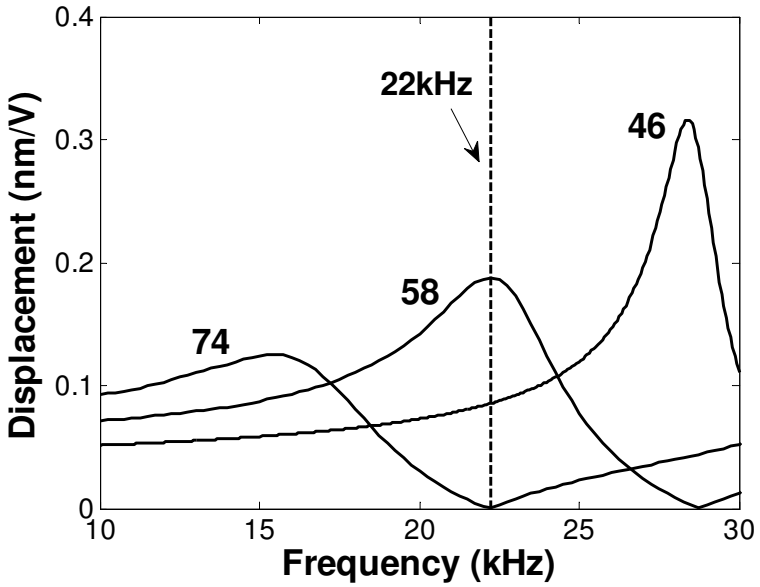

Figure 3.11: *FRF for transducers of different diameters (shown in mm) attached to a 10 mm-thick aluminium plate. Interlayer thickness is 2 mm and backing mass length is 6 mm.*

Figure 3.12, which shows the A0/S0 mode power flow ratio for 3-, 5- and 10 mm-thick plates as a function of D/λ. The effect of frequency-thickness is clear in this figure, with high mode purity being obtained for the 3 mm-thick plate and reductions in the A0/S0 mode ratio values occurring for each increase in plate thickness.

Bandwidth of frequency-response functions

Figure 3.13 shows the effect of the transducer diameter to A0 mode wavelength (at 22 kHz) ratio on the half power bandwidth of the FRF of the transducer-plate system for aluminium plates of 3, 5 and 10 mm thickness. The high bandwidths seen in Figure 3.13 are due to the strongly asymmetrical shape of the FRF in some cases. For example, a 9.5 mm diameter transducer on a 3 mm-thick aluminium plate has its peak response at 27 kHz and half power points at 2.1 and 71 kHz, giving a 255% bandwidth. The horizontal lines indicate the bandwidth of a 3-cycle and 5-cycle Hanning-windowed toneburst which are expected to be the most probable

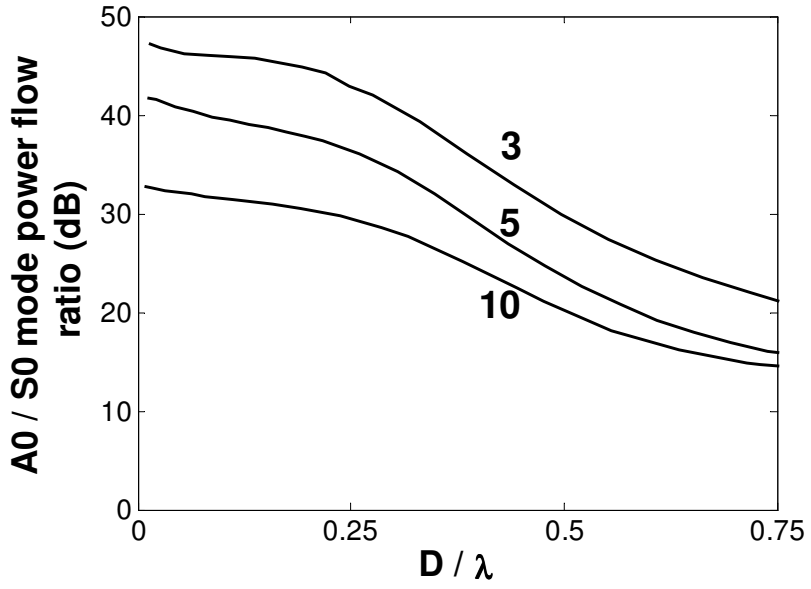

Figure 3.12: *A0/S0 mode power flow ratio, for displacements monitored at 22 kHz (resonance frequency of a spring-mass system with equivalent vertical geometry), as a function of transducer diameter (D) to A0 mode wavelength at 22 kHz (λ), for 3 mm-, 5 mm- and 10 mm-thick aluminium plates.*

input signals to a guided wave SHM system. It is desirable for the bandwidth of the FRF of the transducer to be at least as large as that of the input signal which precludes using very small diameter transducers. The temperature dependence of the transducers is also reduced with increasing bandwidth due to less rapid phase changes. Phase stability of signals is particularly important for SHM systems using temperature compensation techniques such as the Optimal Stretch and combinations of this with baseline subtraction techniques [3, 46, 49, 50]. Therefore, Figure 3.13 shows that for a 10 mm-thick plate, a D/λ value above 0.2 would be ideal, and lower values would be needed for thinner plates.

Final transducer diameter

The results shown in the previous sections show that the parameter D/λ is responsible for several effects which should be considered when choosing the final transducer

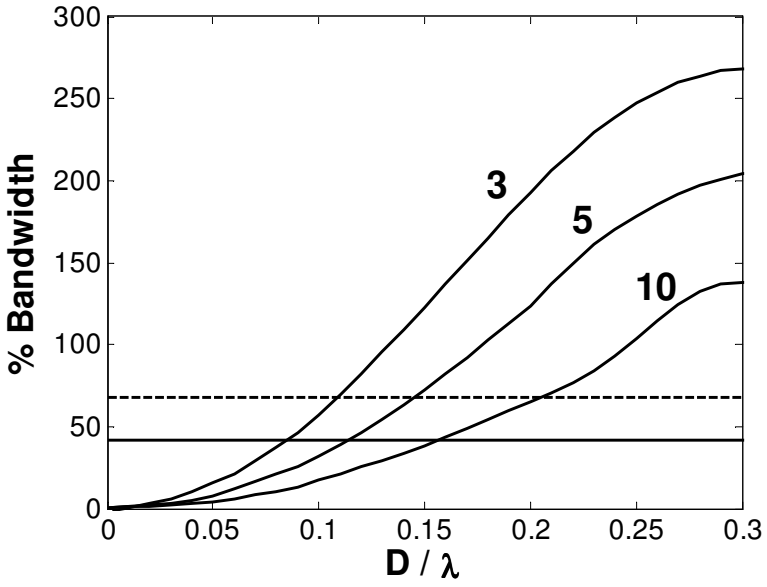

Figure 3.13: *Percentage bandwidth of FRF of transducer-plate systems, for transducer with 6 mm-long backing mass and 2mm-thick interlayer, as a function of the ratio of transducer diameter (D) to A0 mode wavelength (λ) at 22 kHz (resonance frequency of a spring-mass system with equivalent vertical geometry), on different aluminium plate thicknesses. Horizontal lines indicate bandwidth of a 3-cycle (dashed line) and a 5-cycle (solid line) Hanning windowed toneburst.*

geometry. It was seen in Figure 3.10 that increasing values of the D/λ ratio cause a slow shift from a well-defined plateau to a radial resonance in the vicinity of a D/λ ratio of unity, where large amplitude displacements are transmitted to the plate; this is then followed by a null in the transmitted displacement. In the plateau region, transmitted displacement values are relatively constant and transducer diameters are small; provided measureable signals are obtained with good signal-to-noise ratio, stability and smaller low-cost transducers are more important than increased transmitted power, so the plateau is the preferred region of operation. Moreover, as the D/λ ratio increases, the transducer mass becomes increasingly large while plate stiffness remains constant; there comes a point where the plate no longer provides a sufficiently stiff base for the simple spring-mass model to be valid (as seen in Figure 3.9). Again in this case, the low D/λ region is the preferred region of operation

since it is where the behaviour of the system can be easily predicted. Low values of D/λ also ensure that better A0/S0 mode ratios are obtained, as shown in Figure 3.12. The results above suggest that transducers in the range D/λ from 0.1 to 0.3 provide a good compromise of performance on the different criteria. This leads to different diameters for different plate thicknesses, the chosen values being shown in Table 3.4. It is important to note the added mass due to the large transducer diameters which are suggested for thick-plate structures (e.g. oil storage tank) is insignificant; smaller transducers are required on thin plate structures such as airplane fuselages where the weight will be an important issue. Figure 3.14 shows a transducer built with final dimensions and 6 mm-diameter on a 2 mm-thick aluminium panel.

Table 3.4: Chosen transducer diameter for different plate thicknesses.

Plate thickness range (mm)	Transducer diameter (mm)
1-5	5
5-10	10
10-20	20
20-30	25

3.2.4 Experimental validation of results

Experimental setup

The frequency-response functions obtained with FE modelling were validated experimentally using the setup shown in Figure 3.15. Transducers with a 2 mm-interlayer and a 6 mm-long backing mass were built and attached to 1-,3-, and 5 mm aluminium plates (5 mm-diameter transducers - see Table 3.4) and to 5- and 10 mm-thick aluminium plates (10 mm-diameter transducers - see Table 4) with epoxy adhesive (Hysol E-05CL). The same epoxy adhesive was used to assemble the different com-

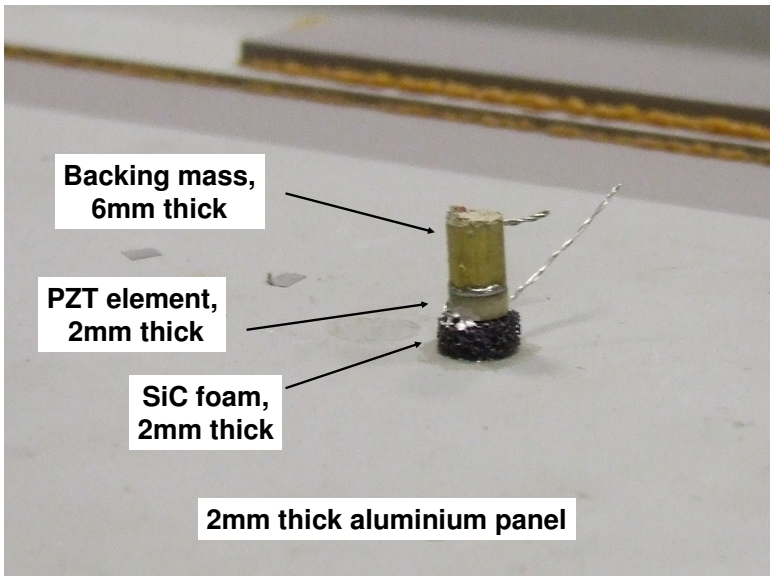

Figure 3.14: *Transducer built with final vertical dimensions and 6 mm-diameter on a 2 mm-thick aluminium panel.*

ponents of the transducer. Care was taken to maintain constant pressure on the transducer to ensure that bond lines as thin as possible were obtained. After a curing period of 24h, the transducers were temperature-cycled with a hot air gun; the maximum temperature the transducer was subjected to was 10°C above the expected operating temperature and the transducer-plate system was left to cool slowly. The cycle was repeated 3-4 times before tests were performed; this is necessary to avoid post-curing effects and to relieve residual stresses in the bond layers, which can cause changes in the response of the transducers over time [74].

The transducer was excited with a 5-cycle Hanning-windowed toneburst which was centred at frequencies between 10 kHz and 100 kHz, with 1kHz steps, which were uploaded from a PC and driven through a power amplifier (Krohn-Hite 7602) which gave 55V peak-to-peak signal. A laser vibrometer (Polytec) measuring out-of-plane velocity was focused at 5 mm from the transducer. This distance was chosen in order to ensure a clear first arrival at the laser point; when possible, signals were also measured at greater distances from the transducer and no difference in the

FRF was seen apart from loss of amplitude due to beam-spreading. The FFT of the signal obtained with this setup was taken, and the displacement spectrum was obtain by dividing the magnitude values of the velocity spectrum by their corresponding frequency value. The value of the displacement spectrum at the excitation frequency of each signal was then used to plot the experimental FRF.

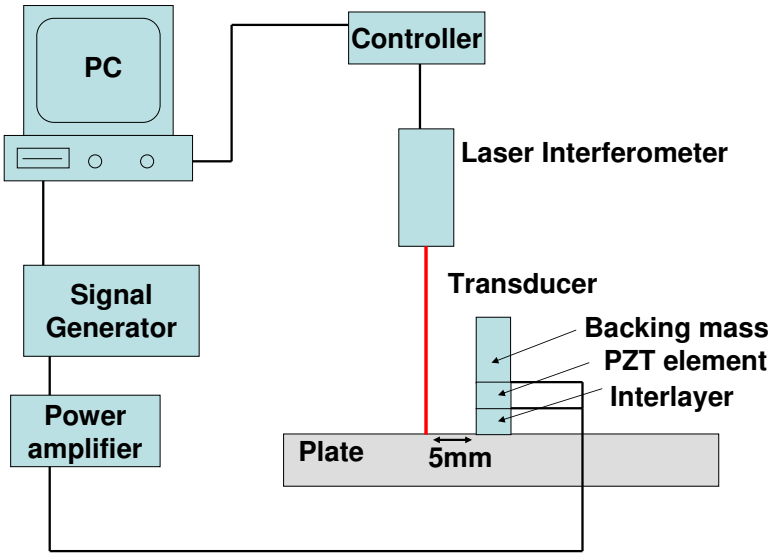

Figure 3.15: *Schematic diagram of experimental setup.*

Comparison between FE and experimentally-obtained FRFs

Figure 3.16 shows the results on the 1-, 3- and 5 mm-thick aluminium plate, with a 5 mm-diameter transducer, compared to the corresponding FE simulations. Good agreement was found in all cases. The experimental curves are slightly more damped than the predicted; this is probably because the bond lines were slightly thicker than those modelled and the adhesive is the main source of damping (apart from radiation damping resulting from excitation of the wave in the plate).

The corresponding results on the 5- and 10 mm-thick plates with 10 mm-diameter transducers are shown in Figure 3.17. Here the agreement with the FE predictions is excellent. It is interesting to note that the resonance of the 10 mm-diameter trans-

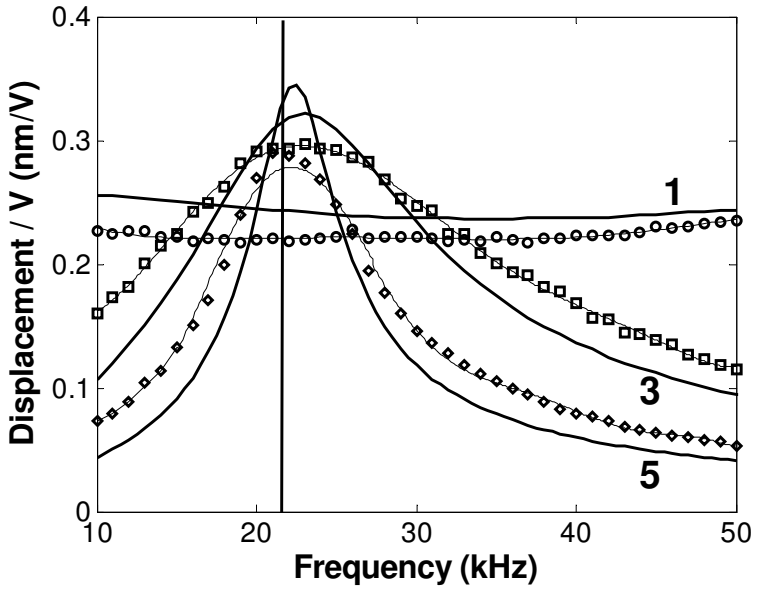

Figure 3.16: *Experimental (points with best-fit curves) and FE (lines) FRF for 5m m-diameter transducers, with 2 mm-thick interlayer and 6 mm-long backing mass, on 1-, 3- and 5 mm-thick aluminium plates. Displacement measured at 5 mm from transducer on the surface of the plate. Vertical line indicates resonance frequency of a spring-mass system of equivalent vertical geometry.*

ducer on a 5 mm-thick aluminium plate is at a frequency value above that predicted by a spring-mass model with equivalent vertical geometry. This agrees well with results shown in Figure 3.9, which shows a deviation from the behaviour of a spring-mass system for transducers with 10 mm-diameter on a 5 mm-thick aluminium plate (D/λ=0.22). Figure 3.9 also shows that a 10 mm-diameter transducer would behave according to the spring-mass model on a 10 mm-thick plate (D/λ=0.15), which is validated by the results of Figure 3.17.

3.2.5 Evaluation of the temperature stability of the A0 mode transducer

It was mentioned in section 3.2.3 that the bandwidth of the FRF of transducer-plate systems is an important issue for temperature stability. This is because phase stabil-

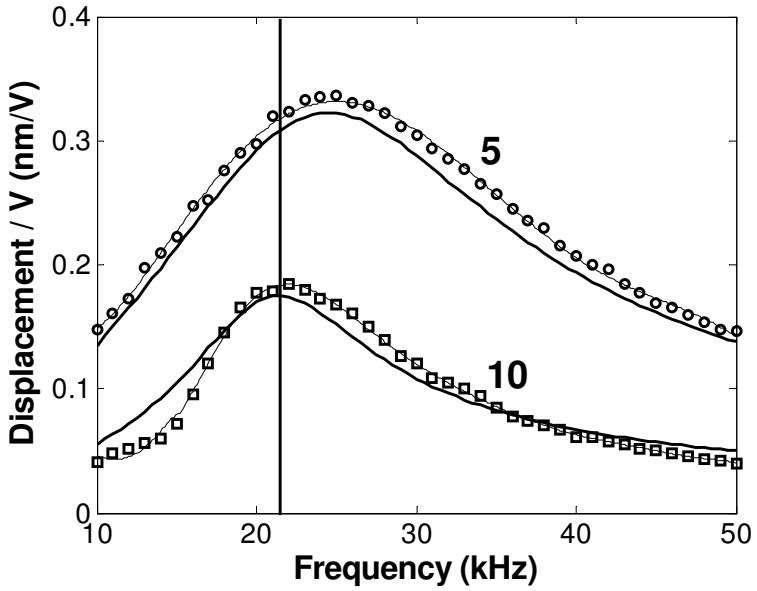

Figure 3.17: *Experimental (points with best-fit curves) and FE (lines) FRF for 10 mm-diameter transducers, with 2 mm-thick interlayer and 6 mm-long backing mass, on 5- and 10 mm-thick aluminium plates. Displacement measured at 5 mm from transducer on the surface of the plate. Vertical line indicates resonance frequency of a spring-mass system of equivalent vertical geometry.*

ity of the transducer is a key requirement of any of the signal processing techniques being considered for SHM, and systems with sharp resonances are likely to suffer temperature-induced phase shifts if excited in the near-resonance region. Therefore, to evaluate the temperature stability of the A0 mode transducer developed in this work, a transducer-plate system with a FRF with a relatively high Q-factor was chosen; this was a transducer with final vertical dimensions and 6 mm-diameter, attached to a 5 mm-thick aluminium plate. The frequency-response function (FRF) of the transducer was obtained by focusing a laser interferometer, measuring out-of-plane velocity, on the backing mass of the transducer and dividing the frequency content of the measured signal by the frequency content of the input signal. The temperature of the system was changed by placing a hot-plate underneath the plate and the temperature was increased from ambient to 40°C, with signals being recorded periodically.

Figure 3.18 shows the magnitude of the FRF obtained using this procedure at different temperatures; at room temperature the resonance of the system was at 22 kHz. When the temperature was raised to 30°C and 40°C an expected change in the FRF is seen in the vicinity of the resonance suggesting the occurrence of significant phase shifts. The shift in phase in the near-resonance region can be seen in Figure 3.19 although far more stable values of phase of the FRF are seen in the off-resonance region. It was found that operation at 35 kHz centre frequency caused minor amplitude variations to occur, which can be easily corrected for, and phase shifts were negligible. Excitation of the transducer in this frequency region also produced adequate signal amplitude in the structure, therefore giving a good compromise between stability and transmitted energy. Because of the slightly higher excitation frequency the A0/S0 mode power flow ratios shown in Figure 3.12 were usually reduced by 5-6dB, as will be demonstrated in the next section.

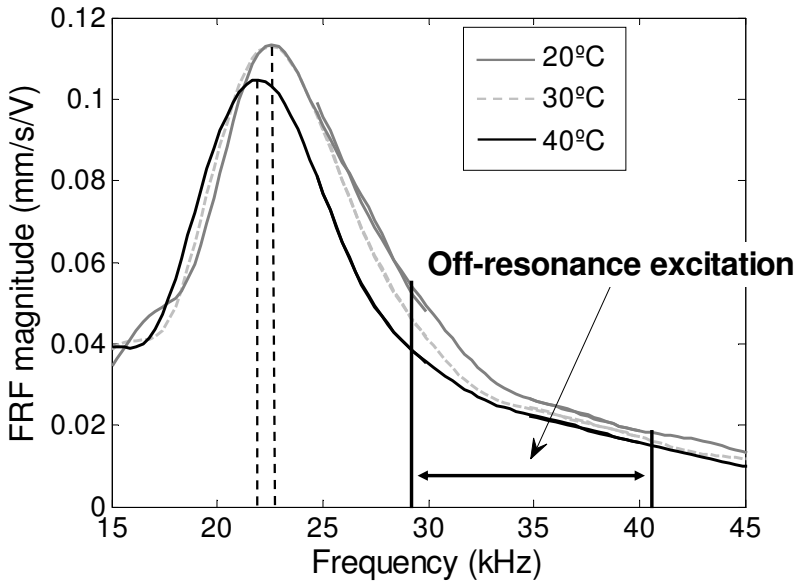

Figure 3.18: *Magnitude of frequency-response function of an A0 mode transducer with final vertical dimensions and 6 mm-diameter on a 5 mm-thick aluminium plate at 20°C, 30°C and 40°C.*

Obtaining good temperature stability of the transducer involved several steps which included selection of appropriate materials, adhesives and adjustment of the best

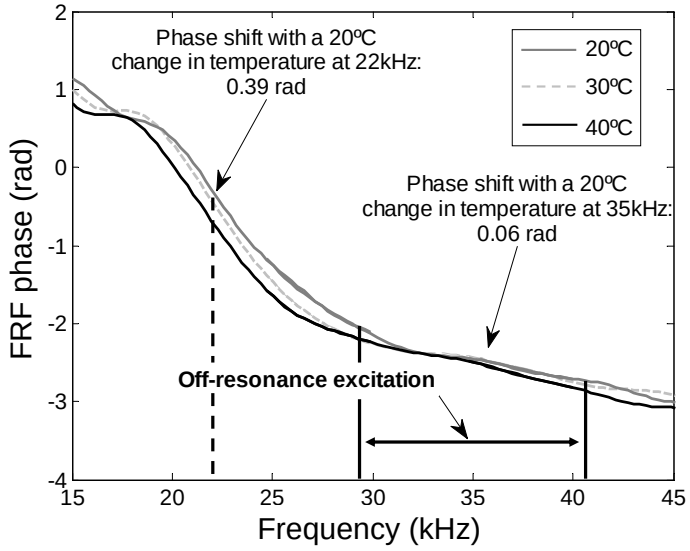

Figure 3.19: *Phase of frequency-response function of an A0 mode transducer with final vertical dimensions and 6 mm-diameter on a 5 mm-thick aluminium plate at 20º C, 30º C and 40º C.*

adhesive curing technique. Initially, a plastic (POM, Polyoxymethylene) was used as interlayer; this material provides good performance at ambient temperatures, is cheap, and is certainly an alternative for laboratory use. However, it has a low glass transition temperature (around 75°C) which led to significant changes in the FRF of the transducers when temperature was varied. Furthermore, common epoxy adhesives were used initially, but their fast curing meant that they became viscous and did not allow thin bond lines to be obtained. Several different polymers were tested but good temperature stability was not achieved, which led to the use of SiC foams, whose elastic properties are very similar to those of POM. High quality epoxy adhesives (Hysol E-05CL) were chosen due to their low viscosity and slow curing times, which allowed very thin bond lines to be achieved. The curing procedure was optimised by combining information from the supplier of the adhesive with literature on packaging of resonant MEMs [74], and conventional UT transducer design [75,76].

For repeatability of the assembly of the transducers, the main factor of influence was the thickness of the bond lines. It was found that by using a low-viscosity adhesive and by applying the same amount of pressure during curing of the bond lines, good

repeatability was achieved. Comparison of the FRF of transducers built showed that no variation was seen in the excitation region around 35kHz, but rather at the resonance of the system, although the shift in the position of the resonance did not exceed 1kHz, or less than 5% of the nominal value of the resonance (22kHz).

3.2.6 Experimental validation of A0/S0 mode ratio of designed transducer

Figure 3.20 shows the out-of-plane signal measured with a laser interferometer placed at 40 cm from a 5 mm-diameter transducer, attached to a 3 mm-aluminium plate, being excited with a 5-cycle Hanning windowed toneburst at 35kHz; a clear first arrival of the A0 mode is seen at the expected position, around 0.3ms. Even though the distance from the transducer was chosen as to allow the arrivals of the A0 and S0 modes to be distinguished due to their dissimilar group velocity, the S0 mode has very little out-of-plane displacement on the surface of the plate at this frequency and no signal is seen at the expected position of its first arrival (around 0.15ms). Figure 3.21 shows the signal recorded with a laser interferometer system measuring in-plane velocity at the same location. In this measurement a small signal is seen at 0.15ms; compared to the amplitude of the A0 mode first arrival, the amplitude of the S0 mode first arrival is very small since the in-plane displacement is characteristic of the S0 mode. Each arrival was windowed and the FFT of the resulting time-traces was obtained. The maximum magnitude of the spectra was divided by 35kHz, which was the frequency at which it occurred, to obtain displacement. Power flow normalised in-plane displacement values at the surface of a 3 mm-thick aluminium plate, obtained from DISPERSE [2] for the A0 and S0 modes at 35kHz, were used to estimate the A0/S0 mode power flow ratio for this case, resulting in a ratio of 42dB. Finite element results in Figure 3.12 showed that for a similar transducer on a 3 mm-thick aluminium plate, operated at 22kHz ($D/\lambda_{A0_{22kHz}}$=0.166), a A0/S0 mode power flow ratio of 47dB would be obtained. However, when the experimental setup described above is excited at 22kHz, the in-plane displacement signal in Figure 3.22 was obtained, from which a ratio of 48dB is found. This difference of 5-6dB in

the A0/S0 mode power flow ratio when the transducer is excited at 35kHz instead of 22kHz was seen in all cases and is explained by the resulting increase in the frequency-thickness product which, as seen in section 3.2.3, leads to a worsening of the mode purity.

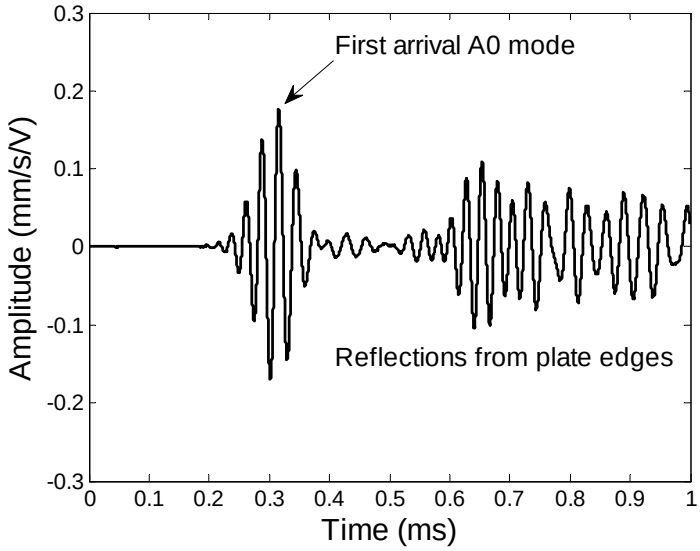

Figure 3.20: *Out-of-plane velocity time-trace obtained at 40 cm from a 6 mm-diameter transducer attached to a 3 mm-thick aluminium plate, at 35 kHz.*

3.3 S0 mode transduction

3.3.1 Finite element modelling

Transduction of the S0 mode at relatively high mode purity was obtained by use of a 20 mm-diameter, 1 mm-thick, PZT disc. This transducer operates in the frequency region where the diameter of the disc is comparable to the wavelength of the unwanted mode, where a sharp drop in the amplitude of the transmitted A0 mode is seen and the transducer gives relatively high S0 mode transmission. To show this effect, a disc with these dimensions was modelled axisymmetrically as described in section 3.2.2 attached to aluminium plates of several thicknesses. The out-of-plane and the in-plane displacements were monitored at the mid-thickness node of

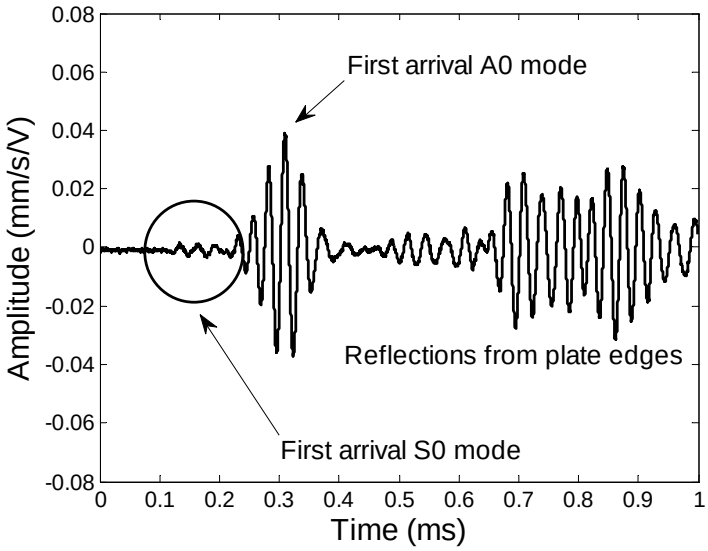

Figure 3.21: *In-plane velocity time-trace obtained at 40 cm from a 6 mm-diameter transducer attached to a 3 mm-thick aluminium plate, at 35 kHz.*

each plate, at a distance of 500 mm from the transducer; these displacements are characteristic of the A0 and S0 mode respectively and therefore could be used to obtain the FRF of each mode. The FRF in Figure 3.23 were obtained when the disc was attached to a 5 mm-thick aluminium plate. The drop in values of out-of-plane displacement is clear at around 150kHz following a resonance which is seen in the frequency region before the point where $D/\lambda_{A0}=1$. This is similar to the drop in A0 mode transmission seen in Figure 3.10 for the A0 mode transducer described earlier. The minimum in A0 mode transmission in Figure 3.23 will occur at different frequencies for different plate thicknesses due to the variation in wavelength of this mode with the thickness-frequency product. Therefore, for 2 mm- and a 3 mm-thick aluminium plates the ideal excitation frequency would be 100 kHz and 120 kHz respectively. This "tuning" of the transducer is similar to what was done in [43, 77] with PWAS sensors.

The same model as above, only without the absorption region, was used to evaluate the A0/S0 mode ratios obtained when a transducer is used as transmitter and receiver, simulating operation in pulse-echo or pitch-catch mode. Again, excitation

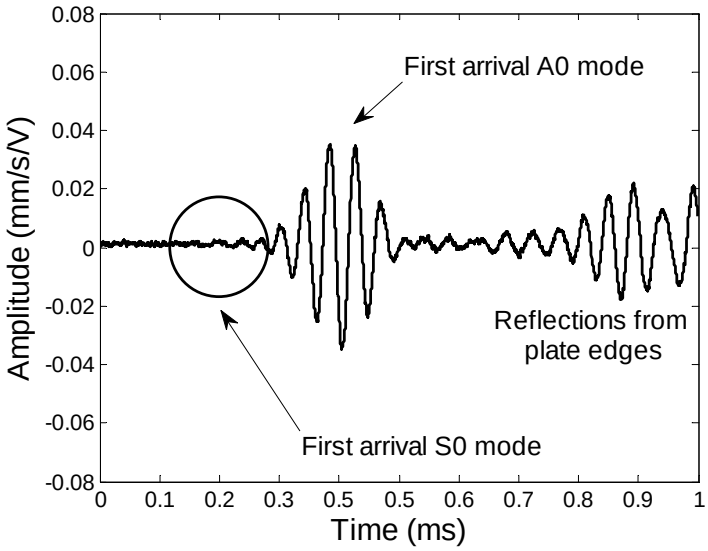

Figure 3.22: *In-plane velocity time-trace obtained at 40 cm from a 6 mm-diameter transducer attached to a 3 mm-thick steel plate, at 22 kHz.*

was achieved by applying a voltage signal to the top surface of the piezoelectric element while the bottom surface was grounded, simulating an experimental setup; the input signal was a 5-cycle Hanning windowed toneburst at different centre frequencies. The transducer generated a wave in the plate which was reflected at the edge and propagated back to the transducer. Due to the significant differences in velocity between the two modes and the large propagation distance involved, the reflection of the two modes could be separated in time and when these signals were received by the transducer a voltage time trace was generated; this was used to obtain the mode amplitude ratios. To avoid dispersion effects which cause a reduction of amplitude due to spread of the signals in time, the computation of the ratio was carried out in the frequency domain. The voltage time-traces obtained on a 5 mm-thick aluminium plate at 150kHz and 200kHz are shown in Figure 3.24. The first reflection from the edge to arrive is the S0 mode which has roughly the same amplitude at the two excitation frequencies, as was expected from the in-plane curve shown in Figure 3.23; the second reflection is due to the A0 mode and a substantial reduction in amplitude is seen for this wavepacket from 200kHz to 150kHz. For the setup modelled (5 mm-thick aluminium plate), the S0/A0 mode voltage ratio obtained

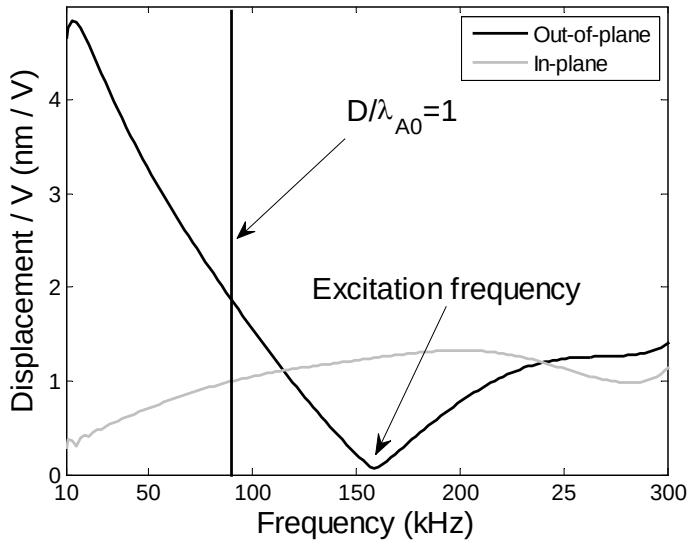

Figure 3.23: *Frequency-response function of a S0 mode transducer on a 5mm-thick aluminium plate.*

was 17dB and 8dB at 150kHz and 200kHz respectively. The 17dB ratio provides substantial mode purity although it is far below the value of 73dB A0/S0 mode voltage ratio obtained when a 6 mm-diameter A0 mode transducer was modelled in the same way.

3.3.2 Experimental results and temperature stability

To evaluate the signal produced by the S0 mode transducer, a setup similar to the one described in section 3.2.4 was used, the difference being that the laser vibrometer measuring out-of-plane displacement on a 5 mm-thick aluminium plate was placed at 30 cm from the transducer; this allowed enough propagation time to separate the wavefronts of the A0 and S0 modes generated by the transducer. Figure 3.25 shows the time traces obtained with this setup when the transducer was excited with 5 cycle Hanning windowed tonebursts at 150kHz and 200kHz; since there are very small values of surface out-of-plane displacement associated with the S0 mode, the wavefront of this mode has smaller amplitude than the wavefront of the A0 mode. As was done in section 3.2.2, power flow normalised out-of-plane displacement values

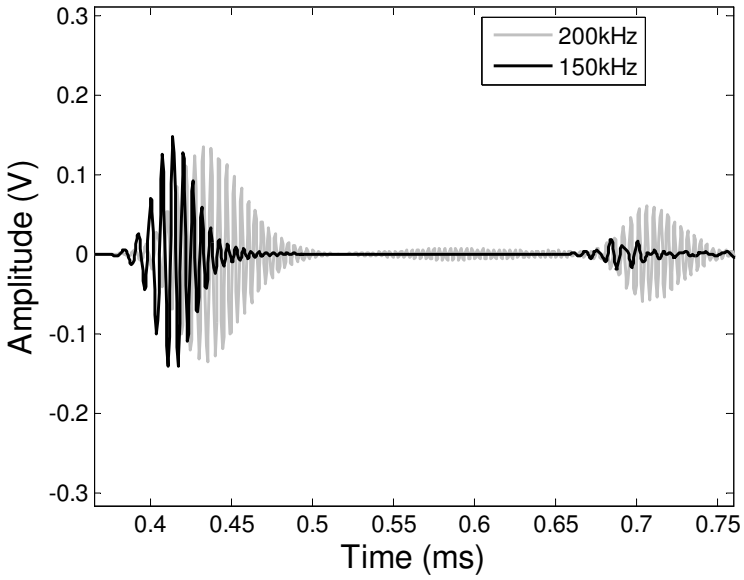

Figure 3.24: *Voltage time-traces obtained from FE modelling of a S0 mode transducer on a 5mm-thick aluminium plate simulating operation in pulse-echo mode.*

on the surface of a 5 mm-thick aluminium plate were obtained from the software DISPERSE [2] for both modes at the two excitation frequencies, in order to calculate experimental S0/A0 power flow ratios. Again, to eliminate reduction of amplitude due to dispersion effects, the amplitude of the spectrum of the wavepackets of the S0 and A0 modes at the centre frequency of the input signal was considered. At 150kHz the S0/A0 power flow ratio obtained was 10.9dB and at 200kHz it was 3dB. In the case of pitch-catch mode operation, these values should be doubled due to transmit-receive reciprocity, leading to values of 21.8dB and 6dB at 150 and 200kHz respectively.

The FRF of the transducers during temperature variation was also monitored, this time by placing the laser interferometer on the back of the transducer when it was attached to a 5 mm-thick aluminium plate, and measuring the out-of-plane response. Figure 3.26 shows the change in magnitude of the FRF with 20°C temperature change; the shape of the curves is very similar, only amplitude variations being seen which are straightforward to compensate for. Figure 3.27 shows that the phase

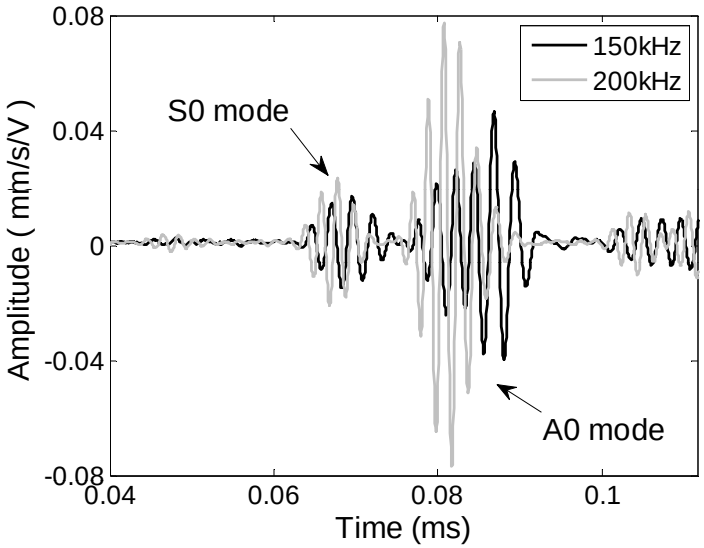

Figure 3.25: *Out-of-plane velocity time-traces measured with a laser interferometer at 30 cm from S0 mode transducer.*

variation with temperature is small over the frequency range of interest.

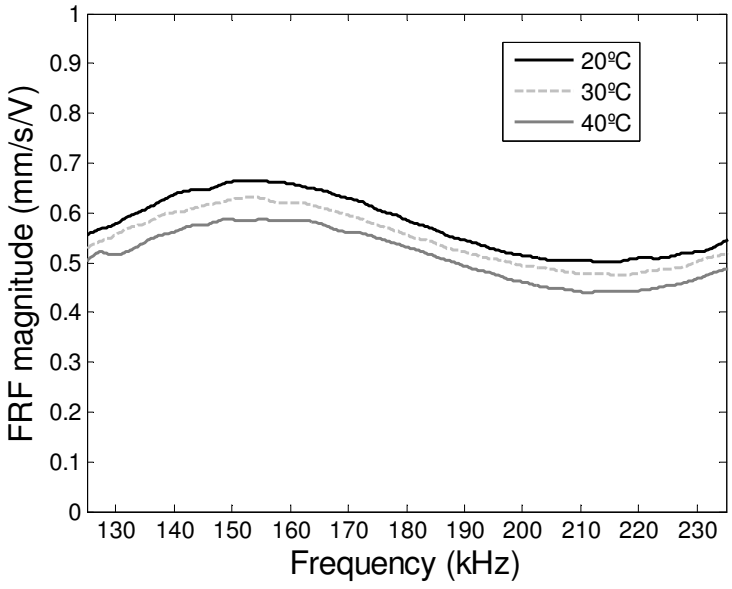

Figure 3.26: *Magnitude of FRF obtained from measuring the out-of-plane velocity on the back of a S0 transducer attached to a 5 mm-thick aluminium plate.*

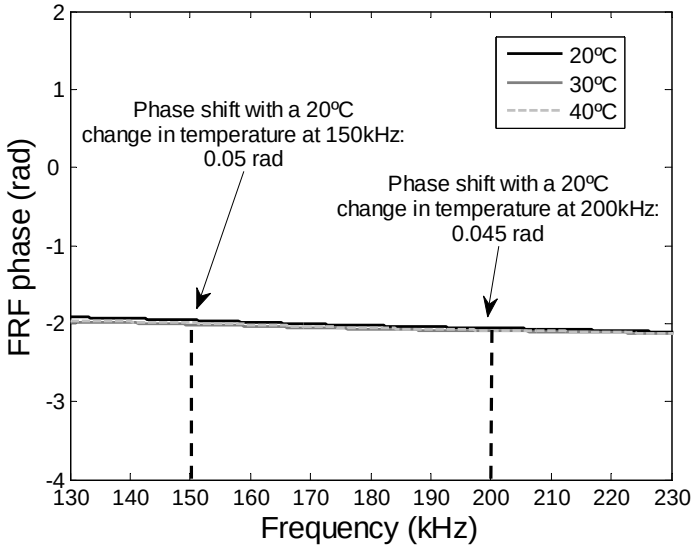

Figure 3.27: *Phase of FRF obtained from measuring the out-of-plane velocity on the back of a S0 transducer attached to a 5 mm-thick aluminium plate.*

3.4 Summary

A transducer generating high purity A0 mode at low frequencies was developed and the behaviour of a transducer generating substantially pure S0 mode was described.

For the A0 mode transducer, good agreement was obtained between results of a finite-element parametric study and experimental results in the 10-50kHz frequency range. The optimal geometry of this transducer was achieved by varying the size of a backing mass, used to lower the through-thickness resonance frequency of a piezoelectric disc from 1MHz to around 100kHz, and a soft front layer, which reduced the resonance of the system to around 20kHz and reduced the transmission of in-plane force generated by the piezoelectric disc to the plate.

The optimal A0 mode transducer geometry is a compromise between mode purity, bandwidth, and mode amplitude. A 2 mm-thick PZT disc with a 6 mm-long backing mass and a 2 mm-thick SiC foam front layer was found to be satisfactory. The optimal diameter is a function of plate thickness, varying from 5 mm at plate thicknesses up to 5 mm, to 25 mm at plate thicknesses from 25 mm to 30 mm. The

temperature stability of the transducer was evaluated and it was found that above resonance excitation, at 35kHz, gave excellent phase stability without significant loss of transmitted A0 mode amplitude or lowering of the A0/S0 mode ratio. Experimental results showed that A0/S0 mode power flow ratios over 40dB were obtained on 3 mm-thick aluminium plates and FE results suggest values above 35dB can be obtained on any plate thickness.

A 20 mm-diameter, 1 mm-thick piezoelectric disc was used to generate S0 mode. This transducer takes advantage of a lowering in transmission of the A0 mode in the frequency region close to where the diameter of the disc is equal to the A0 mode wavelength. FE results showed that a S0/A0 mode voltage ratio of 17dB could be obtained at 150kHz in pitch-catch on a 5 mm-thick aluminium plate, and experimental measurement showed that a S0/A0 mode power flow ratio of 21dB was obtained on a plate of the same thickness. If the same transducer is excited at 200kHz this ratio drops to 8dB. Experimental measurements of temperature stability showed that this transducer shows only small phase shifts in the frequency region from 120-240kHz, the only significant changes in the FRF being amplitude shifts which can easily be compensated for.

Chapter 4

Baseline subtraction and temperature compensation techniques

4.1 Introduction

In structures containing high densities of structural elements, the time-traces obtained are often too complex to be directly interpreted due to the large number of overlapping reflections. In this case, the Baseline Subtraction technique becomes attractive [48, 50]. As shown in Figure 4.1, in this method a current signal from the structure is subtracted from a signal which has been acquired during the initial stages of operation of the structure. This eliminates the need for interpretation of the complex raw time signal and any defects will be seen clearly provided the amplitude of the residual signal obtained after subtraction of the baseline signal is sufficiently low when the structure is undamaged. The target amplitude level of the residual signal is -40dB relative to the amplitude of the first arrival in a pitch-catch configuration, since most defects of interest in large area SHM and NDE, removing 30-50% of the wall thickness, give reflections of the order of -30dB or lower [78–81], so a residual of -40dB gives a 10dB margin.

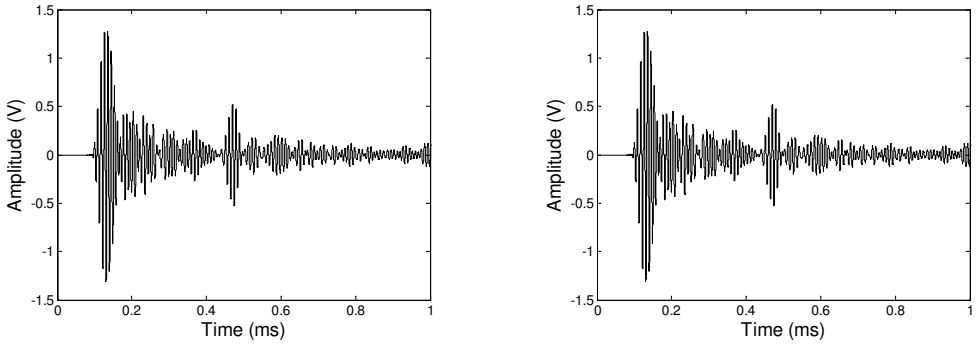

(a) Baseline signal - undamaged structure (b) Current signal - damaged structure

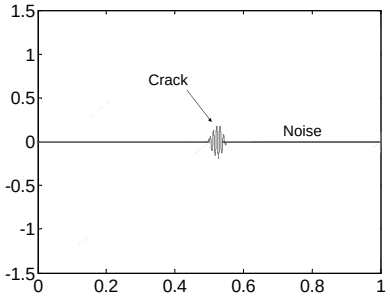

(c) Subtracted signal

Figure 4.1: *Schematic of baseline subtraction sequence, showing baseline signal, current signal and subtracted signal with the presence of a reflection from a defect.*

Temperature has a great influence on transducer performance and on wave propagation [51, 82]. As seen in chapter 3, the influence on transduction can be eliminated by careful material selection and assembly techniques. Wave propagation is affected when the elastic properties and density of the propagating medium are shifted. This means significant changes in signals will happen even with very small (<0.5°C) temperature drifts. Testing of the structure will happen over a range of temperatures which are bound to significantly change the signals obtained. Approaches to overcome this problem are presented in [9, 46, 82], and are called Baseline Selection or Optimal Baseline Subtraction; these involve the use of a database of signals that represents environmental conditions commonly faced by the undamaged structure which are recorded during the initial stages of operation. The current signal is compared to each signal in the database and the optimal baseline signal will be the one

which gives the lowest residual. However, to reach the targeted levels of amplitude in the residual signal, the temperature interval needed between baselines is very small. As will be demonstrated, an impractical number of baselines would be necessary to ensure acceptable results if only Baseline Subtraction is used.

Temperature compensation techniques [49,50] can be used in conjunction with Optimal Baseline Subtraction to increase the allowable temperature gap between baseline signals and therefore to reduce the number of signals in the database. However, these techniques may be affected by the complexity of the signals and the degree of mode purity.

This chapter begins by discussing the influence of mode purity and signal complexity on signal processing techniques for temperature compensation. Experimental set-ups consisting of simple pitch-catch arrangements using transducers described in chapter 3 which generate different A0/S0 mode ratios at a range of frequencies were used. The spatial frequency of reflectors was also varied by testing plates of different sizes. The effects are quantified so the minimum number of baselines necessary for a robust SHM system is identified. Finally, a real complex structure is monitored using the signal processing strategy described. The results of this chapter have been published in [46].

This chapter also shows the strong collaboration which took place during this project with the Non-Destructive Evaluation Group of the University of Bristol. Many of the results and concepts presented in this section are strongly based on their previous work and have been discussed extensively in project meetings between our groups.

Many of the parameters of the experimental procedures adopted will be found in the text of this chapter. Appendix B gives a more detailed description of the procedures.

4.2 Influence of temperature on wave propagation and baseline subtraction

The influence of temperature on wave propagation was demonstrated in [9]. Two Hanning-windowed tone bursts are considered, I_0 and I_1, which represent the baseline and the current signal respectively. The current signal is taken at a different temperature so it is expanded in time by δt, which is the time shift:

$$I_0 = u_0 h(t) \sin(wt) \tag{4.1}$$

$$I_1 = u_0 h(t + \delta t) \sin w(t + \delta t) \tag{4.2}$$

where $h(t)$ is the Hanning window function, u_0 is the amplitude, ω, the angular frequency, and t is time. The concept of Baseline Subtraction is applied and I_1 is subtracted from I_0. The change from $h(t)$ to $h(t+\delta t)$ and from $\sin(wt)$ to $\sin w(t+\delta t)$ shows that the group velocity and the phase velocity are affected by temperature variations.

RF subtraction is strongly preferred over envelope subtraction, although the latter misleadingly gives lower values of residual signal after subtraction due to the fact that the envelopes of the signals vary less rapidly than the RF signals with time and are therefore less sensitive to temperature-induced time-shifts. However, this also reflects a smaller sensitivity to change in shape of the envelopes due to the presence of a defect. In fact, as shown in [9], the use of envelope subtraction leads to a loss of linearity of the subtraction procedure, in the sense that the residual signal remaining after subtraction of a signal taken from a damaged structure and a baseline no longer expresses the amplitude of the reflection from the defect directly; on the other hand, with RF subtraction this linearity is maintained.

For RF subtraction the temperature-induced phase shift is the main concern; this

is unaffected by the window and we therefore neglect the difference between $u_0h(t)$ and $u_0h(t+\delta t)$ and define:

$$U_0 = u_0h(t) \approx u_0h(t+\delta t) \tag{4.3}$$

Hence,

$$I_1 - I_0 \approx U_0(\sin w(t+\delta t) - \sin wt) \tag{4.4}$$

By assuming that δt is small enough to allow a small angle approximation:

$$|I_1 - I_0|_{max} = 2\pi f U_0 \delta t \tag{4.5}$$

where f is frequency.

As demonstrated in [9], the time shift for direct subtraction can be represented as:

$$\delta t = \frac{d}{v}(\alpha - \gamma)\delta T \tag{4.6}$$

where γ is the fractional change in phase velocity with temperature, ν/v, ν being the coefficient of change in phase velocity with temperature and v the phase velocity; δT is the variation in temperature, d is the propagation distance, and α is the coefficient of thermal expansion. Equation 4.6 shows that change in wave velocity due to temperature drifts is the main cause of time shift in signals, since $|\gamma|$ is typically significantly larger than $|\alpha|$. It also shows that increases in temperature will always cause a positive δt, as this will increase the propagation path due to thermal expansion of the structure and reduce phase velocity values, since, as mentioned in [9], a typical value of ν is $-1m.s^{-1}.^oC^{-1}$. Equation 4.6 can be simplified to:

$$\delta t = \frac{d}{v}\beta\delta T \tag{4.7}$$

where β is $(\alpha - \gamma)$.

It follows from the development of Equation 4.5 that if two waves of equal amplitude arrive in phase, the amplitude of the residual signal will be doubled. When the number of reflectors increases, as in a complex structure, interference will happen more frequently, so the maximum residue after baseline subtraction will increase. This suggests that the residual signal is proportional to the temperature difference between the current signal and baseline (expressed by the time shift), to the number of overlapping arrivals and to the excitation frequency. It was shown in [46] that by combining Equations 4.5 and 4.7 and considering a single frequency (in practice the centre frequency of a toneburst), then the wavelength is $\lambda = v/f$, so:

$$|I_1 - I_0|_{max} = 2\pi\frac{d}{\lambda}U_0\beta\delta T \tag{4.8}$$

Equation 4.8 shows that the residual level is proportional to the propagation distance expressed in wavelengths rather than simply to the frequency; only if the velocity is constant with frequency (i.e. the mode is non-dispersive) is the residual for a given propagation distance simply proportional to frequency. This is an important issue when selecting the mode and frequency which will be used by the monitoring system.

As shown in [9], the residual level predicted by Equation 4.8 increases significantly with increases in δT. The danger of having such high levels of amplitude in the subtracted signal is that reflections from defects can be masked; therefore, the quality of the baseline subtraction controls the sensitivity of the system to defects. Figure 4.2(a) shows the subtracted signal resulting from the direct subtraction between a baseline and a current signal measured experimentally on a real structure with a 0.2°C difference; although subtraction is not perfect the signals are similar, as

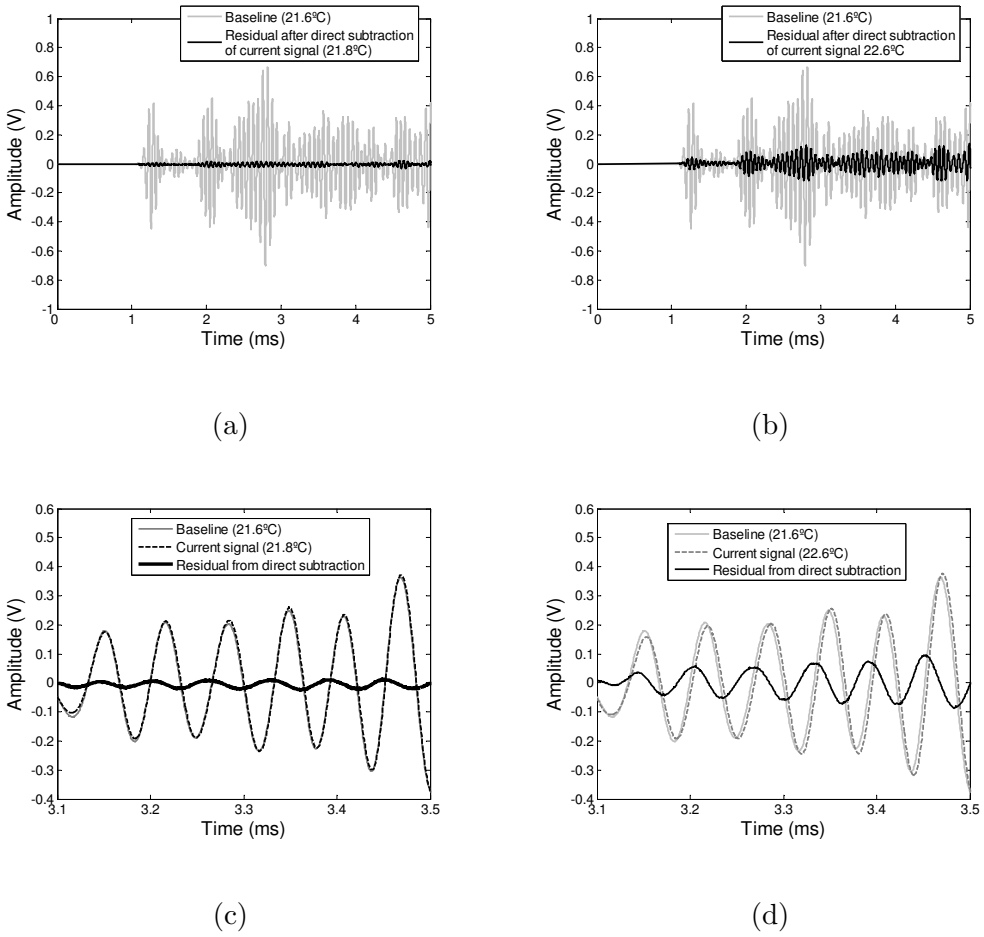

Figure 4.2: *(a) Baseline (21.6º C) and subtracted signal obtained after direct subtraction of current signal at 21.8º C, recorded on a real structure; (b) Baseline (21.6º C) and subtracted signal obtained after direct subtraction of current signal at 22.6º C, recorded on a real structure; (c) Detail of (a); (d) Detail of (b).*

shown in Figure 4.2(c), due to the small temperature difference in between them. Figure 4.2(b) shows the subtracted signal obtained when the same baseline is directly subtracted from a current signal taken with a 1ºC temperature difference; levels of residual are much higher, due to the time dilation described by Equation 4.7, as can be seen in Figure 4.2(d). It is therefore clear that in most cases a single baseline will not be able to cover the entire temperature range to which a real structure is subjected.

4.3 Temperature compensation methods

4.3.1 Optimal Baseline Subtraction

The Optimal Baseline Subtraction method attempts to minimise residual signal amplitude levels by using not only one baseline, but a large database of signals taken from the undamaged structure over a given period of time, when the presence of defects arising from construction has been eliminated by the use of conventional NDT techniques; if adequately collected, the signals in this database will cover temperature and environmental conditions commonly faced by the structure. The method is based on the identification of a baseline within the database which is most similar to a current signal taken from the structure during inspection. If the two signals are similar enough, low levels of residual will be achieved when the two are subtracted in the absence of a defect. Since environmental effects are the main reason for changes in the response of the system, the Optimal Baseline method is effectively a search for the signal which has been taken at environmental conditions similar to those found during inspection. The database of signals will have been previously acquired during the initial stages of operation of the structure after conventional NDE techniques have been used to search for manufacturing defects. The selection of the Optimal Baseline is generally done by subtracting all the signals in a database from the signal currently taken during inspection. The choice of best baseline is done by monitoring a value which describes the amplitude of the residual signal. It is clear that a large database, covering all environmental conditions likely to seen in practice, is necessary if small residual levels are to be obtained with this method. As demonstrated in [82], the minimum level of residual is not necessarily found when the current signal is subtracted from a baseline taken at exactly the same temperature at an earlier stage; the Optimal Baseline is often a signal taken at a slightly different temperature, the difference typically being of the order of 0.1°C. This effect may be attributable to uncertainties in temperature measurement.

4.3.2 Optimal Stretch

As seen in section 4.2, temperature changes affect the velocities of the different modes besides causing expansion or contraction of the structure. These changes cause signals to arrive earlier or later in time; this effect is cumulative so that later parts of the signal, corresponding to larger propagation distances, suffer larger absolute delays.

Several related methods for correcting this effect have been presented in the literature based on time domain stretching [83] of either the reference signal or the current signal, estimation of delay as a function of time through local coherence and use of these values as factors for subsequent time-domain stretch [50, 51], or simple frequency domain stretch [3, 46, 49].

In theory, only one baseline would be needed when using this method, since current signals would be stretched or compressed until they matched this universal baseline. However, the compensation is not perfect and the size of the residual signal after subtraction is affected by several factors, the most immediate being that not only the arrival time of reflections is modified by stretching the content of the signal in the time or frequency domain, but the reflections themselves are also deformed. The proportionality between δt and δT in Equation 4.7 shows that this effect will become more significant as δT increases, since the stretch needed to match the signals will be greater and wave packets will suffer significant changes in their frequency content.

In this study the correction was made in the frequency domain by stretching the frequency axis. Figure 4.3(a) shows part of the spectrum of a reference signal and of a second signal taken with a temperature difference of 10°C. To compensate for the small difference between the two spectra, the frequency step size, Δf, of the spectrum of the second signal was stretched or compressed in small steps. In each step, the stretched spectrum of the second signal would be multiplied by the ratio between the spectrum of the input signal and the stretched spectrum of the input signal; this is a correction factor for spectrum distortion effects, as described in [49]. The Optimal Stretch corresponds to the minimum of the residual signal in time or

to the maximum in correlation between the spectra of the two signals. Figure 4.3(b) shows the best match between the spectra of the two signals shown in Figure 4.3(a). Small differences in the overall amplitude of the two spectra are compensated by normalising the power content of each signal in the frequency domain. This amplitude correction in the frequency domain occasionally leads to excessive or insufficient amplitude corrections at certain frequencies, as can be seen, for example, in the region around 29-30 kHz in Figure 4.3(b), but the overall amplitude differences in the time domain are considerably improved. This is seen in Figure 4.4 which shows the time-traces related to Figure 4.3, obtained with two of the A0 mode transducers described in chapter 3 in pitch-catch on a 1 m-square, 5 mm-thick aluminium plate (for further details of the setup, see [3]). Figure 4.4(a) shows the current or second time-trace recorded at 31.8°C and the subtracted signal obtained after direct subtraction of a baseline at 21.6°C. The amplitude of the subtracted signal relative to the amplitude of the first arrival "A" in Figure 4.4(a) is shown in Figure 4.4(b); high levels or residual are seen, the worst being around -7dB. When the Optimal Stretch method is applied to the current signal, and the resulting time-trace is subtracted from the same baseline, the subtracted signal seen in Figure 4.4(c) is obtained. Figure 4.4(d) shows this residual relative to the amplitude of the first arrival "A"; it is clear that an improvement in residual amplitude levels close to 20dB was obtained by the stretch demonstrated in Figure 4.2(a).

4.3.3 Filtering of noise in subtracted signal after Optimal Stretch

When the Optimal Stretch method is used to compensate for a temperature gap between a reference and a current signal, differences in matching of different regions of the spectrum are often seen. This unequal matching occurs because the centre frequency of the spectrum of the two signals is where the largest power is concentrated and therefore the highest amplitude is found. Consequently, the best match of the region close to the centre frequency during stretch of the frequency axis will cause the sharpest drop in the rms of the residual signal. However, the quality of the

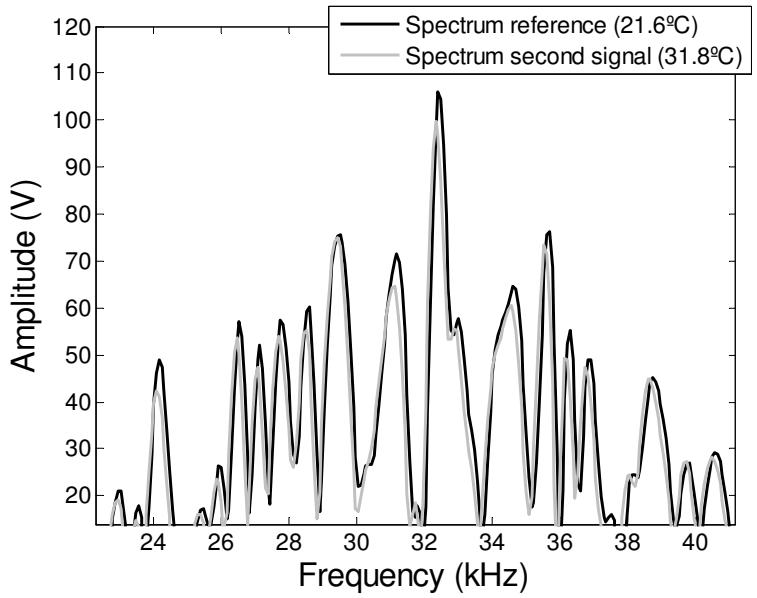

(a)

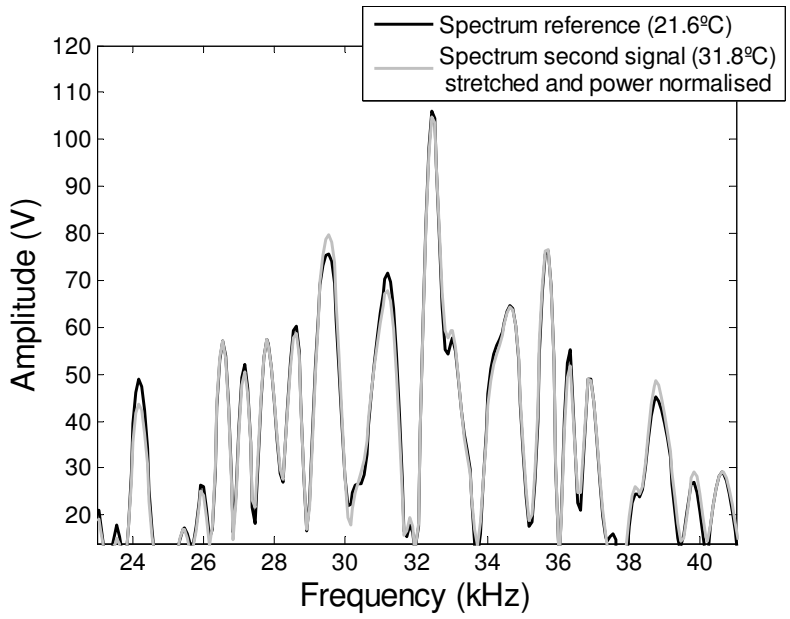

(b)

Figure 4.3: *(a) Spectrum of the reference signal (21.6°C) and of the current signal (31.8°C); (b) Spectrum of the reference signal (21.6°C) and of the current signal (31.8°C) after Optimal Stretch and power normalisation [3].*

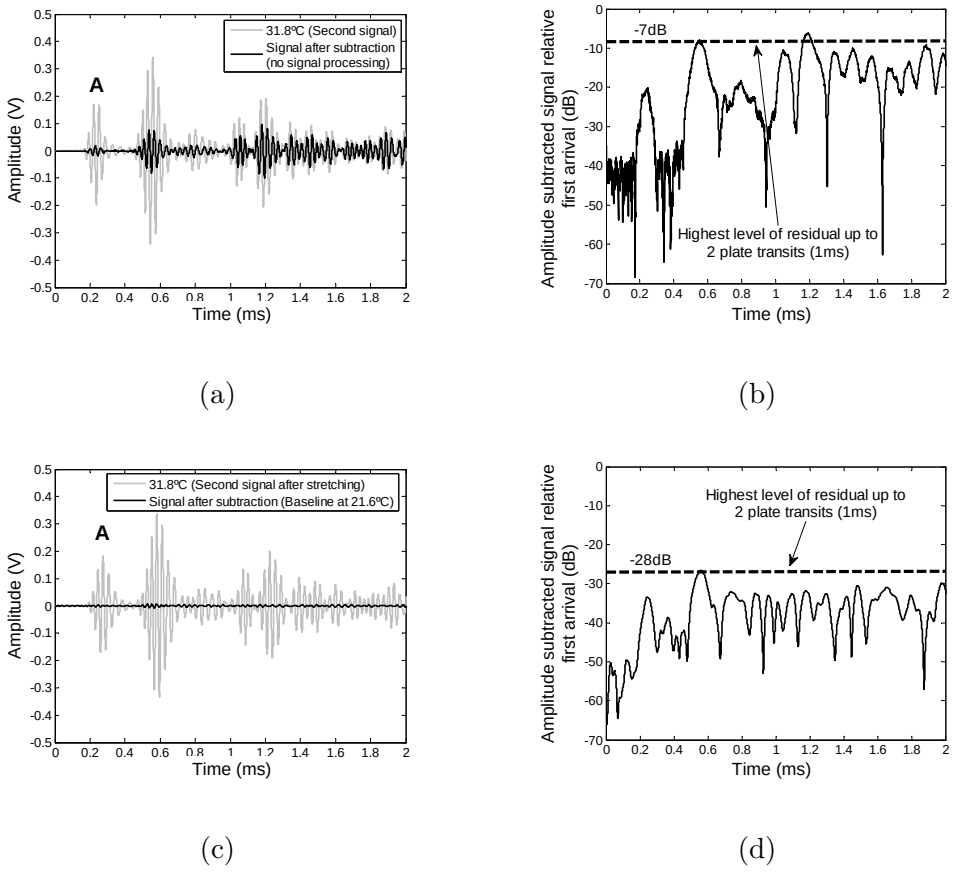

Figure 4.4: *(a) Second signal (31.8°C) and subtracted signal obtained after direct subtraction of baseline signal at 21.6°C; (b) Amplitude subtracted signal relative amplitude of first arrival A in (a); (c) Stretched and power normalised second signal (31.8°C) and subtracted signal obtained after subtraction of baseline signal at 21.6°C; (d) Amplitude subtracted signal relative amplitude of first arrival A in (c) [3].*

match in other parts of spectrum is less good and analysis of the frequency content of the subtracted signal shows that high levels of residue are found at frequencies above or below the centre frequency region. Figure 4.5 shows the spectrum of the subtracted signal seen in Figure 4.4(c). High amplitudes are seen at frequencies below the centre frequency of the input signal (35 kHz). A filter with bandwidth equivalent to that of a 7-cycle Hanning windowed toneburst was used to eliminate the unwanted regions of the spectrum of the subtracted signal. The use of such a simple bandpass filter can give a 5-10dB reduction of amplitude levels in the residual. This is shown in Figures 4.6(a) and 4.6(b), which show the filtered subtracted signal of Figure 4.5 in the time domain; a 10dB improvement in residual amplitude

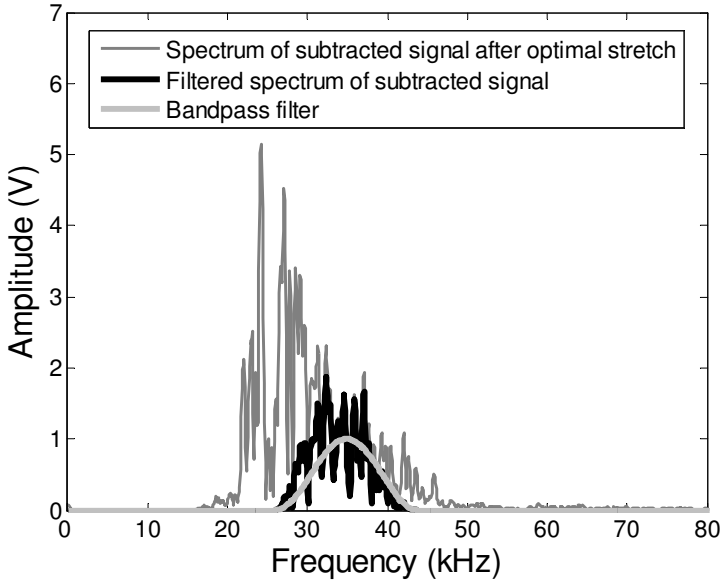

Figure 4.5: *Spectrum of the subtracted signal in Figure 4.4(c), bandpass filter and final filtered subtracted signal [3].*

is seen in comparison with the levels shown in Figure 4.4(d). The bandwidth of the filter was chosen as a compromise between reduction of noise levels and maintenance of sufficient spatial resolution for defect localisation.

The bandpass filter described in this section was applied to the residual signals in all cases in which the Optimal Stretch was used.

4.4 Evaluation of temperature compensation methods

4.4.1 Specimens and experimental setup

Figure 4.7 shows a sketch of the simple pitch-catch system used in this work. Two steel plates of 5 mm thickness and lengths L of 1 m and 0.4 m were used. All other dimensions, including positioning of the transducers, were kept proportional to L.

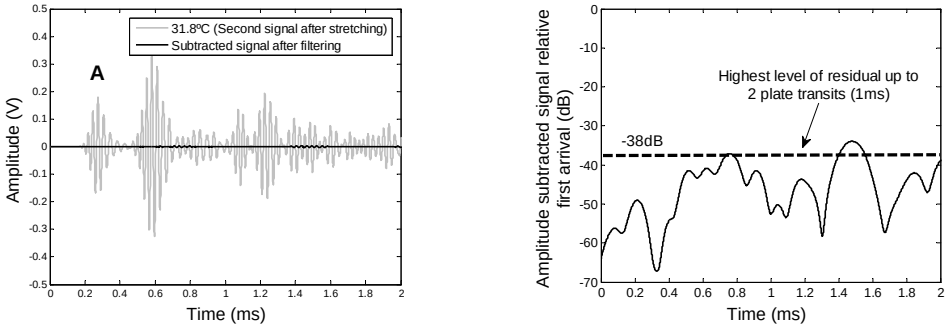

(a) (b)

Figure 4.6: *(a) Second signal (31.8°C) and subtracted signal obtained after Optimal Stretch, power normalising and filtering of noise; (b) Amplitude subtracted signal relative amplitude of first arrival A in (a) [3].*

The system was placed in a temperature controlled environment where the temperature was gradually increased by 10°C and then cooled back to ambient temperature, signals being acquired at 0.1°C steps. This cycle was repeated with an interval of a day and signals obtained during the first cycle were used as baselines while signals from the second cycle were considered current signals. The temperature was monitored by type-K thermocouples soldered to the plate next to the transducers. Temperature was read to a precision of 0.1°C.

The two types of piezoelectric transducers described in chapter 3 were used. Both transducers were attached to the plates with epoxy adhesive (Loctite Hysol E-05CL) which was room temperature cured for 36h and cycled at temperatures above those expected during operation to avoid post-curing effects and to relieve residual stresses in the bond layer which lead to changes in stiffness during operation [74]. Constant pressure was applied to the transducer during curing so that a thin bond line was obtained; this reduces the influence of change in the bond line on transducer behaviour.

A PC was used to upload input signals to an arbitrary function generator (Agilent 33220) which was connected through an amplifier to the emitting transducer. The signal from the receiver was pre-amplified and acquired via a 12-bit PC-based

oscilloscope set to 100 averages.

A brass cylinder of 5 mm diameter and 6 mm length was attached to the surface of the plates with a couplant to simulate a weak reflector or "defect". The position of this simulated defect is indicated in Figure 4.7.

All residual signals obtained after processing and baseline subtraction were corrected for beam-spreading by:

$$RS(t) = \sqrt{\frac{t.V_{gr}}{D}}.rs(t) \tag{4.9}$$

where $rs(t)$ is the uncorrected residual signal, $RS(t)$ is the corrected residual signal, t is the corresponding arrival time of each point of $rs(t)$, D is the distance between the transmitter and the receiver, and V_{gr} is the group velocity of the excited mode at the centre frequency of the input signal. The factor multiplying $rs(t)$ in Equation 4.9 corrects the amplitude of the signal relative to the maximum amplitude of the first arrival.

4.4.2 Results for different plate sizes

Results presented in this section were obtained by using two low-frequency A0 transducers in a pitch-catch configuration on the two plate sizes, with dimensions as described in section 4.4.1 and Figure 4.7.

4.4.3 Optimal Baseline Subtraction method

Figure 4.8(a) shows the signal obtained from the large plate at a temperature of 28.9°C and the residue obtained when this signal and the selected Optimal Baseline, which was taken on the previous day at 29.0°C, are subtracted. The first arrival can clearly be seen and multiple reflections from the edges of the plate arrive later. The noise levels in the subtracted signal relative to the amplitude of the first arrival are

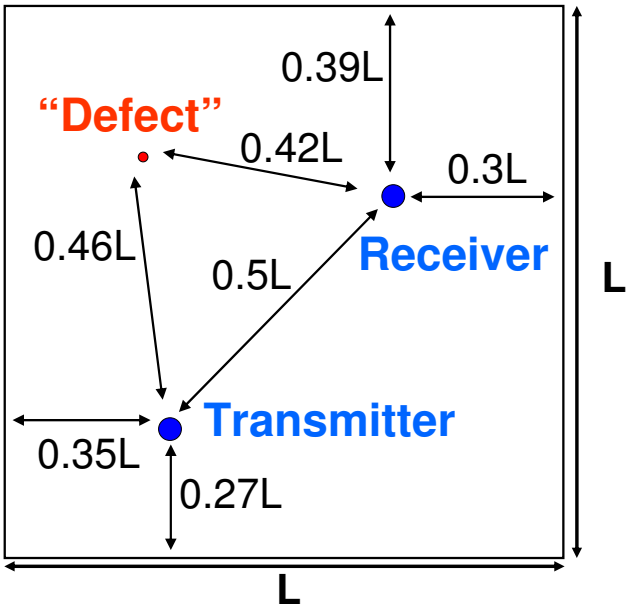

Figure 4.7: *Schematic diagram of positioning of transducers and defect as a function of plate length L.*

shown in Figure 4.8(b) and correspond to a worst case of -38dB. This value is close to the target of -40dB but these results demonstrate how small the temperature gaps between baselines need to be to ensure satisfactory results.

Figure 4.9(a) shows the signal obtained for the small plate at 32.6°C and the residual signal after subtraction from the Optimal Baseline, which in this case was taken at 32.5°C. The decay rate of the signal in Figure 4.9(a) is much higher than that of the correspondent signal on the large plate (Figure 4.8(a)). This is thought to be due to mode conversion at the edges, which are not perfectly normal to the surface, and to attenuation and mode conversion at transducer bond lines. In the small plate there are more interactions with the edges and bond lines in a given time than on the large plate (propagation equivalent to one side length takes 0.18ms in the small plate and 0.45ms in the large plate).

Figure 4.9(b) shows that the level of residue obtained, -39dB relative to the first arrival in Figure 4.9(a), is also close to the target of -40dB. In the simpler signal of Figure 4.8(b), only one time region was responsible for the worst residual amplitude

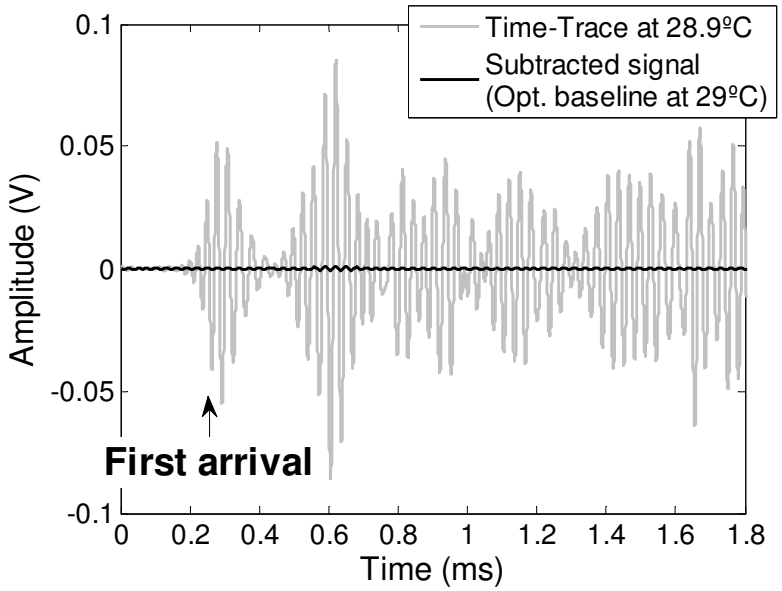

(a)

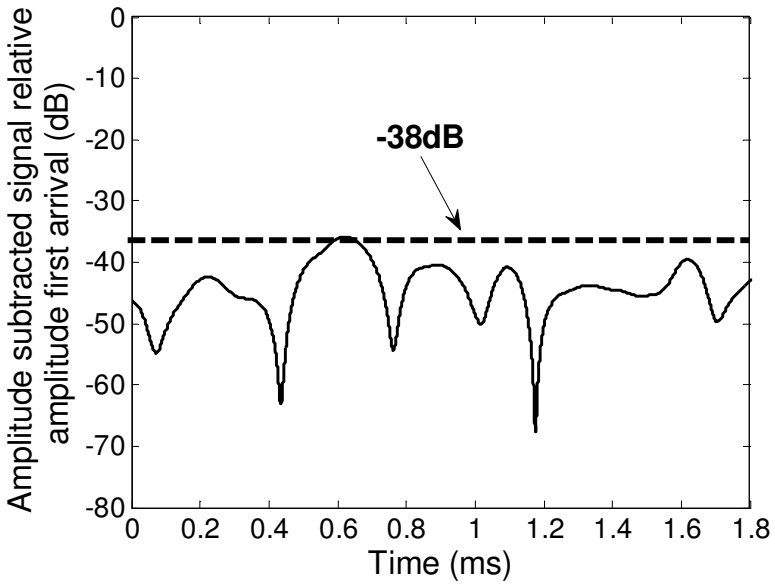

(b)

Figure 4.8: *(a) Signal taken at 28.9º C and the signal obtained when subtracted from baseline (29º C) on the large plate; (b) Amplitude of the subtracted signal relative to amplitude of the first arrival in Figure 4.8(a).*

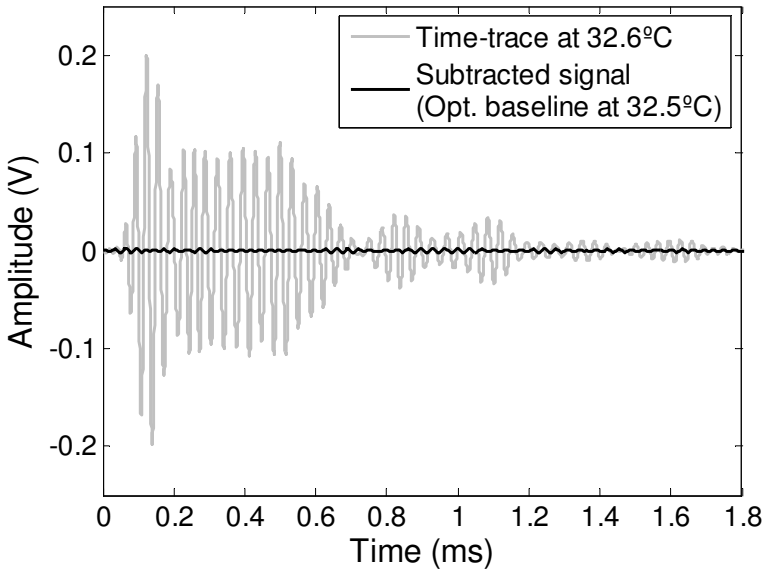

(a)

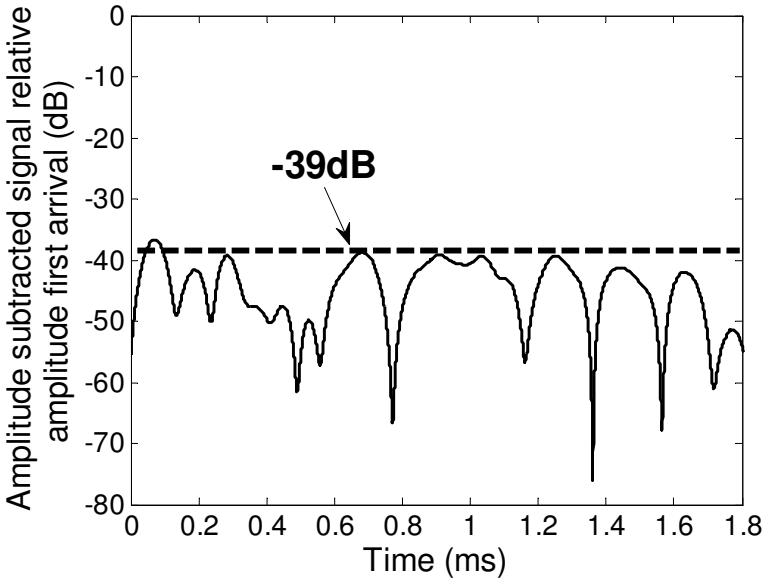

(b)

Figure 4.9: *(a) Signal taken at 32.6°C and the signal obtained when subtracted from baseline (32.4°C) on the small plate; (b) Amplitude of the subtracted signal relative to amplitude of the first arrival in Figure 4.9(a).*

value, which was the point (0.6ms) where four reflections from the edges overlap. The corresponding point in the small plate is at 0.25ms, but since the distances between reflectors are smaller than in the large plate case, strong overlapping of reflections happens throughout the entire signal.

Figures 4.10(a) and 4.10(b) show the residual levels after subtraction of signals taken on the large plate and the small plate with a temperature gap of 0.3°C. This simulates the effect of the baseline data set being obtained with a larger temperature step size. In both cases the worst residual level is increased to around -31dB relative to the first arrival. This shows that if the Optimal Baseline method is used alone it is necessary to store a very large baseline set at small temperature step sizes (0.1°C), which is likely to be impractical to store and difficult to obtain.

4.4.4 Optimal Stretch method

For the results shown in this section, a signal taken at room temperature (21.5°C) will be taken as the reference and the effectiveness of the Optimal Stretch method will be evaluated for a current signal taken 5°C above reference. This temperature difference was considered a challenging test for the robustness of the Optimal Stretch method because high levels of residual are found for direct subtraction of the two signals as seen in Figure 4.11(a), which shows the signal taken from the large plate at 26.5°C and the signal obtained after direct subtraction from the baseline at 21.5°C. Figure 4.11(b) shows that the worst amplitude level in the residual reaches -10dB relative to the first arrival.

Figure 4.12(a) shows the signal obtained after temperature compensation of the signal of Figure 4.11(a) through the Optimal Stretch method. The amplitude levels in the subtracted signal are around -38dB relative to the first arrival seen in Figure 4.12(a) for a 5°C temperature change, as can be seen in Figure 4.12(b). This is a large improvement compared to the value of the signal obtained from direct subtraction (-10dB relative to the first arrival, as shown in Figure 4.11(b)).

The same procedure was repeated for signals obtained on the small plate. The worst

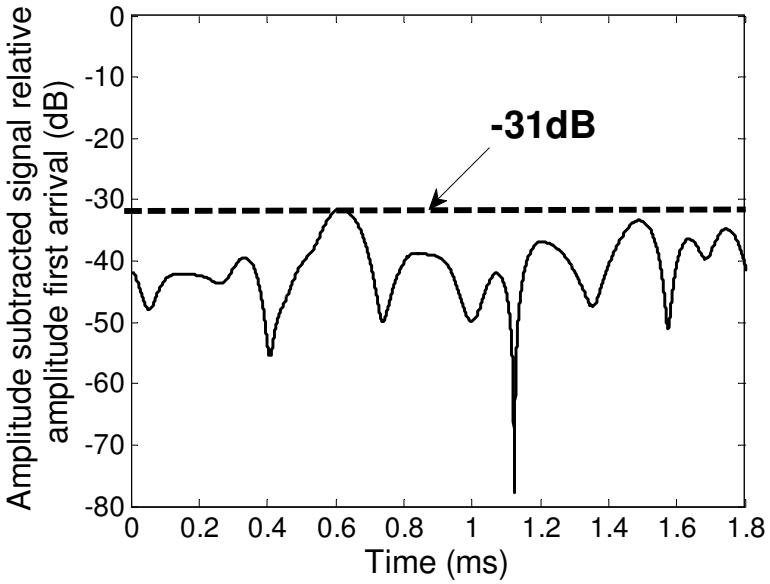

(a)

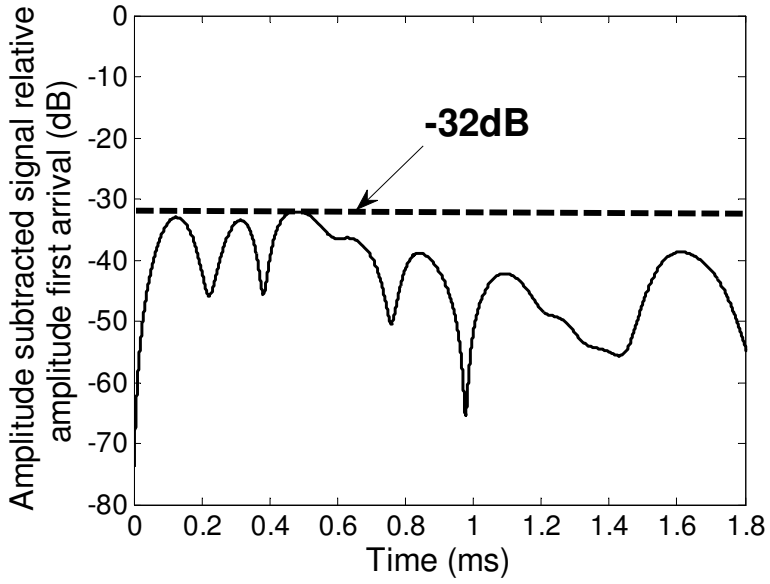

(b)

Figure 4.10: *Residual levels after subtraction for: (a) Large plate; (b) small plate; with a temperature gap between current signal and baseline of 0.3°C (current signal at 32.6°C, baseline at 32.3°C), relative to the first arrival.*

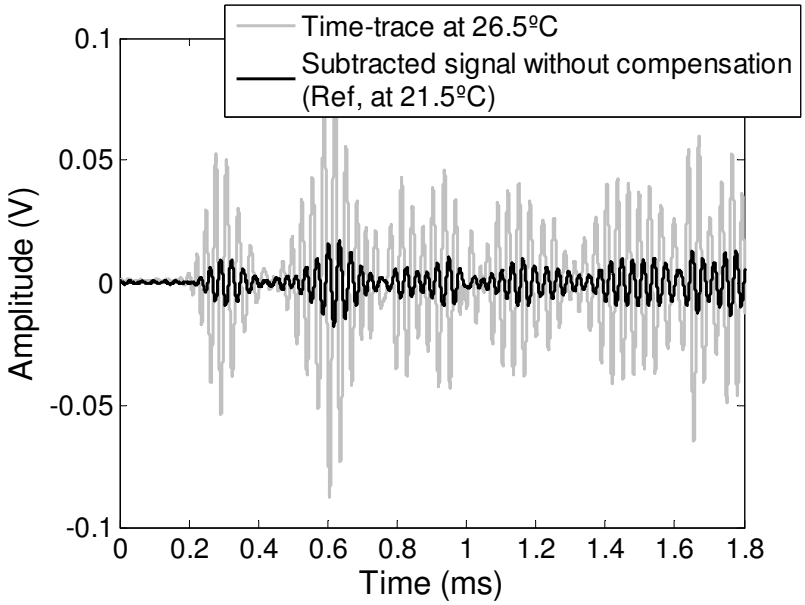

(a)

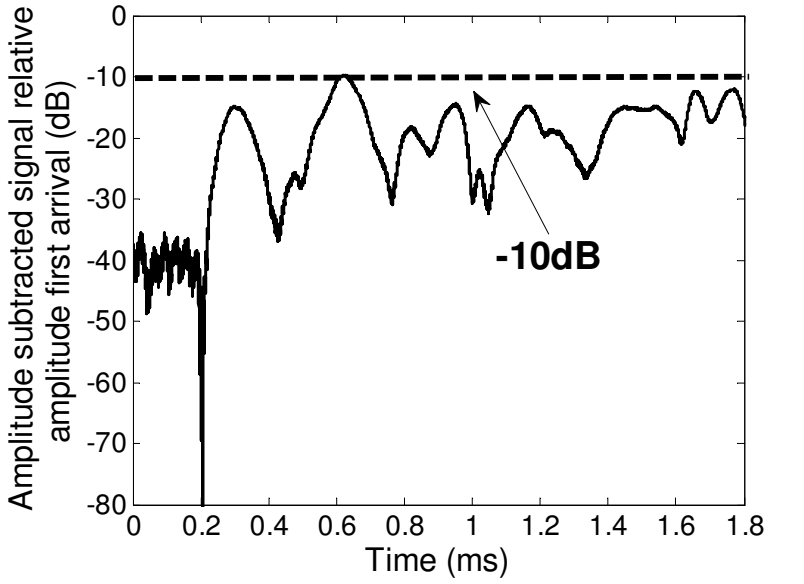

(b)

Figure 4.11: *(a) Signal taken at 26.5°C and the signal obtained from immediate subtraction from baseline (21.5°C) on the large plate; (b) Amplitude of the subtracted signal relative to amplitude of the first arrival in Figure 4.11(a).*

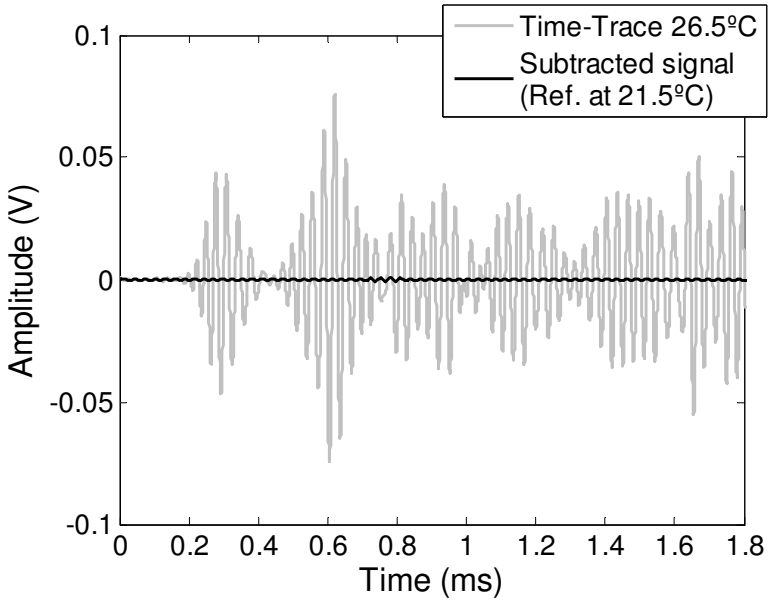

(a)

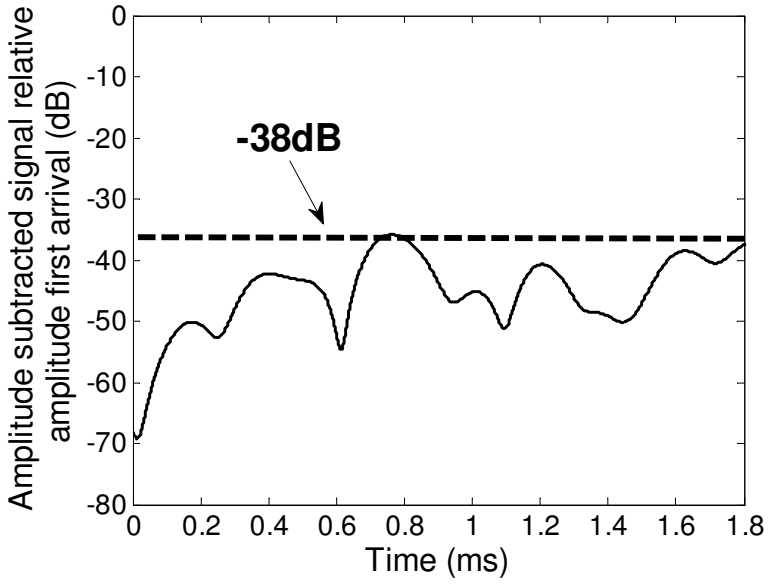

(b)

Figure 4.12: *(a) Signal taken at 26.5°C and the signal obtained when subtracted from stretched reference (21.5°C) on the large plate; (b) Amplitude of the subtracted signal relative to amplitude of the first arrival in Figure 4.12(a).*

amplitude level in the residual signal after direct subtraction between a signal taken at 26.5°C and a baseline at 21.5°C was -11dB relative to the first arrival. This level is similar to the result obtained for direct subtraction between two signals taken at the same temperatures on the large plate (as was seen in Figure 4.11(a)).

When the Optimal Stretch technique is used to compensate for the 5°C temperature difference between the signals taken from the small plate, the residual signal level shown in Figure 4.13 is obtained after subtraction. A worst value of -27dB relative to the first arrival was found; this is far from the target value of -40dB and much poorer than the performance of the method on the signals taken on the large plate. This difference between the large and small plates was seen consistently in data from multiple experiments. This suggests that the effectiveness of the Optimal Stretch method in compensating for large temperature differences is reduced when it is applied to more complex signals comprising a large number of reflections. The Optimal Stretch method therefore has limited applicability on health monitoring of complex structures if it is used as the sole temperature compensation technique.

4.4.5 Combined use of the Optimal Baseline and the Optimal Stretch methods

Figures 4.14(a) and 4.14(b) show the results obtained when applying the Optimal Stretch method to compensate for a temperature difference between a current signal taken at 26.5°C and reference signals taken 1°C and 2°C below that temperature, respectively, on the small plate. The worst value in the residual signal in Figure 4.14(a) is above the -40dB target value; however, an improvement of 5dB is seen compared to the level obtained in Figure 4.13, when the temperature difference was 5°C. When the temperature difference is further reduced, to 1°C, the residual signal level is greatly improved, reaching the target value of -40dB (Figure 4.14(b)). This shows that although the Optimal Stretch method cannot be applied as the sole method for temperature compensation of complex structures, it can be used in conjunction with the Optimal Baseline method to reduce the number of baselines

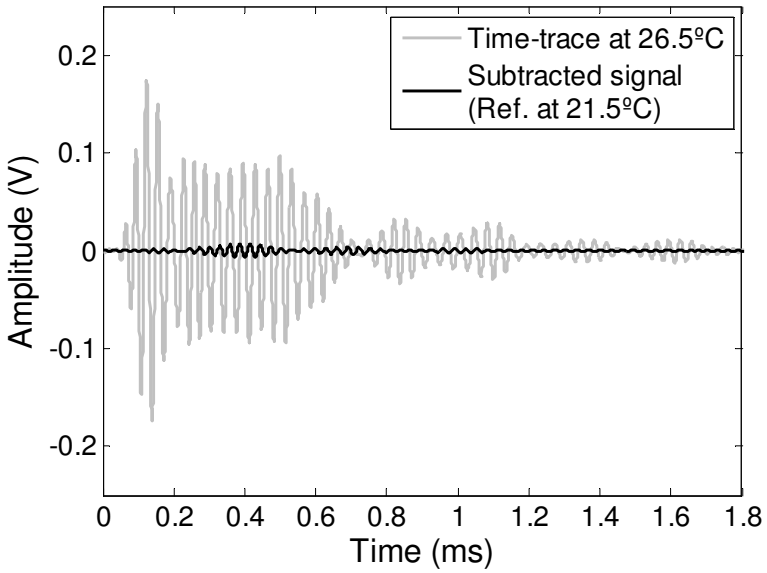

(a)

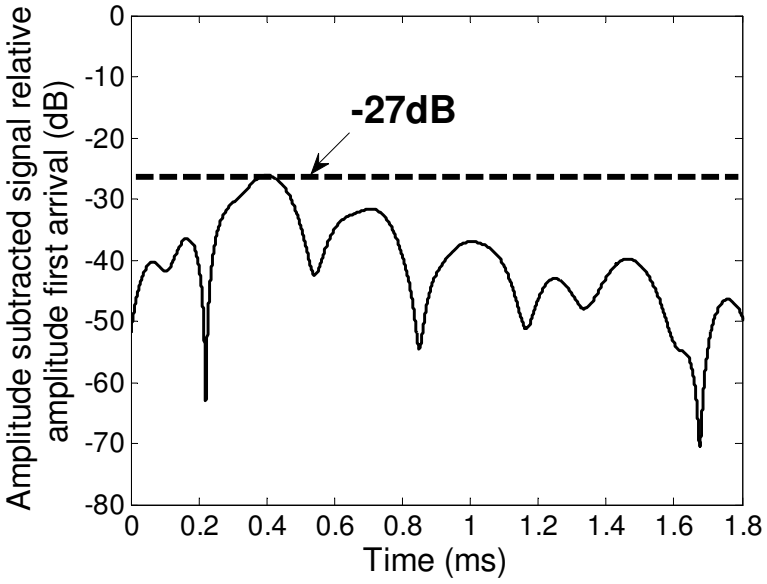

(b)

Figure 4.13: *(a) Signal taken at 26.5°C and the signal obtained when subtracted from stretched reference (21.5°C) on the small plate; (b) Amplitude of the subtracted signal relative to amplitude of the first arrival in Figure 4.13(a).*

necessary to achieve target values of residual.

Therefore, if a number of baselines within the operating temperature range of a structure are collected, the following strategy can be applied: the Optimal Baseline method identifies the baseline providing the closest match to a signal taken during inspection and the Optimal Stretch method then compensates for remaining differences in temperature between the best baseline and the current signal. If such a strategy is applied to the small and large plates used in the experiments, the maximum gap between baselines to achieve the target levels of residual signal would be 1°C for the small plate and 5°C for the large plate. The increase in the maximum admissible temperature gaps between baselines makes collecting signals for the database an easier task since this gives a margin for temperature fluctuations in between data collections.

The maximum temperature difference that can be effectively compensated by the Optimal Stretch method is thought to decrease as more complex signals are processed. This suggests that the number of baselines needed for achievement of low levels of residue with such a processing strategy will increase with signal complexity. Nevertheless, the combination of the Optimal Baseline and the Optimal Stretch techniques will always require a smaller database than if the former is used alone. This was also confirmed by work in [52].

The signal processing strategy consisting of the combination of the Optimal Stretch and the Optimal Baseline techniques will be used in the sections below.

4.4.6 Response to simulated defects

The response of the large and small plate systems to simulated defects was evaluated. As mentioned in section 4.4.1, the simulated defect consisted of a brass cylinder with 5 mm diameter and 6 mm length attached to the surface of the plates with a couplant. The reflection ratio from this "defect" was estimated to be of the order of -24dB, though it was strongly dependent on the coupling, making quantitative comparisons between the results in the two plates invalid. The reflection ratio was

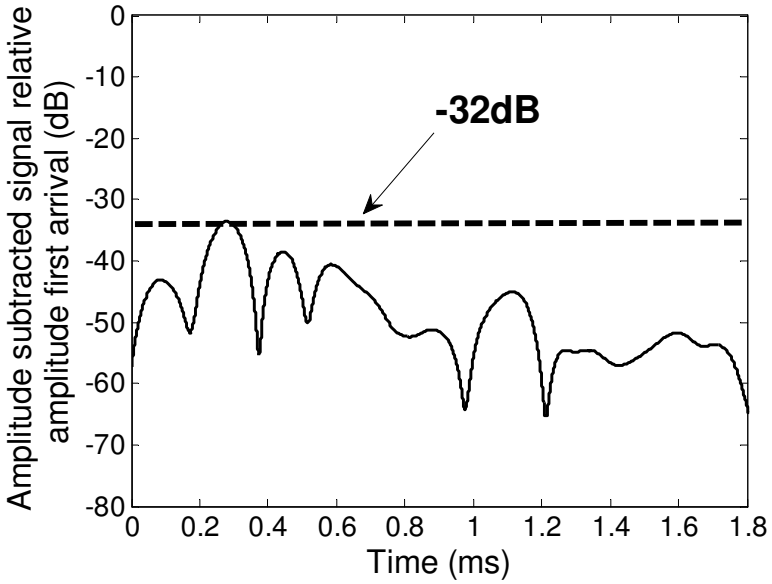

(a)

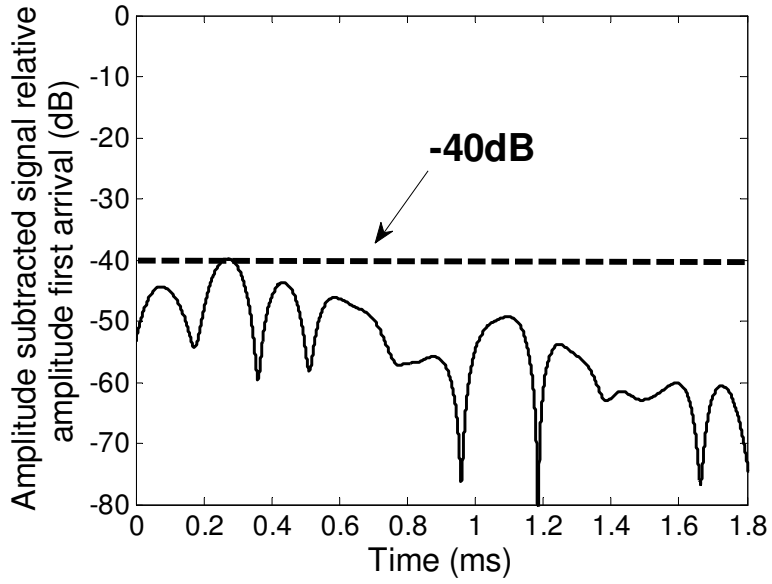

(b)

Figure 4.14: *Amplitude of the subtracted signal relative to first arrival for: (a) a 2°C difference between current signal (26.5°C) and reference (24.5°C) after Optimal Stretch for small plate; (b) a 1°C difference between current signal (26.5°C) and reference (25.5°C) after Optimal Stretch for small plate.*

defined as the ratio of the amplitude of the reflection from the "defect" to the amplitude of the incident signal. This was measured by focusing a laser vibrometer at a point in-line between the transmitter and the "defect" at a position where the two signals could be separated in time. The amplitudes were corrected for propagation distances to correspond to the values at the "defect" location before computing the ratio.

A signal was taken at 26.5°C on the two plates, with and without the "defect", and compared to a baseline 0.5°C below this temperature, the "with defect" signals being taken the day after the baselines. The levels of the residual signal obtained by processing the signals acquired from the "undamaged" plate were compared to levels obtained from signals acquired with presence of the "defect".

Figure 4.15(a) shows the time-trace obtained on the large plate with the "defect" and the residual signal left after processing and subtraction. In Figure 4.15(b) the amplitude levels can be more easily identified and a first excursion above the "undamaged" residual values was seen at the time corresponding to the first arrival of a reflection from the "defect". This signal is 4dB above the level of residual signal for the plate with no "defect", suggesting a reflection from the defect of less than -35dB. This is much lower than the reflection ratio measured above due to the distance of the transducers from the defect. This illustrates that the detectability of a given defect is strongly dependent on the position relative to the transducers. The later parts of the signal are clearly disturbed and residual levels above -29dB are found. This is caused by shadowing effects created by the presence of the "defect" which cause increases and decreases of amplitude in subsequent reflections from the edges of the plate.

Figure 4.16(a) shows the signal obtained from the small plate at 26.5°C with the presence of a "defect" and the residual signal left after Optimal Stretch of the baseline and subtraction. Figure 4.16(b) shows a first excursion 7dB above the level for the "undamaged" plate. The presence of a defect in the small plate was relatively easy to detect compared to the large plate case. This is because the reduction of scale means the "defect" was closer to the transducers. However, as explained above,

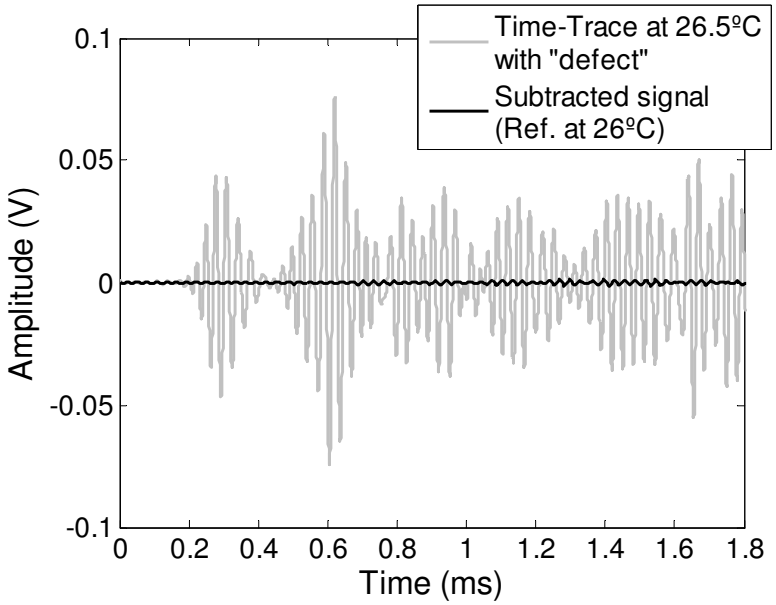

(a)

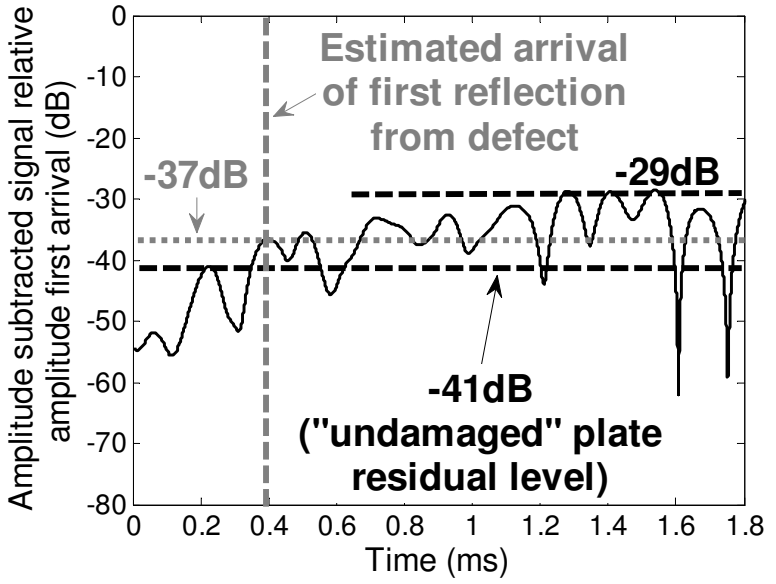

(b)

Figure 4.15: *(a) Signal taken at 26.5°C on large plate with simulated defect and the signal obtained when subtracted from stretched reference (26°C); (b) Amplitude of the subtracted signal relative to amplitude of the first arrival in Figure 4.15(a).*

probable differences in the coupling of the simulated defects in the plates mean that precise quantitative comparisons should not be made. In Figure 4.16(b) it can again be seen that the "defect" produces large changes in the later parts of the signal due to the shadowing effects discussed earlier.

4.5 Influence of mode purity on temperature compensation strategy

To evaluate the influence of mode purity on the signal processing strategy described in section 4.4.5, signals were simulated analytically with the $A0/S0$ mode ratios which were obtained experimentally. The temperature variation was simulated by varying the dimensions of the plate and by changing the density, shear and longitudinal velocities of aluminium. These properties were obtained from data on the variation of elastic constants with temperature for monocrystalline aluminium found in [84]; this data was averaged according to [85] to give results for polycrystalline aluminium with crystals with cubic symmetry. This procedure was validated in [86] and used in [87] giving good results. The property values derived from this procedure were used as input data to obtain frequency versus wavenumber curves at different temperatures from the software DISPERSE [2]. These curves were then used to simulate signals analytically as discussed, for example, in [30].

This 2D simulation was based on a 5 mm thick, 0.6 m long, aluminium plate shown in Figure 4.17. The excitation was a 5-cycle Hanning windowed toneburst centred in turn at each of the frequencies used experimentally. Propagation of the A0 and S0 modes in this plate at 20°C and 30°C was simulated. The signal was generated at edge 1 and then reflected backwards and forwards through the plate, being monitored at point A. In this case there is no mode conversion as the plate is mid-plane symmetric. For each reflection from the edges, the signal was phase shifted by 90° in the A0 mode case, while in the S0 mode case a 180° phase shift was applied [88]. The time-traces obtained for the A0 mode and the S0 mode were considered sep-

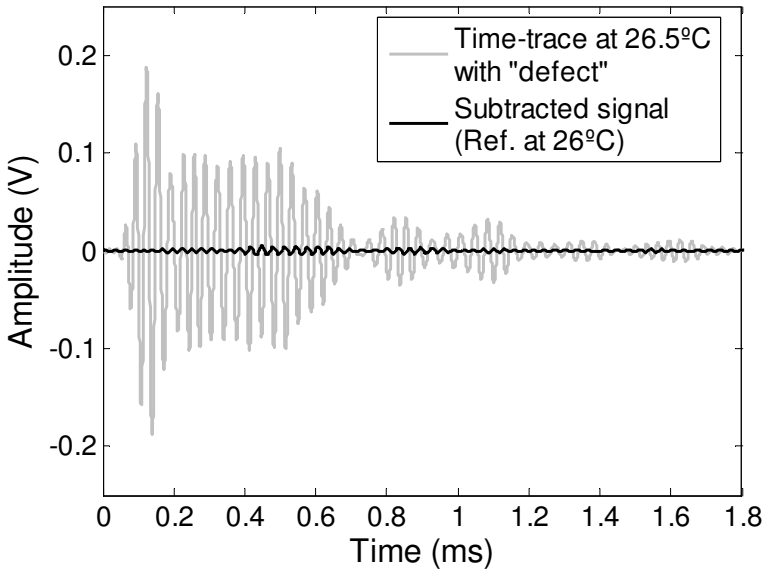

(a)

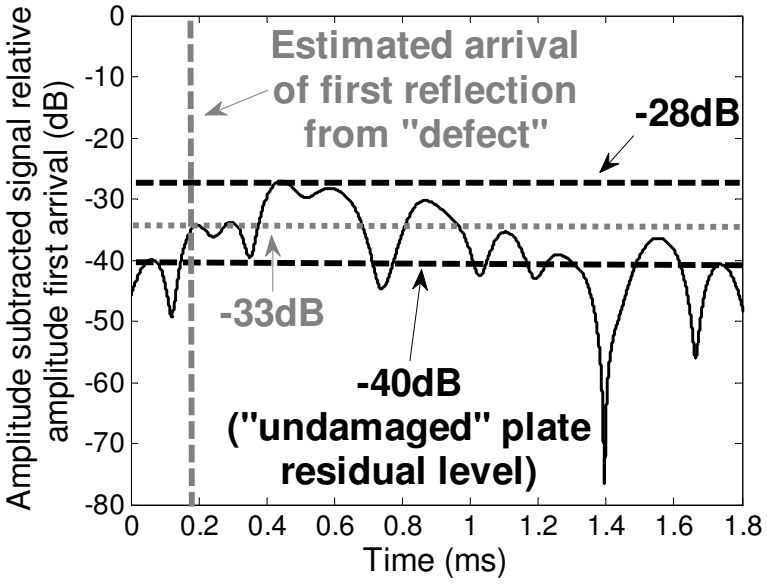

(b)

Figure 4.16: *(a) Signal taken at 26.5°C on small plate with simulated defect and the signal obtained when subtracted from stretched reference (26°C); (b) Amplitude of the subtracted signal relative to amplitude of the first arrival in Figure 4.16(a).*

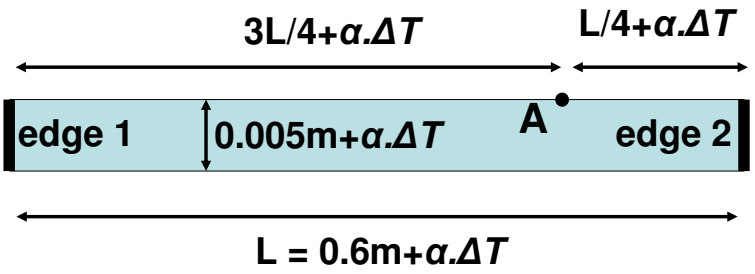

Figure 4.17: *Schematic diagram of geometry used for analytical simulation of signals with A0/S0 mode ratios similar to those obtained experimentally. As in section 4.2, α is the coefficient of thermal expansion and δT is the change in temperature (in this case a 10^oC increase).*

arately and were also added together to give signals with the $A0/S0$ mode ratios obtained in FE modelling of the transducers used in experiments. Section 3.3.1 described an FE model used to evaluate the mode purity of the two transducers used experimentally when they were operated in pulse-echo or pitch-catch mode. This model showed that when the simple piezoelectric disc was excited at 150kHz on a 5 mm-thick aluminium plate a S0/A0 mode voltage ratio of 17dB was obtained, whereas if it is excited at 200kHz it would give a ratio of 8dB for the same setup. The same model used in section 3.3.1 was used to model the A0 mode transducer described in chapter 3, and a A0/S0 mode voltage ratio of 73dB was found for a 6 mm-transducer on a 5 mm-thick aluminium plate.

The time-traces in the pure mode and in the mixed mode states were processed with the Optimal Stretch method to compensate for the 10°C difference between what was considered the reference signal (at 20°C) and the current signal (at 30°C). Figure 4.18(a) shows the time-trace resulting from the simulation of the propagation

of a 5-cycle Hanning windowed toneburst centred at 200 kHz, with a S0/A0 mode ratio of 8dB, in the geometry shown in Figure 4.17. There is a clear A0 mode wave packet at around 0.25 ms, indicated by the second dark arrow from the left, which is roughly 2.5 times smaller than the amplitude of the S0 mode. The other A0 mode wave packets overlap with wave packets of the S0 mode as would happen with signals obtained experimentally. Figure 4.18(a) also shows the signal resulting from the subtraction between the reference signal and the current signal after Optimal Stretch temperature compensation. Figure 4.18(b) shows the amplitude of the subtracted signal relative to the first arrival in Figure 4.18(a). For comparison, the amplitude of the residual signal relative to the first arrival, when the same procedure is applied to the signal obtained with pure S0 is also shown.

Figure 4.18(b) shows that the amplitude of the residual signal is increased in the regions where an A0 mode wave packet is present. This effect is most severe in later parts of the signal, reaching 15dB at 1.7 ms, where the propagation distance for the S0 mode is about 9 metres. For an S0 mode propagation distance of 5m, which is reached at around 1ms, the increase in amplitude levels in the residual signal was of the order of 10dB.

The increased residual at the arrival time of A0 reflections indicates that the Optimal Stretch required for the A0 mode is different to that required for the S0 mode. Figure 4.19 shows the variation of the rms value of the residual signal in the pure mode and mixed mode cases as a function of the percentage reduction of the frequency step size, Δf, in the spectrum, or the percentage stretch of the current signal. The minimum point in these curves corresponds to the Optimal Stretch. It is clear that the Optimal Stretch for pure A0 and pure S0 is different and that, as would be expected, the Optimal Stretch for an $S0/A0$ ratio of 8dB is close to that for a pure S0 mode. However, the minimum value of the rms of the subtracted signal for the mixed mode case is slightly higher than for the pure S0 mode case; this is due to the localised increases in amplitude at times where the A0 mode wave packets were present.

The difference in the amount of stretch needed to achieve the minimum rms value of

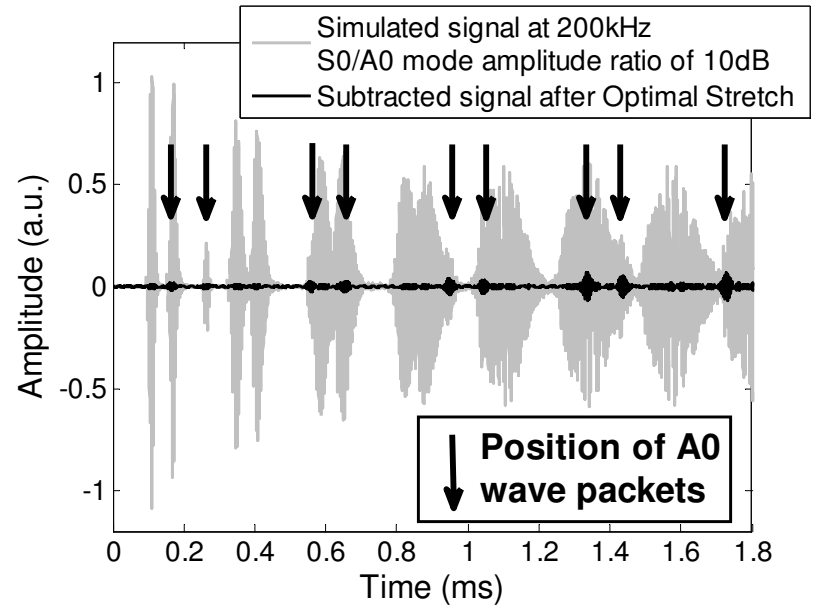

(a)

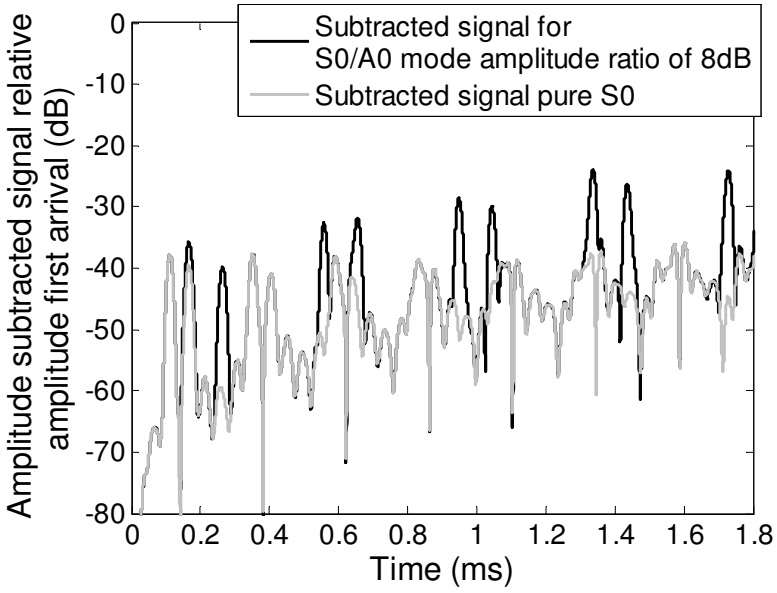

(b)

Figure 4.18: *(a) Simulated reference signal at 20°C and subtracted signal after Optimal Stretch of simulated current signal at 30°C, on structure shown in Figure 4.17, with a 8dB A0/S0 mode ratio; (b) Amplitude subtracted signal relative to amplitude first arrival for pure S0 at 200kHz and for signal with a 8dB A0/S0 mode ratio.*

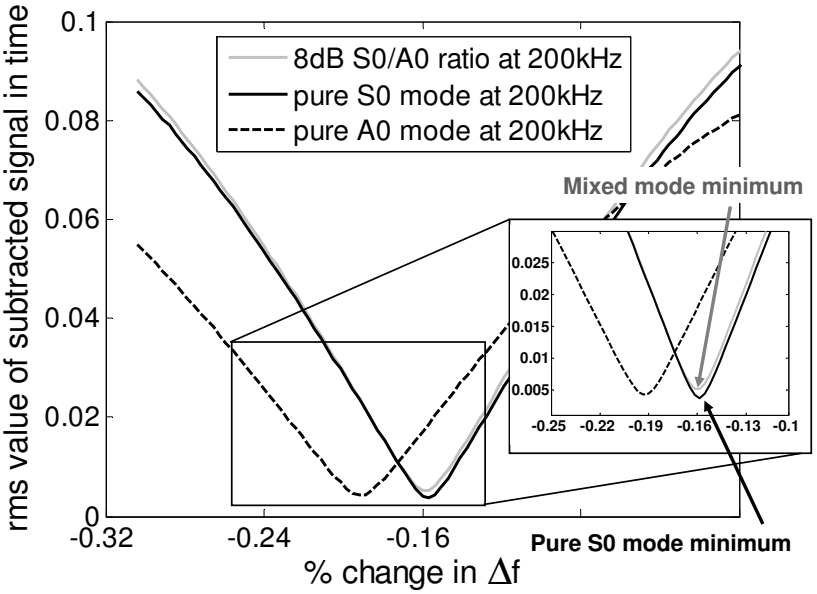

Figure 4.19: *Variation of position of minima in the rms value of the signal obtained from the subtraction between simulated reference signal at 20°C and simulated current signal at 30°C for pure A0 at 200kHz, pure S0 at 200kHz and a 8dB S0/A0 mode ratio.*

the subtracted signal for the A0 and the S0 modes during Optimal Stretch is a consequence of the effects described by Equation 4.6, which shows that δt is proportional to v_{ph}^{-1} and γ. The large differences in phase velocity (v_{ph}) in the frequency-thickness product region used in this work are the dominant cause of the differences in stretch values between modes; the fractional change in phase velocity with temperature (γ) is also mode dependent but has less influence on the results presented here. The difference between the modes is amplified if the temperature difference between the signals being compared is large, since δt is directly proportional to δT. This means that the residual caused by differences in stretch values for mixed-mode signals will increase with the temperature difference between the reference and the current signals.

To evaluate experimentally the influence of mode purity on the temperature compensation techniques presented earlier, pairs of the two transducer types described in chapter 3 were attached in turn to the 1 m-square plate, at the positions shown in Figure 4.7. The low-frequency A0 mode transducer was excited with a 5-cycle

toneburst centred at 35 kHz and this gave a A0/S0 mode ratio of 73dB in pitch-catch. The piezoelectric disc was excited with a 5-cycle toneburst centred at 150 kHz and 200 kHz, giving 17dB and 8dB S0/A0 mode ratios, respectively.

Figure 4.20(a) shows the results obtained using Optimal Stretch with a temperature difference of 0.5°C between the reference and the current signal taken from the system operating with the piezoelectric disc transducer at 150 kHz. The amplitude levels in the subtracted signal after Optimal Stretch achieved values close to the target levels (-38dB relative to the first arrival). Figure 4.20(b) shows the results with the same temperature difference between reference and current signal, for the same system at 200 kHz. In this case the worst case amplitude level resulting from the subtraction of the two signals after Optimal Stretch is -36dB.

Figure 4.21 shows the corresponding results with a temperature difference of 2°C between the reference signal and the current signal. The increase in the temperature gap between the two signals leads to an increase in residual levels to -35dB at 150 kHz and -30dB at 200 kHz. The results in Figures 4.20 and 4.21 are shown up to a time corresponding to a propagation of around 5m of the S0 mode.

When the signals obtained with the low-frequency A0 mode transducer pair were processed with 0.5°C and a 2°C temperature gaps between baseline and current signals, the worst residual signal level obtained after subtraction was -40dB and -39dB, respectively. This was expected since it was shown previously (Figure 4.12) that in this case a temperature gap of 5°C can be satisfactorily compensated for using Optimal Stretch.

The results in Figures 4.20 and 4.21 show that if the temperature difference between the baseline and the current signals is small, good levels of residual signal are obtained after subtraction by using the signal processing strategy described in section 4.4.5. However, if the temperature difference increases, the difference in the stretch factor required for the two modes becomes significant and the degree of mode purity becomes an important factor in the quality of the result obtained.

It is important to stress that mode purity is not the only factor in the difference

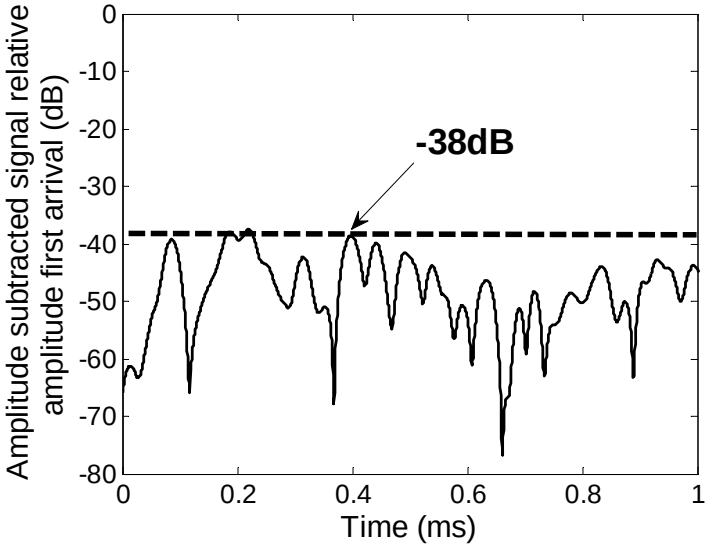

(a)

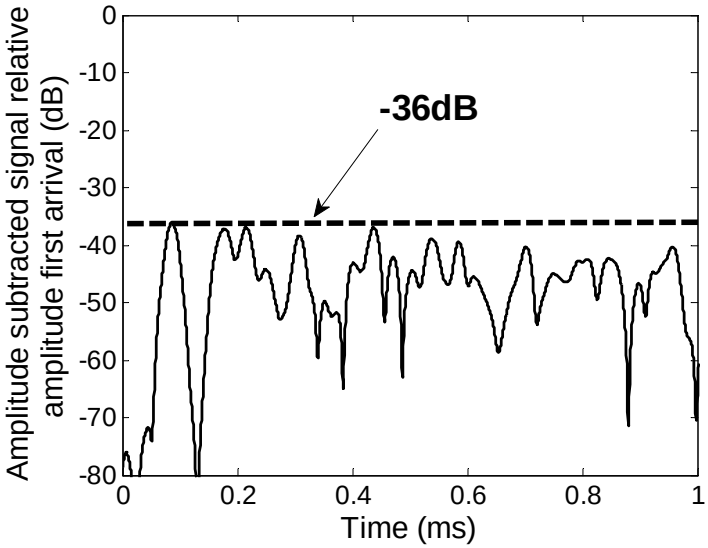

(b)

Figure 4.20: *Amplitude level in the residual signal relative to the first arrival, obtained after temperature compensation of a temperature gap of 0.5°C between a reference and a current signal taken with: (a) 17dB A0/S0 mode ratio (150kHz); (b) 8dB S0/A0 mode ratio (200kHz). Structure: large plate.*

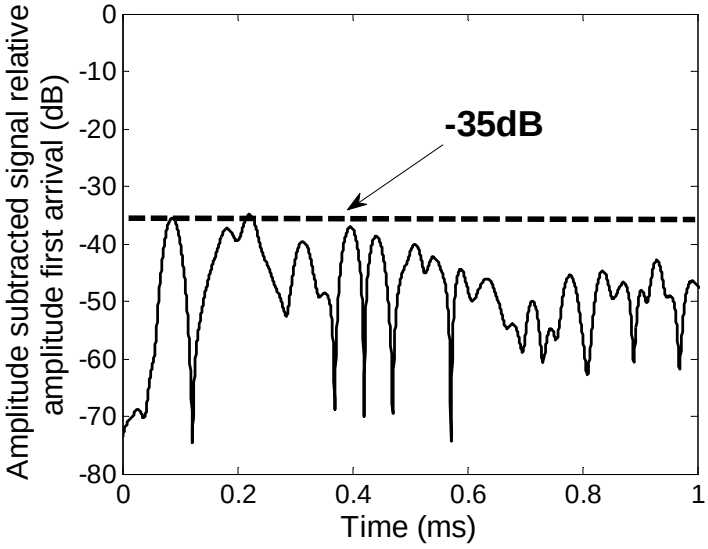

(a)

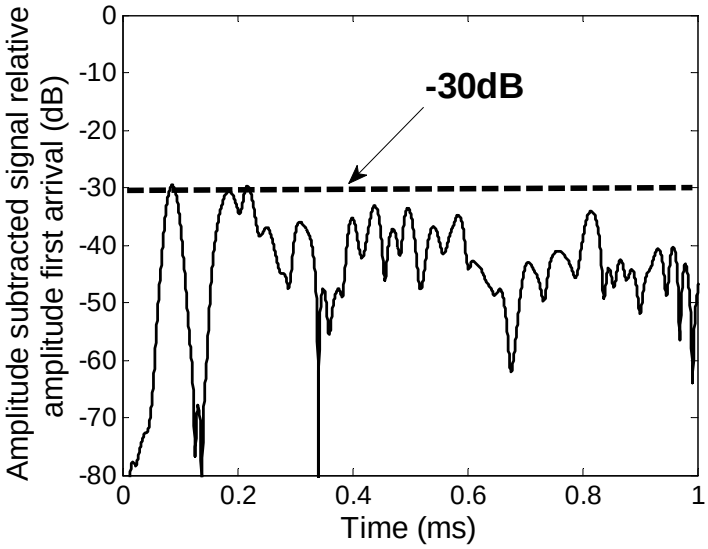

(b)

Figure 4.21: *Amplitude level in the residual signal relative to the first arrival, obtained after temperature compensation of a temperature gap of 2°C between a reference and a current signal taken with: a) 17dB A0/S0 mode ratio (150kHz); b) 8dB S0/A0 mode ratio (200kHz). Structure: large plate.*

between the residual of Figures 4.21(a) and 4.21(b). Equation 4.8 shows that the residual is proportional to the number of wavelengths propagated. A 5m propagation distance is equivalent to 138 S0 mode wavelengths at 150 kHz and 185 wavelengths at 200 kHz. Therefore, a difference of 2.5dB in the residuals at the two frequencies due to this effect would be expected. This suggests that the increase of 5dB between Figure 4.21(a) and 4.21(b) is half due to the effects of mode purity and half due to the increase in number of wavelengths propagated.

4.6 Inspection of a real structure

4.6.1 Airframe panel

As an example of inspection of a real structure, a section of an airframe panel was used as shown in Figure 4.22. The main structural features in this were steps in thickness (from 2 mm to 1 mm) and bonded stiffeners, as well as the edges. This panel was instrumented with 3 low-frequency A0 mode transducers as shown in Figure 4.23; in the results shown in this section transducer 3 was used as an emitter and transducers 2 and 1 as receivers. The system was placed in a room with no temperature control where temperature variations of up to 4-5°C were common. The acquisition system consisted essentially of the same equipment used for previous experiments, the only difference being the use of a multiplexer to switch between receiving channels. Signals were acquired every 2 hours over 3 weeks and this supplied a set of baselines in which temperature gaps between signals never exceeded 0.3°C.

It is known that large temperature gradients within the structure can limit the applicability of this temperature compensation strategy since this would invalidate the baselines collected previously. In this specific test, only small temperature gradients, below 1°C, were encountered; results which will be given in chapter 5 suggest however that temperature gradients of up to 2°C in large metallic structures can be accommodated by the compensation strategy.

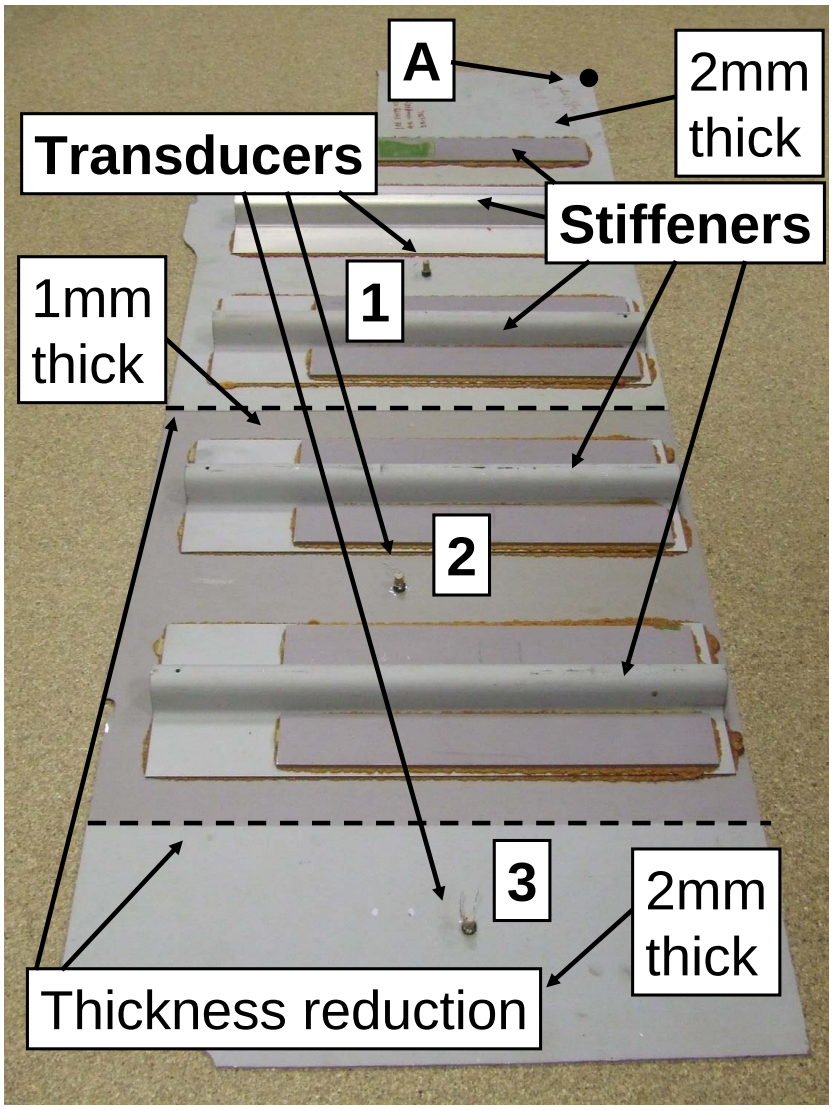

Figure 4.22: *Picture of airframe panel used for inspection of a real structure-like specimen.*

The features in the propagation path between the emitter (transducer 3) and the first receiver were a 50% reduction in thickness, from 2 mm to 1 mm, and a stiffener, while an additional two stiffeners and an increase in thickness back to that at the emitter were present in between the two receivers (transducers 1 and 2). The distance from the emitter to point A in Figure 4.23 and back to each of the receivers was considered the propagation distance needed to ensure complete coverage. This distance was 1.58

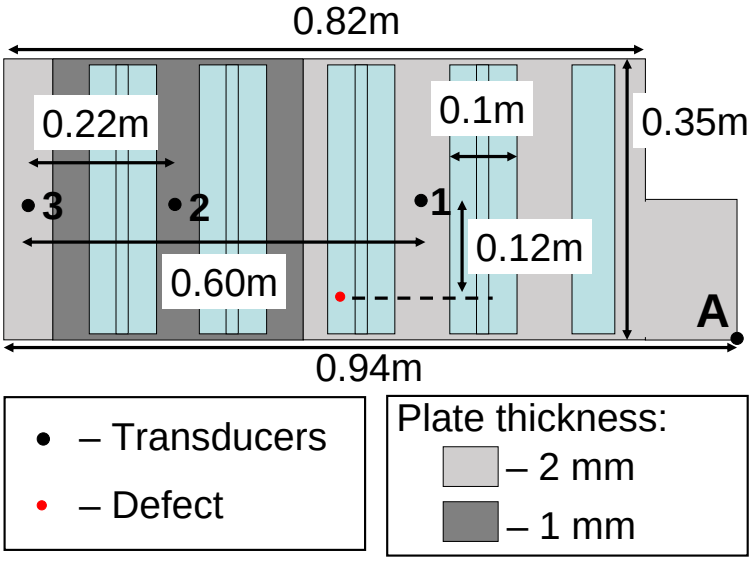

Figure 4.23: *Schematic of airframe panel used for inspection of a real structure-like specimen.*

m for receiver 2 and 1.28 m for receiver 1.

The signals obtained on this structure were processed with the Optimal Baseline Subtraction method alone and with the combined Optimal Baseline Subtraction and the Optimal Stretch techniques. Figure 4.24(a) shows the time-trace obtained at receiver 2 (see Figure 4.23). Signals are shown up to a time equivalent to a propagation distance of 3 meters for the A0 mode at 35 kHz. In Figure 4.24(a), the residual signal obtained after direct subtraction of the optimal baseline, which was a signal taken at the same temperature in the previous week, is also shown. The level of the residual signal relative to the amplitude of the first arrival in Figure 4.24(a) is shown in Figure 4.24(b). It can be seen that a residual level of -39dB is achieved up to times considerably above that needed for full coverage of the structure.

Figure 4.25(a) shows the signal received at receiver 1 on the airframe panel and the subtracted signal obtained after direct subtraction from the optimal baseline which was also taken at the same temperature in the previous week. Figure 4.25(b) shows that in this case residual signal amplitude levels of -38dB relative to the first arrival in Figure 4.25(a) are also obtained up to the time necessary for full coverage of the

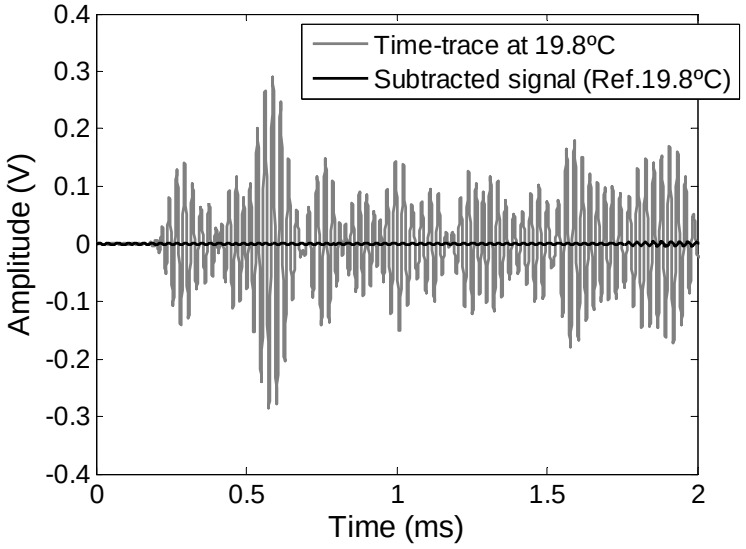

(a)

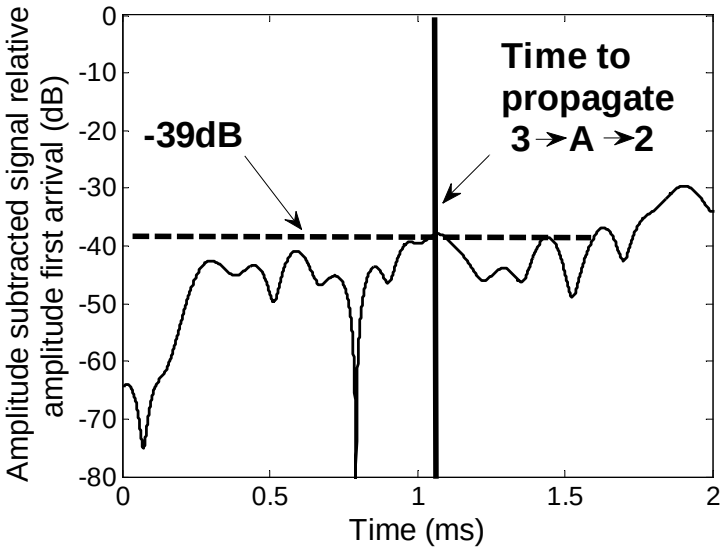

(b)

Figure 4.24: *(a) Signal taken at 19.8°C at receiver 2 on airframe panel and the residual signal obtained when subtracted from optimal baseline (19.8°C); (b) Amplitude of the subtracted signal relative to amplitude of the first arrival in Figure 4.24(a).*

panel.

Figures 4.26(a) and 4.26(b) show the result of processing signals obtained at receivers 2 and 1, respectively, when the signal processing strategy, consisting of the combination of the Optimal Baseline Subtraction method and the Optimal Stretch method, was applied to signals obtained from the structure at 21.4°C and 21.9°C, giving a difference of 0.5°C. Residual amplitude levels of -38dB are achieved up to times significantly above the time which is necessary for full coverage in both cases. These results show that this temperature compensation strategy is efficient in delivering residual levels as low as those found when the Optimal Baseline Subtraction technique is used alone, even though a smaller number of baselines in the database was used. If a 1°C temperature gap between baseline and current signal was used, the maximum amplitude level in the residual signal up to the time equivalent to full coverage increased to around -34dB relative to the first arrival. Therefore, in this case the complexity of the signals means that baselines must be acquired with a maximum temperature gap of around 0.5°C.

4.6.2 Defect detection in airframe panel

Defects in the form of holes of increasing diameter (1, 2.5, 3.5 and 5 mm) were introduced at the position indicated in Figure 4.23. The set of baselines of the undamaged structure considered in this section was acquired over two days at intervals of 20 minutes and again no temperature gap larger than 0.3°C was found in between baselines. With an interval of a day from the baseline capture, signals of the undamaged structure were taken and the first hole was drilled. Twenty signals were taken for each hole size with an interval of an hour to ensure that signals were taken over the widest temperature range possible. The temperature variations in this environment reached 3-4°C with gradients of around 1°C.

The objective of this experiment was to verify if the defect would be detectable with the database temperature gap of 0.5°C suggested in the previous section. Therefore a single baseline, taken at 23.5°C, was chosen to process signals taken at around 24°C

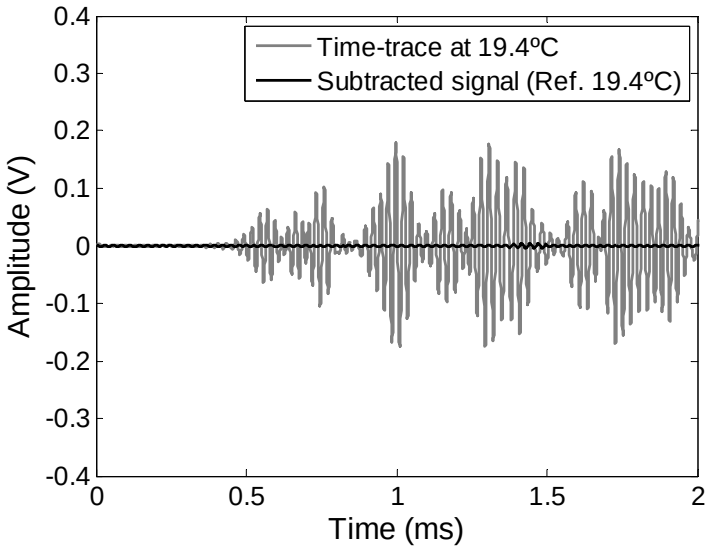

(a)

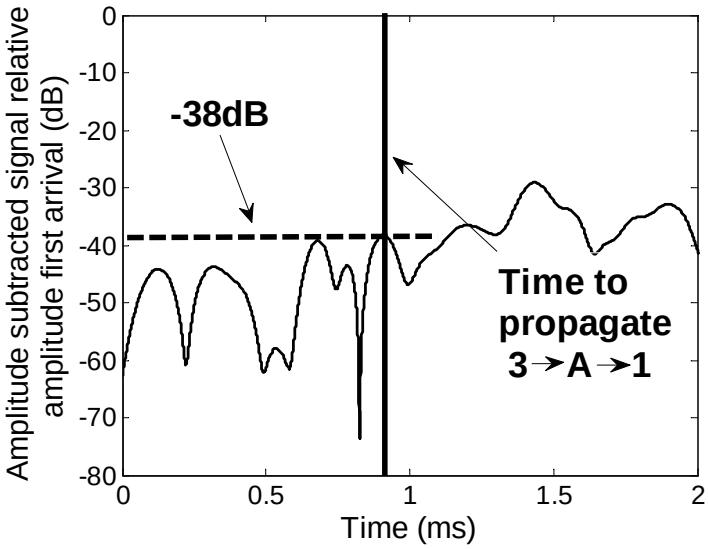

(b)

Figure 4.25: *(a) Signal taken at 19.8°C at receiver 1 on airframe panel and the residual signal obtained when subtracted from optimal baseline (19.8°C); (b) Amplitude of the subtracted signal relative to amplitude of the first arrival in Figure 4.25(a).*

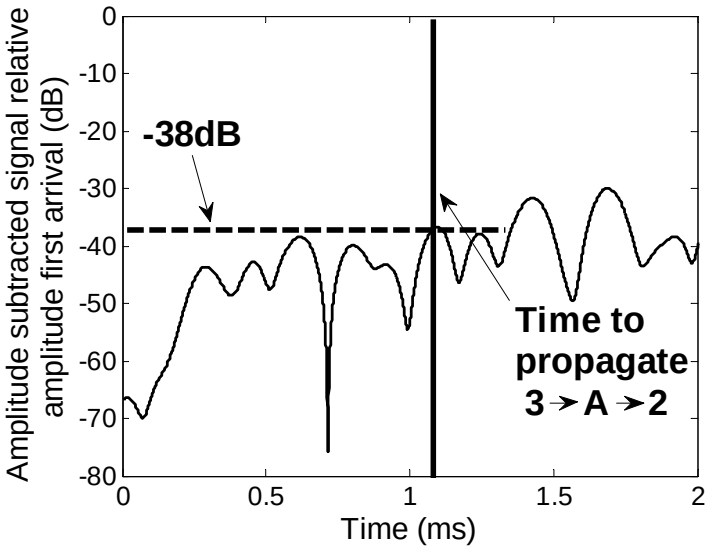

(a)

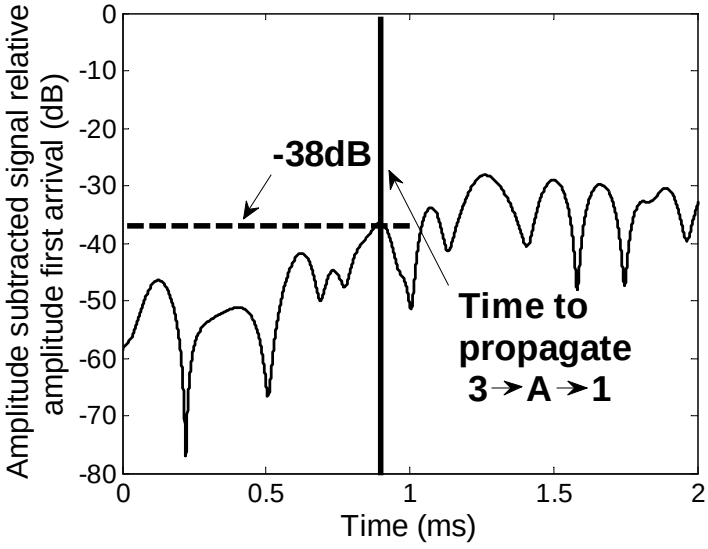

(b)

Figure 4.26: *Amplitude level in the residual signal relative to the first arrival, obtained after temperature compensation of a temperature gap of 0.5°C between a reference and a current signal taken at: (a) receiver 2; (b) receiver 1.*

for each state of the structure (undamaged and for each hole size). The emitter in this experiment was transducer 1 and the receivers were transducers 2 and 3 in Figure 4.23.

Figure 4.27(a) shows the baseline taken at 23.5°C from transducer pair 1-3, which was used for processing all signals, and the subtracted signal obtained after processing a current signal recorded at 24.1°C on the undamaged structure. The amplitude of the subtracted signal in Figure 4.27(a) is presented again in Figure 4.27(c), relative to the amplitude of the first arrival and as in the results shown in the previous section, the residual levels are close to -40dB. Figure 4.27(b) shows the subtracted signal obtained when the same baseline was used for processing a current signal recorded when a 5 mm hole was present in the structure, and an increase in amplitude values can be seen at the position where the arrival of the first reflection from the defect is expected. This can be more clearly seen on the dB scale of Figure 4.27(c) where a clear excursion above the worst amplitude in the undamaged structure subtracted signal can be seen at the expected position. Shadowing effects such as those described in section 4.4.6 cause substantial increases in residual levels at parts of the subtracted signals beyond the reflection from the defect. These effects are significant for this transducer pair and make identification of a single first reflection from the defect impossible. The explanation for such severity of shadowing effects for this combination of sensors is the location of the receiver; it is positioned 3 cm away from a strong reflector (the edge of the plate) and on a thin section of plate with 2 mm thickness, where energy is bound to be trapped causing significant reverberation and strong interference of reflections which can be easily disrupted. Figure 4.27(c) shows that an increase in amplitude is also seen at the expected position when a 2.5 mm-diameter hole was present, and this amplitude is slightly lower, as expected. A clear reflection from the 1 mm-diameter hole could not be seen in Figure 4.27(c); however, the presence of this hole did cause significant change to later parts of the signal due to shadowing effects.

Figure 4.28(a) shows the baseline recorded at 23.5°C and the subtracted signal for the undamaged structure from transducer pair 1-2; again, as can be seen from the

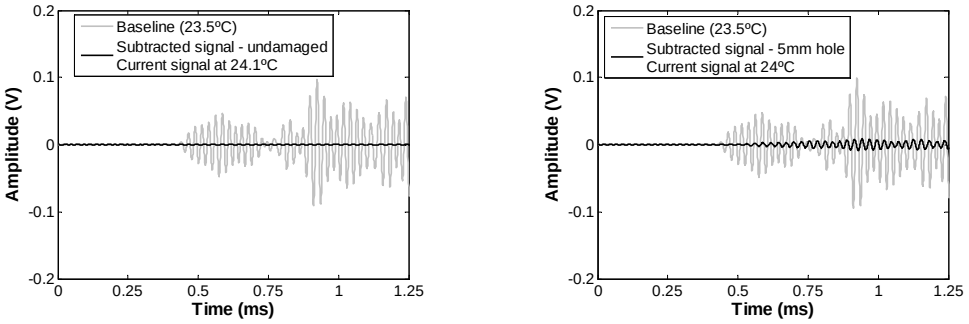

(a) (b)

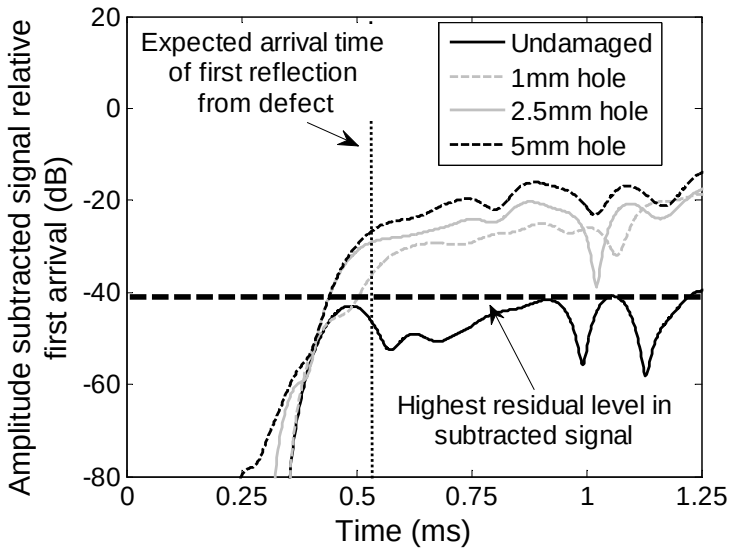

(c)

Figure 4.27: *Baseline obtained from transducer pair 1-3, and subtracted signal obtained after processing a current signal recorded at a temperature at least 0.5°C above the baseline temperature for: (a) the undamaged structure; (b) structure with a 5 mm hole. (c) Amplitude subtracted signal, relative maximum amplitude in signal up to a propagation distance of 1.5m, for the undamaged structure and the structure with 1, 2.5 and 5 mm holes.*

curve for the undamaged structure in Figure 4.28(c), residual levels close to -40dB were obtained. Figure 4.28(b) shows the same baseline and the subtracted signal obtained when a 5 mm hole is present in the structure, large values of residual amplitude being seen in later parts of the signal. Figure 4.28(c) shows that an increase in amplitude at the expected position of the first arrival from the defect is detectable above the limit value of the worst residual level of the undamaged structure. The 2.5 mm-diameter hole is also detectable above the limit value with a significantly lower amplitude than seen when the 5 mm-diameter hole is present. The first reflection from the 2.5 mm-hole is also more clearly seen than in the 5 mm-hole case since the larger hole size causes high values of residual in later parts of the signal due to stronger shadowing effects. Again, no clear reflection from the 1 mm-diameter hole could be seen in Figure 4.28(c) but increases in the amplitude of residual can be seen at later parts of the signal due to shadowing effects caused by the presence of this hole.

Analysing results from individual transducer pairs is an unreliable way of inspecting a structure since certain combinations will have better detectability than others, depending on the position of the defect. The results shown in this section demonstrate this effect, the defect being more easily identified with transducer pair 1-2 than 1-3. The ideal way to combine information from all possible transducer combinations is to use imaging algorithms, which will be introduced in the next chapter. It was not possible to apply these algorithms to the airframe panel described in this section because it is too small to be instrumented with a distributed sparse array which gives a large variety of combinations and angles of inspection. The experiments performed in this structure do however show the efficiency of the temperature compensation strategy presented in this chapter and that defects can be detected with this method in real complex structures.

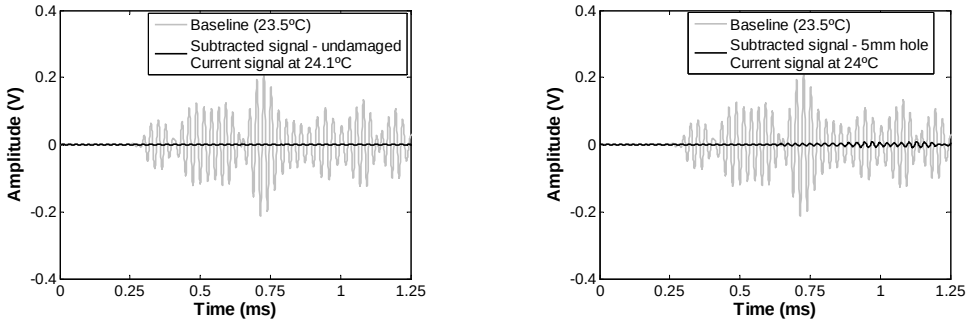

(a) (b)

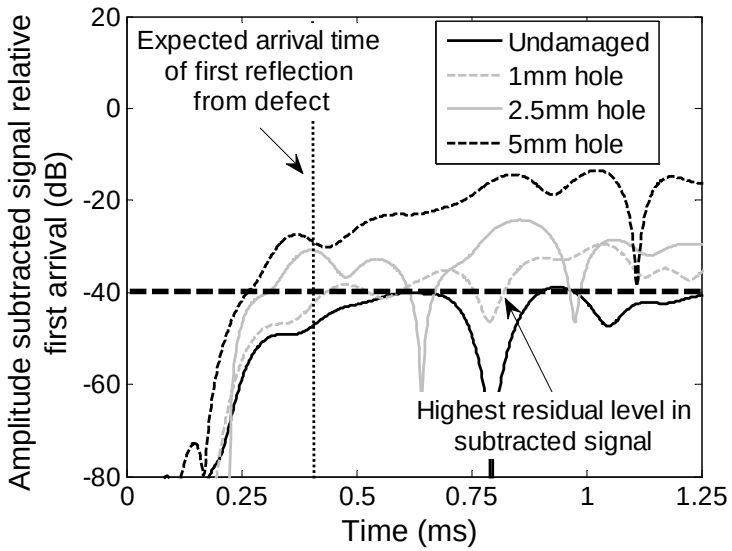

(c)

Figure 4.28: *Baseline obtained from transducer pair 1-2, and subtracted signal obtained after processing a current signal recorded at a temperature at least 0.5°C above the baseline temperature for: (a) the undamaged structure; (b) structure with a 5 mm hole. (c) Amplitude subtracted signal, relative maximum amplitude in signal up to a propagation distance of 1.5m, for the undamaged structure and the structure with 1, 2.5 and 5 mm holes.*

4.7 Summary

When the Optimal Baseline Subtraction method is used alone as a temperature compensation technique, a large number of baselines are needed since only small temperature steps (typically 0.1°C) will ensure amplitude levels in the residual signal which are low enough for good sensitivity (around -40dB relative to the first arrival). The success of the Optimal Stretch method is strongly dependent on mode purity and structural complexity. However, if signal complexity is low and mode purity is high, it is effective in compensating for a large temperature gap between reference and current signals (>5°C).

The Optimal Baseline Subtraction and the Optimal Stretch methods can be combined to form a robust temperature compensation strategy. This reduces the number of baselines necessary to ensure good sensitivity in comparison to that needed when the Optimal Baseline Subtraction technique is used alone. The reduction in the number of baselines in the database is limited by the maximum temperature gap between baselines which can be compensated for by the Optimal Stretch without loss of sensitivity; this is a function of mode purity, signal complexity and the maximum propagation distance to cover the whole structure expressed in wavelengths. In some cases, especially when the signal complexity is high or when mode purity is insufficient, the temperature gap between baselines needed for good sensitivity can drop to as low as 0.5°C, as was seen for the airframe structure inspected. In this case, the signal processing strategy gave a residual of -38dB with a temperature gap of 0.5°C, when high mode purity was used. If the temperature gap was increased to 1°C the residual amplitude was worsened, to -34dB.

When this signal processing strategy was used to process signals obtained from undamaged plates and from the same plates with simulated damage, a first excursion above the residual level for the undamaged structure was seen at the expected position of the first reflection from the "defect". Large increases in later parts of the residual signals were also seen, indicating good sensitivity to changes in the structure. Defects as small as 2.5 mm were detected in a complex airframe structure, thus

validating the efficiency of the signal processing strategy described in this chapter in inspecting a real structure.

It is important to note that other factors other than the ones described (signal complexity, mode purity, wavelength of the mode of choice) can affect the efficiency of the signal processing strategy described and demonstrated in this chapter. Examples of these effects are factors other than changes in temperature, such as loading of the structure and changes in liquid or viscoelastic layers present on the surface of the structure (such as a water layer or paint), which affect the wave velocity in the same way as temperature. If two or more of these are present, the size of the database might become excessively large and complex. Another issue is large temperature gradients within the structure, which are not supported by the technique. One way of avoiding these effects is to only inspect when the structure is unloaded and protected from direct sunlight exposure (such as an airplane in a hangar) or during night time. For this, the guided wave SHM system could be integrated with other sensors measuring stresses which could act as a trigger for inspection when certain conditions are met. Large temperature gradients can be detected from the signals gather by the guided wave SHM system itself as described in [55], and inspection can be avoided when these are present.

Chapter 5

Defect localization in a real structure

5.1 Introduction

This chapter shows the results obtained when a sparse-array guided wave SHM system was applied to a shipping container panel subjected to uncontrolled temperature variations in a non-laboratory environment. Initially, the suitability of the A0 and S0 modes for this particular structure was evaluated by studying transmission across the corrugations of the panel in finite element models. Experimentally, baselines were acquired from the sparse array over several weeks and the stability of the temperature compensation and baseline subtraction techniques presented in Chapter 4 was assessed. Defects of different diameter were machined in the structure and the detection capability of the system was verified. This was performed by processing the data with imaging algorithms which allowed the information of all possible transducer combinations to be combined, thus increasing the reliability of defect detection in relation to simple analysis of individual subtracted signals. The results shown in this chapter have been submitted for publication [70].

Many of the parameters of the experimental procedures adopted will be found in the text of this chapter. Appendix B gives a more detailed description of the procedures.

5.2 Structure and Mode propagation

5.2.1 Structure and transduction

The structure used in this work was the door of a shipping container, as shown in Figure 5.1(a). This consisted of a corrugated 2 mm-thick steel sheet welded to a box-beam frame made of 12.5 mm-thick steel. The panel was instrumented with two permanently attached 9-sensor sparse arrays of identical geometry (Figures 5.1(a) and 5.1(b)); the first array was formed by the transducer generating high-purity A0 mode at 35 kHz, and the second by the transducers generating mostly S0 mode at 100 kHz, both of which were described in Chapter 3.

Figures 5.2(a) and 5.2(b) show signals obtained from the A0 and S0 mode sparse arrays with amplitudes corrected for beam-spreading effects, as in [79]; two pitch-catch combinations were chosen for each sparse array since the signals obtained by these transducer pairs involved crossing the corrugations at different angles. Transducer pairs 6-5 and 15-14 had incidence angles on the corrugations of 0^o, while pairs 6-2 and 15-11 had incidence angles of 32^o. Figure 5.2(a) shows the signals obtained from the A0 mode array for the two incidence angles, the amplitude of the first arrival between 6-5 being 7 times higher than for 6-2. In Figure 5.2(b), where the signals for the S0 mode array transducers are shown, the difference in amplitude of the first arrivals between transducer pairs 15-14 and 15-11 is only 50%. These results show that propagation within the structure is highly dependent on the mode being used and the direction of propagation. These effects were evaluated further by finite element modelling as described below.

5.2.2 Modelling of mode propagation

The interaction of the A0 mode at 35 kHz ($\lambda_{A_0} = 35mm$) and the S0 mode at 100 kHz ($\lambda_{S_0} = 50mm$) with the structural feature present in the container panel was studied by 3D finite element (FE) modelling. The objective of this study was to evaluate the

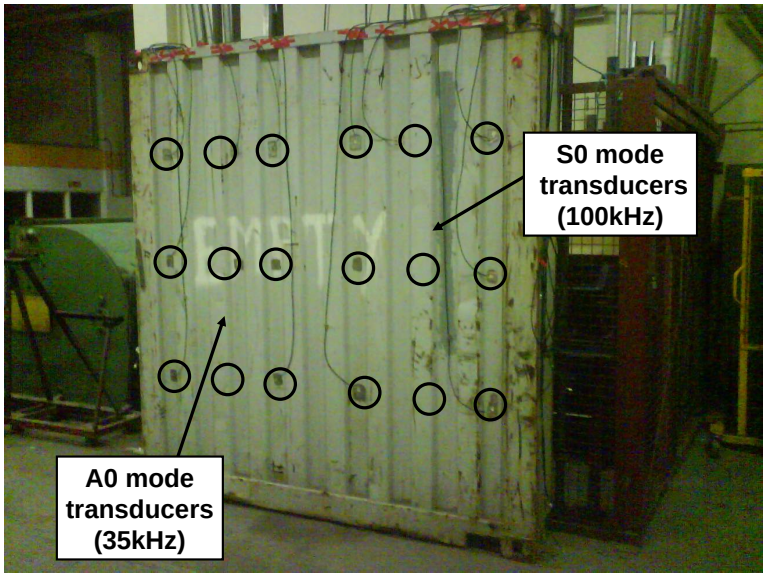

(a)

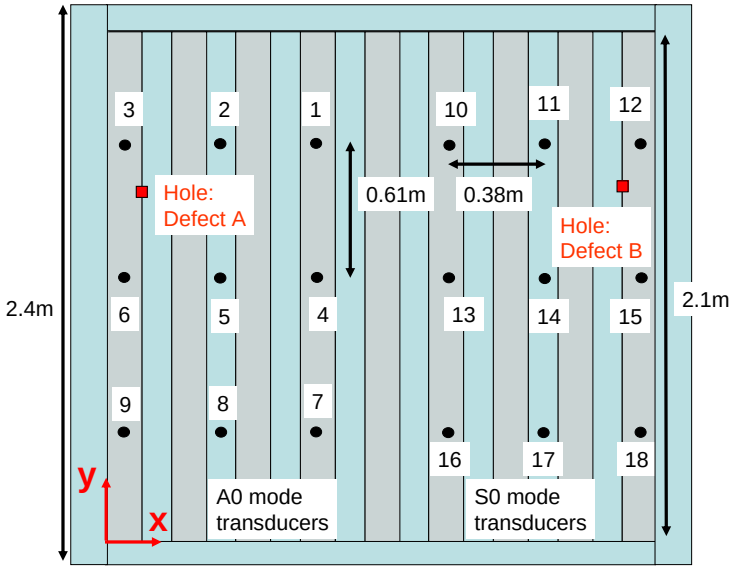

(b)

Figure 5.1: *(a) Container panel and transducer grid; circles indicate transducer locations; (b) Schematic of container panel with dimensions; circles indicate position of transducers, squares indicate position of defects.*

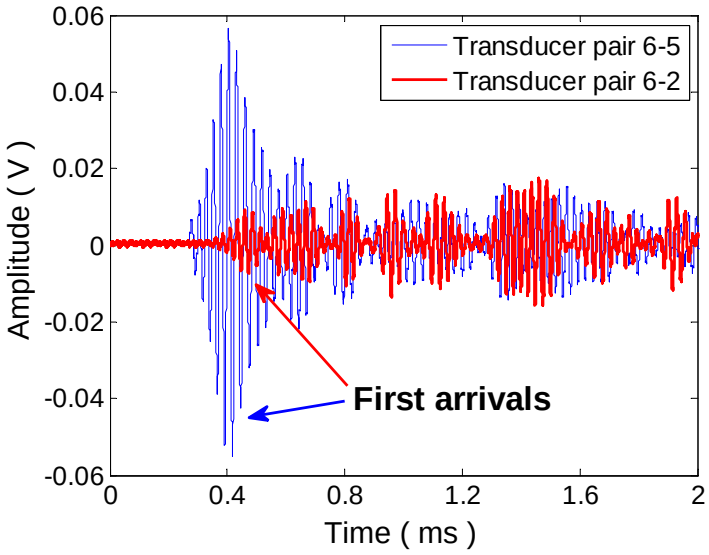

(a)

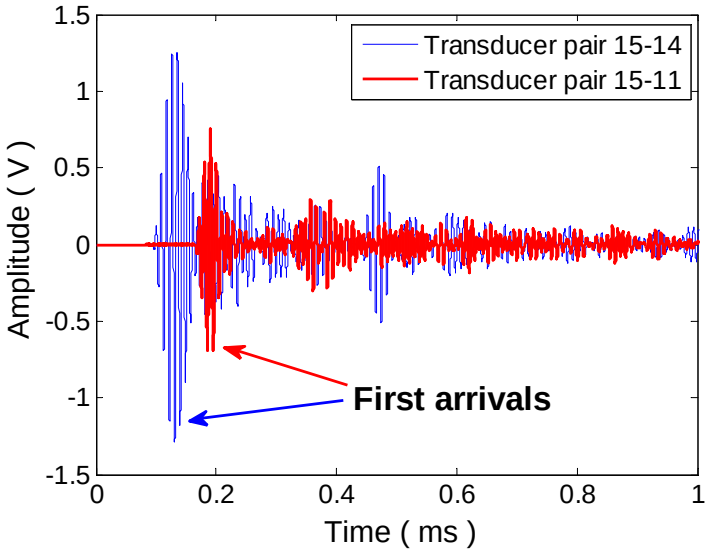

(b)

Figure 5.2: *(a) Measured pitch-catch signals between transducer pairs 6-2 (32° incidence angle on corrugation) and 6-5 (0° incidence angle); (b) Measured pitch-catch signals between transducer pairs 15-11 (32° incidence angle) and 15-14 (0° incidence angle).*

transmissibility of each mode by obtaining reflection and transmission coefficients as a function of the incidence angle of a wave front on the structural feature found in the container panel. The corrugation of the steel plate, which repeated itself a number of times along the width of the structure, had a cross-section with dimensions as shown in Figure 5.3(a). A plate with a single corrugation, with dimensions as shown in Figure 5.3(b) was modelled; to generate this model, 1.5 mm-long brick elements with a 1 mm square section were used, so that 2 elements were present through the thickness of the plate. These elements had all dimensions at least 10 times smaller than the smallest wavelength in the model. To avoid unwanted reflections from the edges of the plates an absorbing region was included in the plates and corrugation. This was done by gradually increasing the values of damping of the elements in the outer region of the plate, as discussed in [71]. By using such an absorbing region the amplitude of reflections from edges was reduced by more than 50dB.

Point-source excitation was introduced at a point close to the absorbing region as indicated in Figure 5.3(b). This meant that only a quarter of the circumferential wave front generated was used to obtain the angular reflection and transmission coefficients since most of the circumferential wave front generated was lost in the absorption region; however, this was enough to define the reflection and transmission characteristic of the wave front interaction with the corrugation since it is symmetric. Point source excitation of the A0 mode was performed by applying an out-of-plane displacement to all the nodes through the thickness of the plate, in the form of a 3-cycle Hanning windowed toneburst at 45 kHz; the S0 mode was excited by using the technique described in [89], where an in-plane point-like source is simulated by applying radial forces to 8 nodes symmetrically placed on a circle of the same diameter as the transducers used in the experimental setup; the input signal was a 3-cycle Hanning windowed toneburst centred at 120 kHz. Lines of monitoring points were included at the position showed in Figure 5.3(b), and the spacing between monitoring nodes was two elements (3 mm). The line on the opposite side of the corrugation was used to evaluate transmission coefficients while the line on the excitation side was used to calculate reflection coefficients.

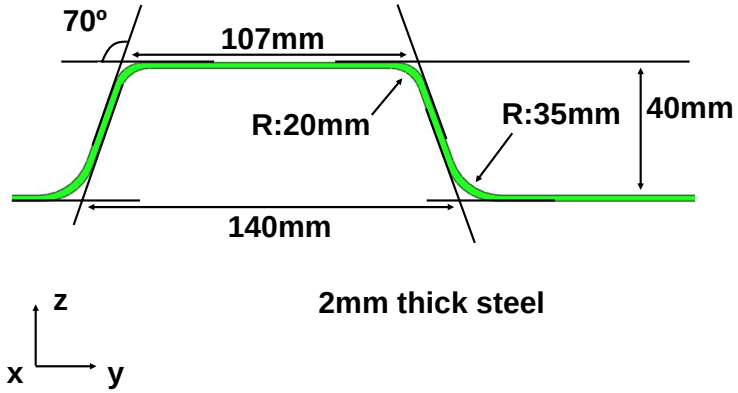

(a)

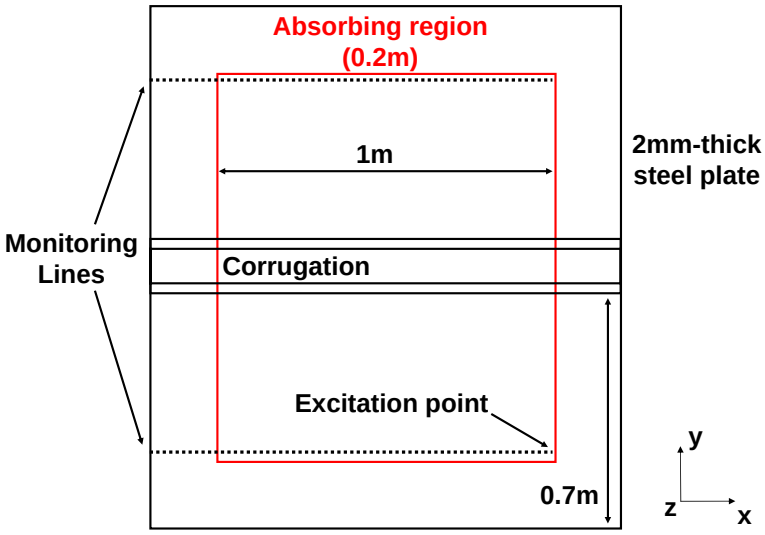

(b)

Figure 5.3: *(a) Detailed container feature; (b) Schematic of finite element model used for obtaining angular reflection and transmission coefficients, with dimensions of the plates and absorbing region. Red line indicates initial elements of absorbing region.*

Data obtained from the FE model was processed to obtain the angular spectrum of each mode; the aim of this signal processing technique is to decompose a circumferential wave front, such as those generated by a point source, into a number of plane wave fronts with different angles. If one of the lines of monitoring points along the x-axis shown in Figure 5.3(b) is considered as an array, the first requirement for calculating the angular spectrum for this array is that the amplitude values at a given frequency of the spectra of received signals at each monitoring point of the array should be selected, so giving a monochromatic field $f(x)$, and processed independently. It is important to compensate the amplitudes for beam-spreading before processing, as demonstrated in Equation 4.9. The angular spectrum $F(k_x)$ is the spatial Fourier transform of $f(x)$ [90], defined as:

$$F(k_x) = \int_{-\infty}^{\infty} f(x) e^{-jk_x x} dx \tag{5.1}$$

where k_x is the wave number component in the x-direction. If only the propagating waves are considered, the wave number vector in the x-direction, k_x, is related to k_y, by [90]:

$$k_y = \sqrt{k^2 - k_x^2} \tag{5.2}$$

where $k = \frac{2\pi}{\lambda}$ is the wave number of the emitted wave at the frequency considered for $f(x)$. The angle Θ between k_x and k can be obtained by trigonometry:

$$\Theta = \cos^{-1}\left(\frac{k_x}{k}\right) \tag{5.3}$$

and the incidence angle of the input signal on the corrugation will be $180^{\circ} - \Theta$ (in degrees).

Performing the computation above for all values of frequency in the bandwidth of the input signal leads to the frequency-dependent angular spectrum plot. It is clear

from Equations 5.2 and 5.3 that for this method to perform correctly, a single mode must be present, since only one value of k can be included in the calculations. In the FE modelling this was guaranteed in two ways: when the A0 mode was excited, the out-of-plane displacement was monitored at the mid-thickness node, where such a displacement is characteristic of this mode only (see Figure2.3); when the S0 mode was excited the in-plane displacement in the y-direction at the mid-thickness node was monitored, which could lead to measurement of S0 and converted SH0; however, the distances chosen for the model allowed the separation in time of wave packets related to the two modes, due to their different group velocities.

A model with the same dimensions as Figure 5.3(b) but without the corrugation was also run to obtain the frequency dependent angular distribution of the input signal. The transmission and reflection coefficients as a function of incidence angle were then obtained by dividing the scattered angular spectrum by the angular spectrum of the input signal over the frequency range of the input.

The transmission and reflection coefficients for the A0 mode are shown in Figure 5.4(a) and 5.4(b) respectively. It is clear that very little signal is transmitted in the 35 kHz frequency region at angles larger than 25°. High values of displacement within the corrugation are seen in the snap-shot of the motion in the model in 5.5, suggesting that energy was trapped there. Figure 5.6(a) and 5.6(b) show the transmission and reflection coefficients of the S0 mode around 100 kHz; here the transmission coefficient is much higher and relatively independent of angle. To validate the models and the angular spectrum post-processing of the data, the reflection (R_c) and transmission (T_c) coefficients of Figure 5.4 or 5.6 were added to verify energy conservation of the scattered field; the resulting frequency vs. incidence angle plot indicated that total energy ($R_c + T_c = 1$) was obtained with an error smaller than 10% for both the A0 and S0 modes, thus proving that the results are sound and indicating that little mode conversion occurs.

The average transmission coefficient for the A0 mode over the bandwidth of the experimental input signal at 0° incidence angle calculated from the FE results shown in Figure 5.4(a) is 0.74 whereas this drops to 0.11 at 32° incidence angle. For the S0

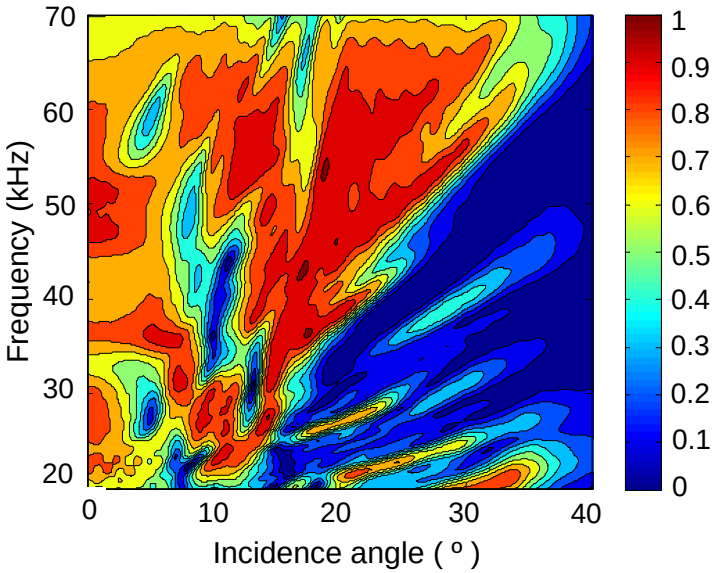

(a)

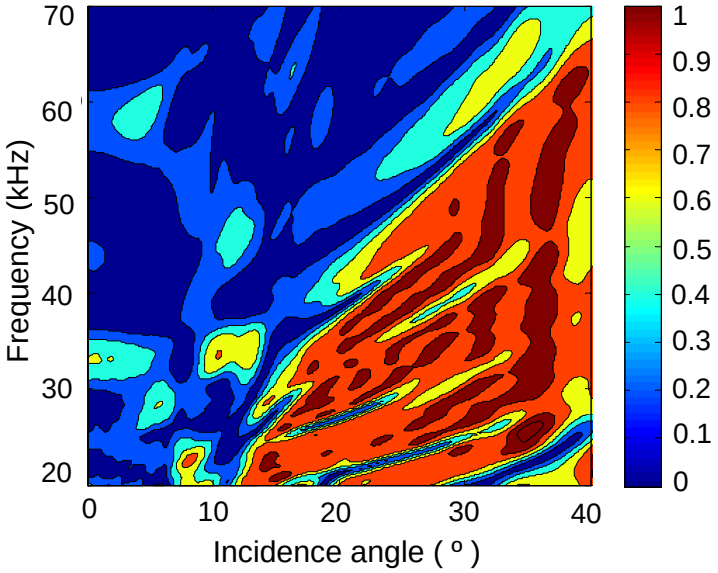

(b)

Figure 5.4: *(a) Predicted transmission coefficient as a function of the angle of incidence of the A0 mode on container feature; (b) Predicted reflection coefficient as a function of the angle of incidence of the A0 mode on container feature.*

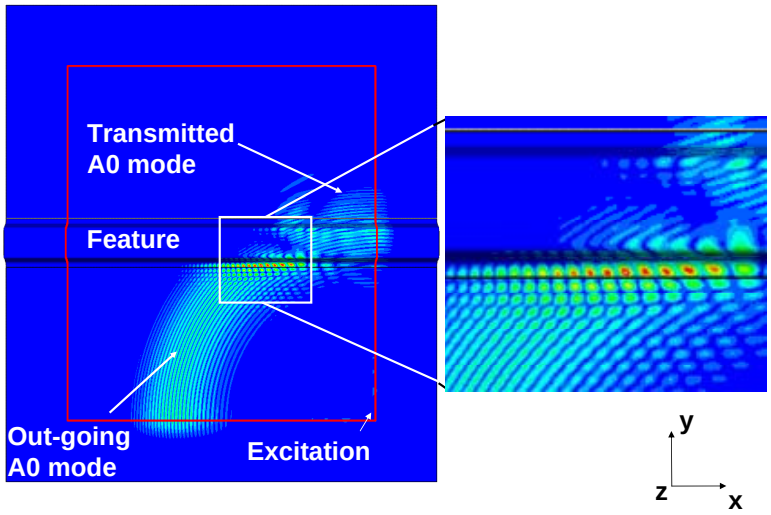

Figure 5.5: *Snap-shot of finite element simulation result used for obtaining angular reflection and transmission coefficients for the A0 mode, showing resonance in the feature.*

mode, the average transmission coefficient at 0° incidence angle is 0.62, reducing to 0.45 at 32°. The more uniform transmissibility of the S0 mode means it is the better mode to use for the inspection of this particular structure so only results obtained with the S0 mode sparse array are presented in the following sections.

5.3 SHM experiments

5.3.1 Experimental Procedure

The container panel was placed in the goods inwards area of the building close to a large roller door and was subjected to uncontrolled temperature swings. The temperature was monitored at each transducer by type-K thermocouples measuring relative temperature variations to a precision of 0.1°C; during the 9 week period in which the experiment was performed, ambient temperature differences of 8°C were measured. Temperature gradients of up to 2°C between sensors were commonly seen; at night, when the temperature of the storage room was relatively constant

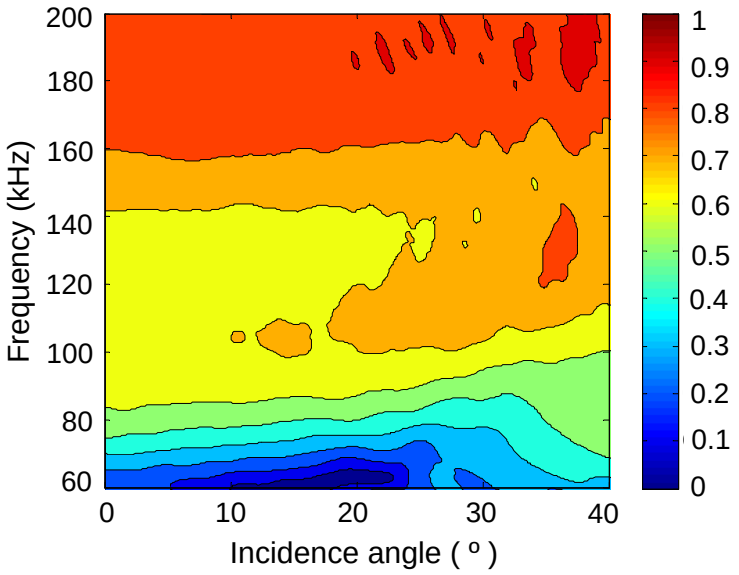

(a)

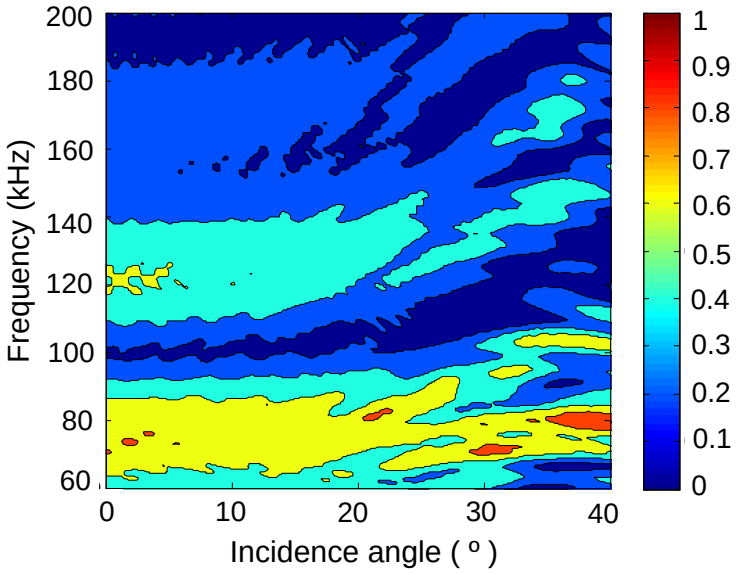

(b)

Figure 5.6: *(a) Predicted transmission coefficient as a function of the angle of incidence of the S0 mode on container feature; (b) Predicted reflection coefficient as a function of the angle of incidence of the S0 mode on container feature.*

due to the large access door to the storage room being closed, gradients were smaller than 0.2°C. This suggests that the gradients of around 2°C seen at other times are genuine, and not solely due to thermocouple calibration errors.

A PC was used to upload input signals to an arbitrary function generator (Agilent 33220) which was connected through an amplifier (Krohn-Hite 7602) to a custom built multiplexer. Received signals were pre-amplified (Krohn-Hite 3988) before returning to the multiplexer. A Labview routine was used to control the emitter-receiver channel selection of the multiplexer, and to save the signals displayed on an oscilloscope (LeCroy 9310A) set to 100 averages.

Only pitch-catch measurements were performed with the transducers of the S0 mode array shown in Figures 5.1(a) and 5.1(b); because of the symmetry of the transmitter-receiver matrix, only half of the combinations were acquired, leading to 36 measurements for each test. The total time necessary for collection of all signals was around 15 minutes. One set of baselines was acquired for all transmit-receive combinations; this was done over 3 weeks at 2-hour intervals and this procedure guaranteed a comprehensive database, with no temperature gaps larger than 0.3°C in between baselines. One week later, a set of 10 signals from the undamaged structure was taken, before a defect in the form of a drilled hole was introduced to the panel at point "A" in Figure 5.1(b). The initial diameter of the hole was 1 mm; this was later increased to 2.5, 5 and 10 mm. For each hole drilled 10 signals were acquired for all transmitter-receiver combinations, over a period of one day. After these measurements were performed, the system was left idle for 4 weeks; in the fifth week the same drilling procedure was applied to point "B" in Figure 5.1(b), 10 signals again being acquired over a period of one day for each hole size.

5.3.2 Results of direct analysis of subtracted signal

The 10 "current" signals recorded for each transmitter-receiver combination in the sparse array for each condition of the structure (undamaged and for each damaged state) were processed with the temperature compensation strategy described

in Chapter 4, leading to 10 subtracted signals. These were averaged to produce a final subtracted signal which was then compensated for beam spreading, following Equation 4.9.

Figure 5.7(a) shows the averaged subtracted signal obtained for transducer pair 16-13 when a 10 mm-diameter hole was introduced at position "A" (see Figure 5.1(b)); for comparison, the Optimal Baseline for one of the processed current signals is also shown. The expected arrival time of the first reflection from the defect is marked in Figure 5.7(a) at 0.57 ms; the distance of the propagation path between the transmitter-defect-receiver is 3.1m ("unfolded" distance, i.e. propagation length equivalent to flat plate, allowing for travel up and over the corrugations) and the group velocity of the S0 mode at 100 kHz is 5450 m/s. A clearer representation of the subtracted signal is obtained by using a dB scale, where the amplitude of the subtracted signal is related to the amplitude of the first arrival of the current signal. As mentioned in Chapter 4, reflections from defects of interest in large area SHM are expected to be of the order of -30dB or lower, so the target level of amplitude in the subtracted signal in such a plot is -40dB or lower. Figure 5.7(b) shows that this is comfortably achieved, the maximum amplitude obtained in the subtracted signal of the undamaged structure being -52dB. No signals above the -52dB level seen in the undamaged case were obtained when holes with diameters smaller than 10 mm (roughly 20% of the wavelength) were present in the structure, and these results will therefore not be shown. When the 10 mm-diameter hole was present at "A" a small first excursion above the highest amplitude level in the undamaged case is seen slightly before 0.57 ms, and large amplitudes are present in later parts of the signal; this is due to shadowing effects caused by the presence of the defect, which means that reflections from structural features in more distant regions of the panel will have their amplitudes modified in relation to the baseline signal, leading to large residuals in the subtraction.

Figure 5.8(a) shows the subtracted signal from transducer pair 13-10 obtained for the undamaged structure and when a 10 mm-diameter hole is present at position "A". Again, the residual signal level for the undamaged structure is better than the

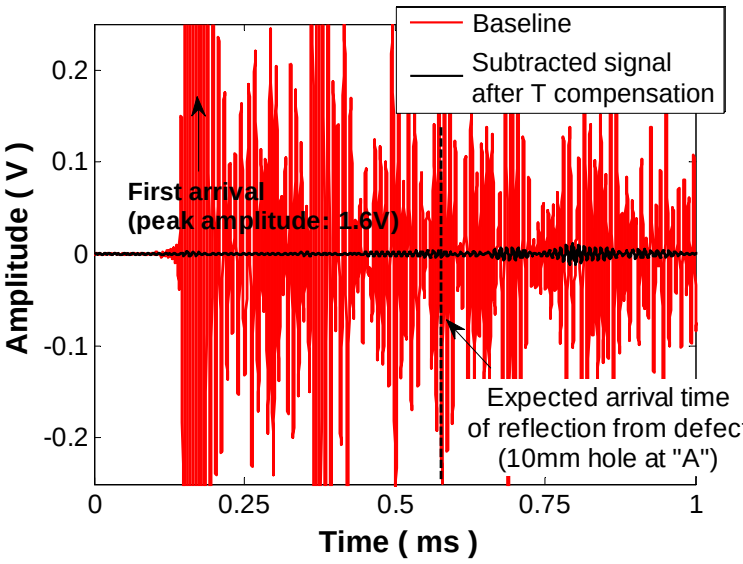

(a)

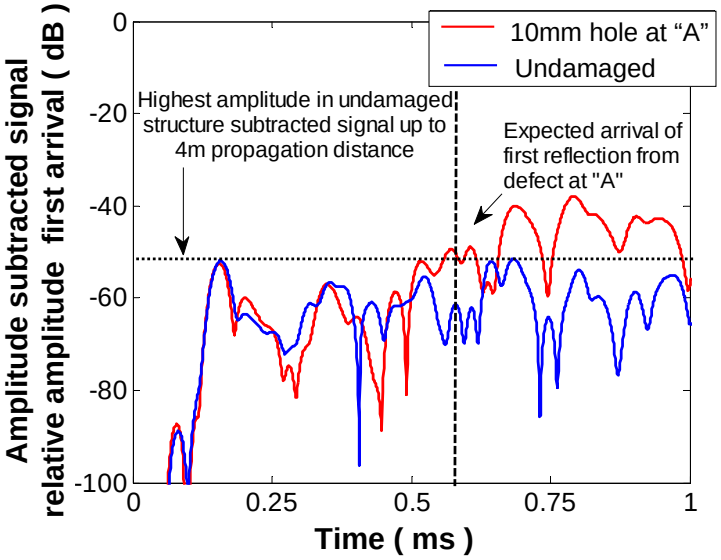

(b)

Figure 5.7: *(a) Baseline and subtracted signal resulting from averaging of 10 processed signals for transducer pair 16-13, for the structure with a 10mm-diameter hole at position "A" in Figure 5.1(b); (b) Amplitude of the subtracted signal relative to the amplitude of the first arrival for the undamaged structure and the structure with a 10mm-diameter hole at position "A" in Figure 5.1(b).*

target levels, at -55dB up to 4 m propagation distance. When a 10 mm-diameter hole is present at "A", a small first excursion is seen at the expected position of 0.52 ms. Since the transmitter-defect-receiver distance is 2.85 m, and shadowing effects cause larger amplitude levels in later parts of the signal. Detection of reflections from smaller holes was also not possible with this transducer pair.

The subtracted signal obtained from transducer pair 13-10 when a 10 mm-diameter hole was present at position "A" is shown again in Figure 5.8(b); the comparison in this figure is with the subtracted signals obtained when additional 5 mm- and 10 mm-diameter holes were present at position "B" for the same transducer pair. Since the same set of baselines was used to process all the signals, the subtracted signals obtained when holes were present at position "B" also contained information on the presence of the previously introduced 10 mm-diameter hole at "A"; however, changes in the signals due to the presence of the hole at "A", either in the form of a direct reflection or shadowing effects, were expected at later times than required for coverage of the entire right-hand side of the panel, which is the area which the S0 mode sparse array was designed to cover, and where hole "B" was located. The propagation path transmitter 13 - defect "B"- receiver 10 is 2.12 m, and the expected arrival time of a reflection from defect "B" would be 0.38 ms. Figure 5.8(b) shows that a clear increase in amplitude is seen at 0.38 ms due to 5 mm- and 10 mm-diameter holes. Figure 5.8(b) shows that although the excursion in the 5 mm hole case does not exceed the maximum residual in the undamaged signal over the whole 4 m propagation range, it is clearly detectable if a shorter range is considered, e.g. up to 0.5 ms propagation time (2.7 m).

Figure 5.9(a) shows the results for transducer pair 15-14 which has a transmitter-defect "B"-receiver propagation path of 1.14 m; reflections from holes at "B" are therefore expected at 0.21 ms. Again, in this case the reflection from the 5 mm-diameter hole at "B" is not significantly above the highest residual level for the case when the 10 mm-hole was present at "A", making its detection by this transducer pair unreliable. A clear reflection from the 10 mm-diameter hole at "B" is seen however, proving that this defect would again be detectable. Figure 5.9(b) shows

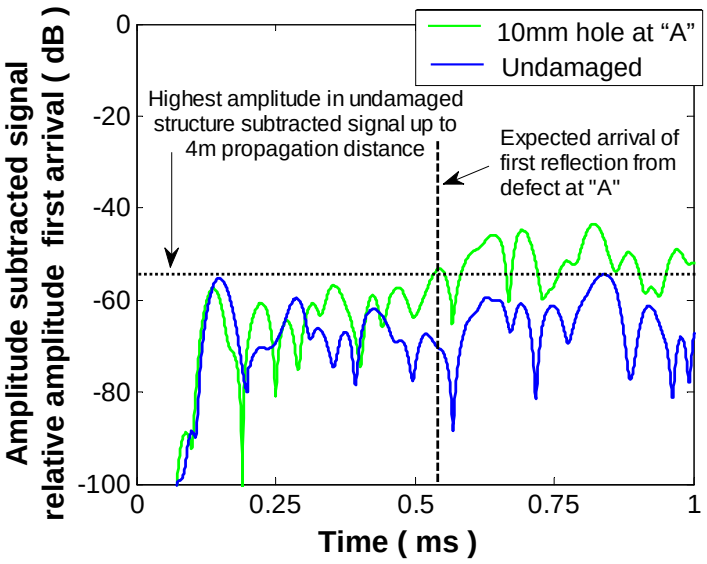

(a)

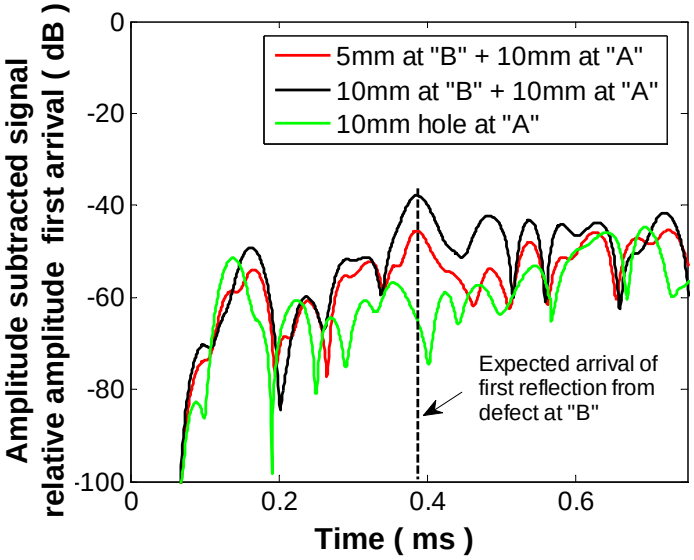

(b)

Figure 5.8: *Amplitude of subtracted signal relative to the amplitude of the first arrival for transducer pair 13-10 when: (a) a 10 mm-diameter hole is present at ”A”; (b) a 10 mm-diameter hole is present at ”A” and a 5 mm- or 10 mm-diameter hole is present at ”B”.*

the results for transducer pair 18-10; here the propagation path from the transducer pair to defect "B" is 2.2 m, and reflections from this position are expected at 0.4 ms. In this case, the 5 mm-diameter hole at "B" can be clearly seen above the highest residual level obtained in the case where a 10 mm-diameter hole was present at "A", and an increase in amplitude at this point is seen when the hole diameter at "B" is increased to 10 mm. The explanation for such a difference in detectability between transducer pairs 13-10 (Figure 5.8(b)) and 18-10 (Figure 5.9(b)) is that although the path of the reflection from the defect to the receiver is the same and is therefore subject to the same drop in amplitude when crossing corrugations, the amplitude of the incident signal is much greater when transducer 18 is used as a transmitter. As can be seen in Figure 5.1(b), the signal emitted from transducer 18 does not interact with any structural features on its way to the defect, whereas the signal arriving at the defect from transducer 13 has crossed 3 corrugations (see Figure 5.1(b)), losing roughly 25-30% of its amplitude at each interaction with the features (see Figure 5.6, the angle of incidence in this case being 15°).

5.4 Imaging Algorithms

Imaging algorithms are a useful way of combining the information obtained by the many transducer pairs in a sparse array, so improving the reliability of the results and providing defect location information. Two algorithms were evaluated in this work, their description being given in the sections below.

5.4.1 Ellipse algorithm

By trigonometry, the time a signal takes to travel from the location of the transmitter, (x_i, y_i), to any point of the panel, (x, y), and to the receiver, (x_j, y_j), is [58, 59]:

$$t_{ij}(x,y) = \frac{\sqrt{(x_i - x)^2 + (y_i - y)^2} + \sqrt{(x_j - x)^2 + (y_j - y)^2}}{V_{gr}} \tag{5.4}$$

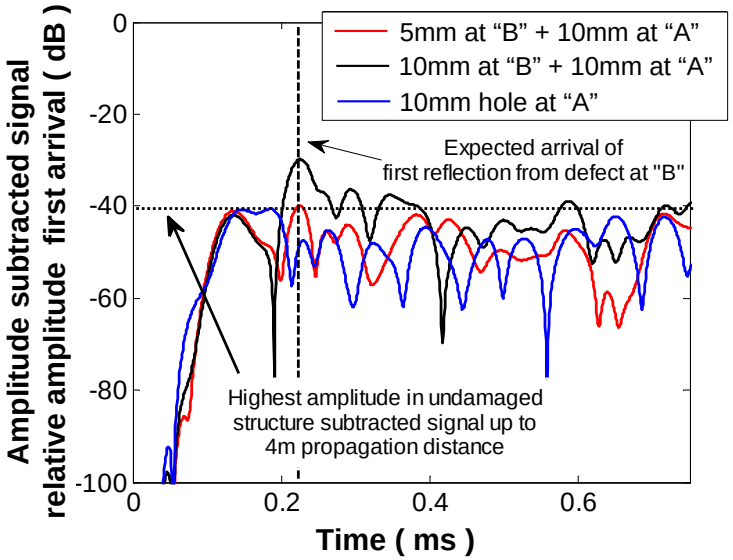

(a)

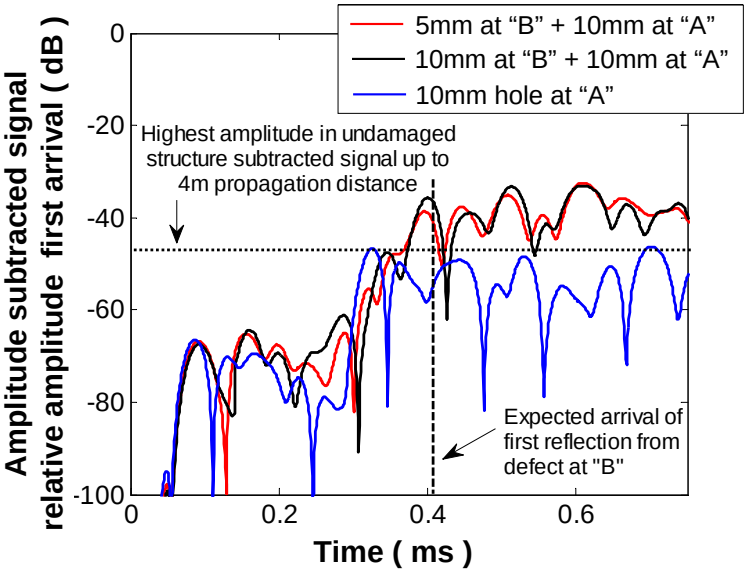

(b)

Figure 5.9: *Amplitude of subtracted signal relative to the amplitude of the first arrival when a 10 mm-diameter hole is present at ”A” and when additional 5 mm- or 10 mm-diameter hole are present at ”B”, for transducer pair: (a) 15-14; (b) 18-10.*

where V_{gr} is the group velocity of the mode of interest at the centre frequency of the input signal. If S_{ij} is the envelope of the subtracted signal for transducer pair ij, obtained after processing of a current signal with the temperature compensation strategy described in Chapter 4, $S_{ij}(t_{ij}(x,y))$ is the amplitude of the subtracted signal corresponding to a given point (x,y) of the panel. By calculating this for every point of the panel, a spatial map of the amplitude of the subtracted signal is obtained. If a reflection is present in the subtracted signal, an ellipse with its foci at the locations of the two transducers will be found; the ellipse is therefore a representation of the most probable locations of the reflection in relation to transducer pair ij. If the procedure above is repeated for a minimum of 3 transducer pair combinations, triangulation is possible and the point at which the 3 ellipses intersect gives the location of the defect. If repeated for all the transducer pair combinations in the array, the final amplitude map will be given by [59]:

$$I(x,y) = \sum_{i=1}^{N-1} \sum_{j=i+1}^{N} S_{ij}(t_{ij}(x,y)) \tag{5.5}$$

where N is the number of sensors in the array.

In this work, the envelope of the signals was used and the amplitude of the signal from a given transducer pair was related to the amplitude of the first arrival between the two transducers, on a dB scale. The images obtained for each transducer pair were then added and the amplitude was averaged.

5.4.2 Hyperbola algorithm

The hyperbola algorithm considers combinations of one transmitter, n, and pairs of receivers, i and j. Therefore, the difference in time that a signal would take to travel from the transmitter to a given point (x,y) on the panel and on to each of the locations of the receivers $((xi,yi)$ and $(xj,yj))$, would be [59]:

$$\Delta t_{ij}(x,y) = \frac{\sqrt{(x_i - x)^2 + (y_i - y)^2} - \sqrt{(x_j - x)^2 + (y_j - y)^2}}{V_{gr}} \tag{5.6}$$

In practise this time difference is calculated using the cross-correlation ($X_{ni,nj}$) between the two subtracted signals obtained after processing of the current signal emitted by n and received by the two receivers i and j. If a reflector is present at the point (x_R, y_R) in the structure, its reflection will appear in the two subtracted signals with different time delays, and the cross-correlation function will give a maximum value at $\Delta t_{ij}(x_R, y_R)$. However, there are many combinations of points (x, y) which will give the same time delay $\Delta t_{ij}(x_R, y_R)$. Therefore, if the value of $X_{ni,nj}$ is plotted for each point (x, y) of the structure, at its corresponding time delay $\Delta t_{ij}(x, y)$, a spatial map will be produced and the shape of the areas with maximum correlation will be a hyperbola with its foci on the two receivers. Again, when this is performed for all the nij groups of sensors available, a full spatial intensity map ($I(x, y)$) will be obtained, and the point at which all the hyperbolae cross will be the location of the defect. The intensity map is therefore given by [59]:

$$I(x,y) = \sum_{n=1}^{N} \sum_{\substack{i=1 \\ i \neq n}}^{N-1} \sum_{\substack{j=i+1 \\ j \neq n}}^{N} S_{ij}(t_{ij}(x,y)) \tag{5.7}$$

The intensity map $I(x, y)$ given by Equation 5.7 was then averaged by the number of combinations to give an averaged correlation map, and plotted on a dB scale. The signals were limited by use of a cosine tapered window with a decay length of 0.1 ms, ending at 1 ms. The main advantage of the hyperbola algorithm is that a larger number of combinations is used in comparison with the ellipse algorithm, which makes identification of the exact location of defects easier [59].

5.4.3 Results

To generate the images shown in this section, the origin of the coordinate system shown in Figure 1b was used and all distances in the panel were corrected for the

additional propagation path imposed by the corrugations, to give a "stretched-out" image. Figure 5.10(a) shows the image obtained when the ellipse algorithm was used to image the whole container panel when no defect was present; the square on the left-hand side of the panel indicates position "A", where holes were later drilled and circles represent the position of the transducers. It can be seen that in the vicinity of the S0 mode transducer array subtraction is very good, residual levels being of the order of -60 dB. Residual signal levels on the left-hand side of the panel become worse due to the influence of distance on subtraction, as described in Chapter 4. When a 10 mm-diameter hole is introduced at position "A" of Figure 5.1(b), the image shown in Figure 5.10(b) is obtained with the ellipse algorithm. Due to the position of the array a limited range of angles of propagation to and from the defect is available. This makes localization of the defect difficult because the ellipses generated cross at very shallow angles, making the precise crossing point difficult to determine accurately. However, the system is able to detect the change caused by the hole since an increase of 7-8dB in the amplitude of the residual is seen over the left-hand side of the panel. Some areas such as the bottom corner of the right-hand side of the panel, showed an increase in levels of up to 3 dB. This is probably because this region is on some of the ellipses showing high values on the left-hand side of the panel and since there are no transducer paths spanning the corner, there is insufficient coverage to reduce the average amplitude to the levels seen within the array.

Since the 10 mm-diameter hole was already present at position "A" when the second hole was drilled at position "B", the level of residual on the right-hand side of the panel in Figure 5.10(b) was the starting point for detection of the second hole. Figure 5.11(a) shows the image obtained from the right-hand side of the panel when a 5 mm-diameter hole is present at position "B". A clear increase in amplitude is seen in the vicinity of the position of the defect, which is indicated by the square in the figure. The shadowing effects discussed earlier are responsible for raising the amplitude values in areas behind the defect, outside the array. When the diameter of the hole is increased to 10 mm, the image in Figure 5.11(b) is obtained; in this case the defect is clearly seen, with an amplitude value which is higher than in all other areas of the figure. The amplitude at the defect is 8dB higher than in the 5

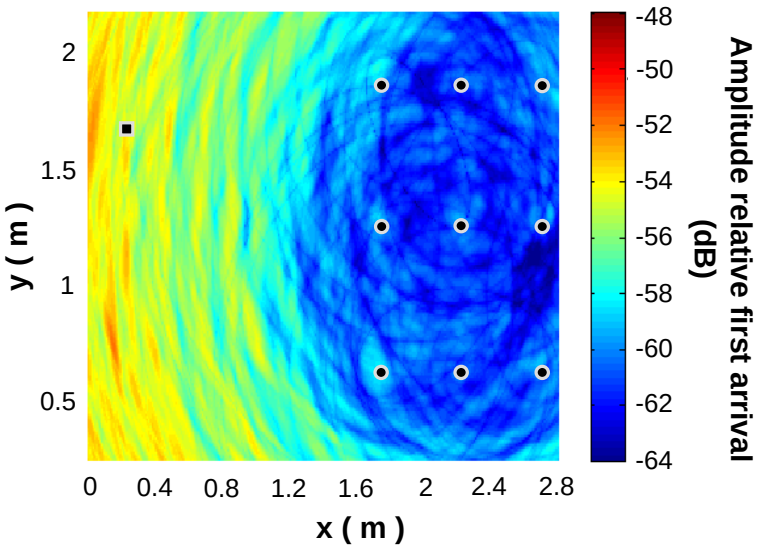

(a)

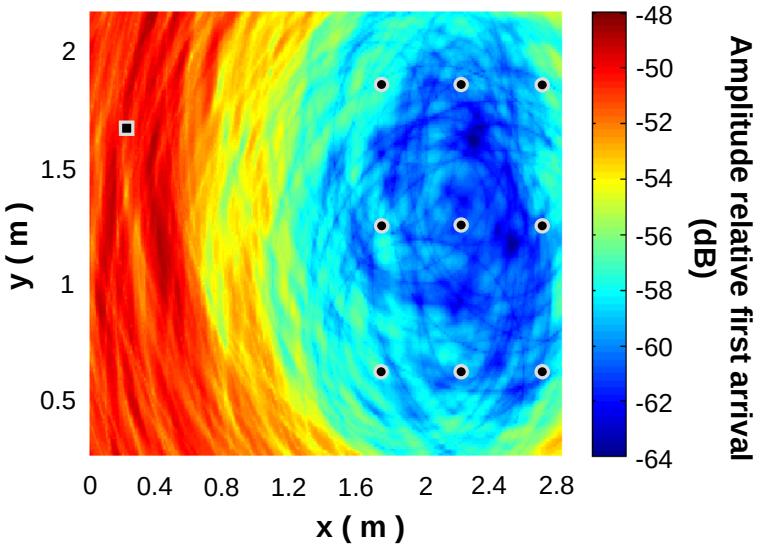

(b)

Figure 5.10: *Image of the full "stretched-out" container panel obtained by processing signals of the S0 mode array with the ellipse algorithm: (a) for the undamaged structure; (b) in the presence of a 10 mm-diameter hole at position "A" in Figure 5.1(b). Dark circles indicate the position of the S0 mode transducers; the dark square indicates position of defect.*

mm-diameter hole case.

When the hyperbola algorithm is applied to signals obtained from the undamaged right-hand side of the panel, the image seen in Figure 5.12 is obtained, and a maximum correlation of around 0.35 is seen in the middle of the area. Figure 5.13(a) shows the image obtained with this algorithm when the 5 mm-diameter hole is present; correlation values of around 0.5 are seen in the area near the defect, which is represented by the square in the figure. When the hole diameter is increased to 10 mm, the algorithm locates the hole more precisely, as shown in Figure 5.13(b). In this image correlation values of 0.7 are seen at the expected position and large changes are seen in the area around the defect.

The ellipse algorithm gives a more exact localisation of the 5 mm-diameter hole, but also produces high noise levels in areas surrounding the sparse array, especially close to the borders of the structure and in the region beyond the defect. This is caused by the shadowing effects mentioned in section 5.3.2, and is of particular concern in cases where the amplitude of the reflection from a defect is low; either the damage will not be identified or these regions will also be "called" as defective. As shown in Figure 5.11(b), this problem is not so significant when a large defect is present, since the amplitude of its reflection is substantially higher than the residual signal in the rest of the structure. The hyperbola algorithm does not locate the defect as precisely (Figure 5.13(b)), but images obtained with this algorithm do not show high levels of signal in areas remote from the defect (Figure 5.13(a)). The explanation for this is that the hyperbola algorithm is based on the correlation between signals recorded by two receivers which will be affected differently by the shadowing caused by the defect, leading to lower values of correlation. This suggests that the best approach may be to combine the results of the two algorithms.

It should be stressed that the transducer pitch in the sparse array is intimately related to the sensitivity of the system. The sensor spacing of the sparse array of S0 mode transducers is sufficient to localise defects with 5 mm-diameter or above within the array, and would have to be replicated in other areas of the structure to ensure full coverage at this sensitivity; in the case of malicious break-in of shipping

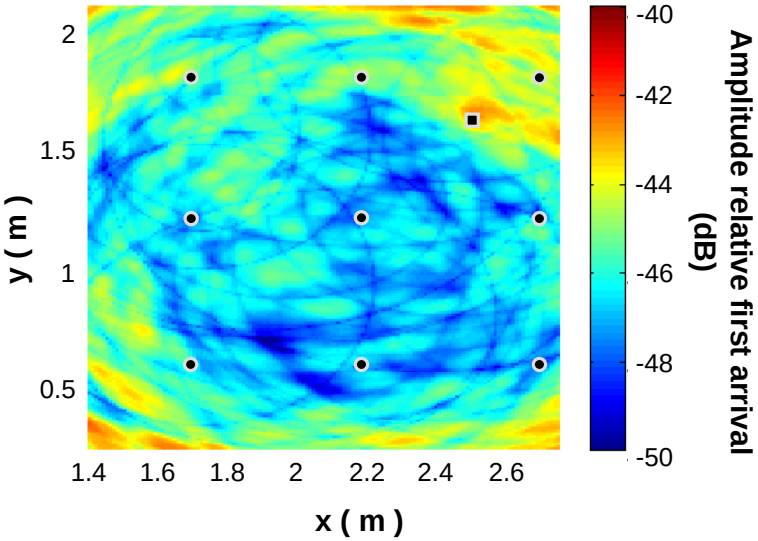

(a)

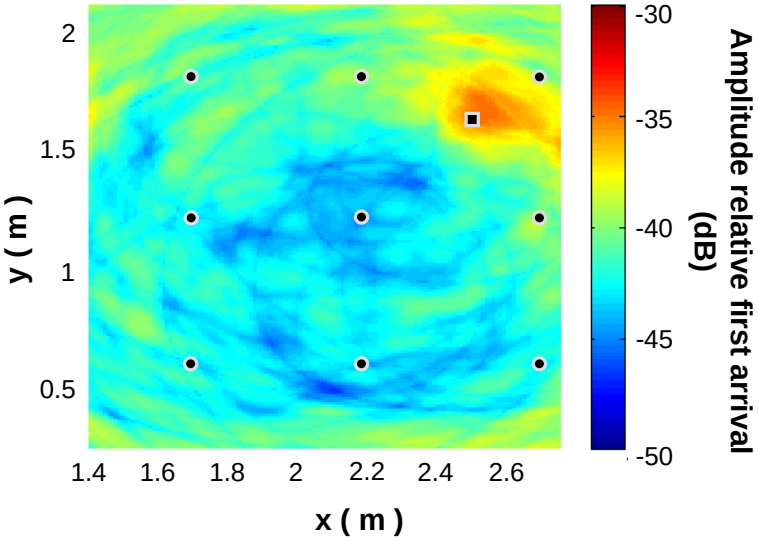

(b)

Figure 5.11: *Image of right hand-side of "stretched-out" container panel obtained by processing signals of the S0 mode array with the ellipse algorithm: (a) in the presence of a 5 mm-diameter hole at position "B" in Figure 5.1(b); (b) in the presence of a 10 mm-diameter hole at position "B" in Figure 5.1(b). Dark circles indicate the position of the S0 mode transducers; the dark square indicates position of defect.*

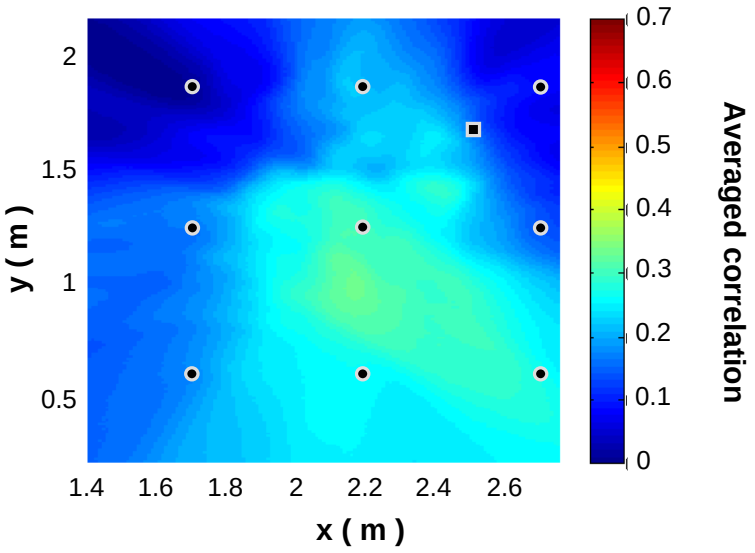

Figure 5.12: *Image of right hand-side of "stretched-out" container panel obtained by processing signals of the S0 mode array with the hyperbola algorithm for the undamaged structure. Dark circles indicate the position of the S0 mode transducers; the dark square indicates position of defect.*

containers, the defects of concern might be substantially larger and a less dense sparse array could probably be used. It is important to note that redundancy is important for defect localisation, and even in the cases where large defects are of concern it may be interesting to have more transducers than strictly necessary in order to improve reliability.

5.5 Summary

A combination of the Optimal Baseline Subtraction and the Optimal Stretch methods was shown to be a robust means of compensating for temperature variations in a real complex metallic structure in a non-laboratory environment subject to temperature fluctuations of up to 8°C and temperature gradients of 2°C within the structure.

It was shown that the S0 mode propagated better across the corrugations in the

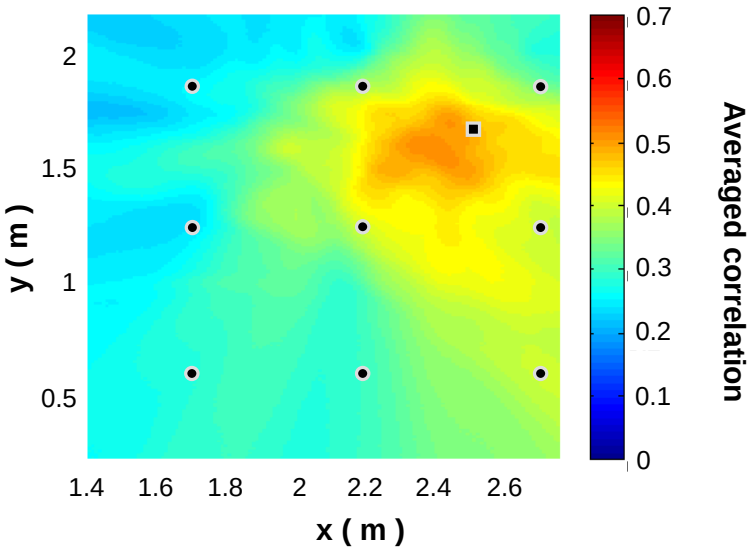

(a)

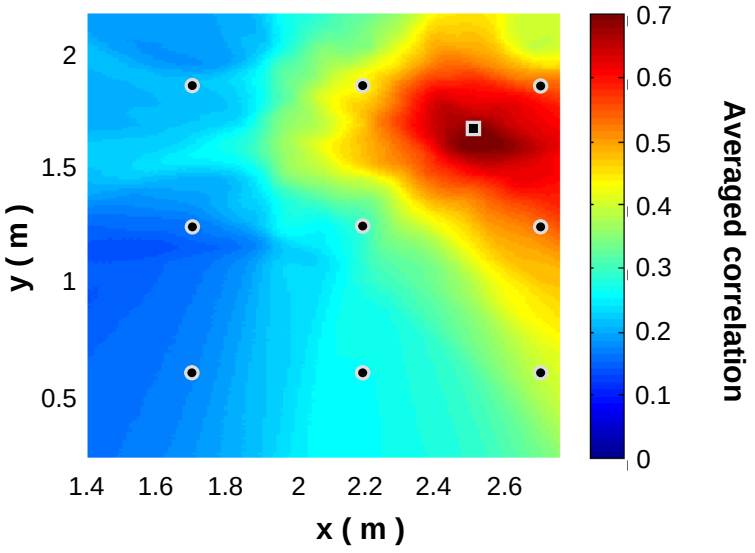

(b)

Figure 5.13: *Image of right hand-side of "stretched-out" container panel obtained by processing signals of the S0 mode array with the hyperbola algorithm: (a) in the presence of a 5 mm-diameter hole at position "B" in Figure 5.1(b); (b) in the presence of a 10 mm-diameter hole at position "B" in Figure 5.1(b). Dark circles indicate the position of the S0 mode transducers; the dark square indicates position of defect.*

structure over a range of angles than the A0 mode so this mode was more suitable for sparse array guided wave SHM in this structure. It is thought that for each structure of interest such a study will be needed since different modes will have better or worse propagation depending on the feature encoutered in that structure. 5 mm and 10 mm diameter holes were successfully detected and located within the region covered by a 9 element array on a rectangular 0.76 x 1.22 m grid. Both ellipse and hyperbola location schemes were used successfully and it was concluded that combining the images resulting from use each method would be useful in practice. A 10 mm hole could reliably be detected at a transmitter-defect-receiver distance exceeding 2 m confirming the practical applicability of guided wave systems of this type.

Chapter 6

Conclusions

6.1 Thesis review

In this thesis the use of guided wave SHM to monitor complex 2D structures was investigated. Guided wave SHM takes advantage of the fact that low frequency Lamb waves can propagate long distances, across many structural features. This makes the technique comparable to acoustic emission SHM, although it shows several advantages including an improved control over the Lamb wave modes propagating in the structure, which leads to a more precise signal processing, the possibility of repeating the inspection to verify results, the elimination of transient and incoherent noise, and low energy consumption during operation.

Signals obtained with guided waves in a structure with high feature density are complicated because of the large number of overlapping reflections, which are a source of coherent noise that needs to be eliminated or reduced if defects are to be detected. This makes signal processing a key requirement if a successful system is to be developed. Review of work in literature shows that most authors rely on the use of baselines: benchmark signals taken from the structure which are compared or subtracted from signals taken during later inspections, with the objective of detecting or monitoring the appearance or growth of defects. However, effects such as temperature, liquid loading and stress cause changes to the signals and signal

processing methods are needed to compensate for these effects. Baseline subtraction methods also require excellent transducer stability, and mode purity is known to reduce signal complexity, in this way helping to eliminate some of the coherent noise even before signal processing is applied.

In this thesis the problem of guided wave SHM was tackled both on the transduction and on the signal processing fronts. A transducer generating high mode purity A0 was developed and a transducer generating substantially pure S0 mode had its behaviour investigated. Both transducers were carefully evaluated in order to ensure they had phase stability when faced with temperature variations. Two temperature compensation techniques, the Optimal Baseline Subtraction and the Optimal Stretch, were evaluated experimentally and the influence of signal complexity and mode purity on these was established. This led to the proposal of a compensation strategy which identifies the advantages of each of the techniques to be complementary; therefore the use of both in combination eliminates some of their disadvantages.

The transducers described in Chapter 3 and the compensation strategy proposed in Chapter 4 were tested in Chapter 5 on a large and complex metallic structure in an uncontrolled environment as a demonstration system, and good detection and localisation of 10 mm-diameter holes was obtained.

6.2 Main findings of this thesis

6.2.1 Transduction

A temperature-stable transducer generating the A0 mode at low frequencies with high mode purity was developed. This was achieved by modifying the frequency-response of a piezoelectric disc by means of a backing mass and a soft front layer. The backing mass was effective in reducing the through-thickness resonance of the piezoelectric disc from 1MHz to around 100kHz. Since the frequency region of interest

was much lower, from 20-40kHz, and since increasing the backing mass length became ineffective in further lowering the resonance, a soft front layer was introduced. This proved to be effective in lowering the resonance frequency of the system to the 20kHz region or below, depending on its thickness. It also reduced significantly the transmission of in-plane force to the plate which occurs during resonance of the disc, and therefore improved mode purity significantly. Because the front layer has much lower stiffness than the other components of the transducer, if the backing mass and the PZT element are considered as a point-mass and the transducer is on a stiff base (e.g. a thick enough plate), the transducer-plate combination can be modelled as a simple spring-mass system. The final vertical dimensions of the transducer based on a 2 mm-thick PZT element were a 6 mm-long backing mass and a 2 mm-thick SiC foam interlayer.

The transducer diameter influences the amplitude transmitted to the plate, the mode purity of signals generated in the plate, and the behaviour of the transducer-plate combination as a spring-mass system, and a compromise between these effects must be found. Because the three effects are controlled by the parameter D/λ_{A0} which relates transducer diameter to A0 mode wavelength, the optimal diameter was found to be a function of plate thickness, varying from 5 mm at plate thicknesses up to 5 mm, to 25 mm at plate thicknesses from 25 mm to 30 mm.

The temperature stability of the transducer was evaluated and it was found that above resonance excitation gave excellent phase stability without significant loss of transmitted A0 mode amplitude or lowering of the A0/S0 mode ratio. Experimental results showed that A0/S0 mode power flow ratios over 40dB were obtained on 3 mm-thick aluminium plates and FE results suggest values above 35dB can be obtained on any plate thickness.

A 20 mm-diameter, 1 mm-thick piezoelectric disc was studied in order to generate S0 mode. This transducer takes advantage of a lowering in transmission of the A0 mode in the frequency region close to where the diameter of the disc is equal to the A0 mode wavelength. FE results showed that a S0/A0 mode voltage ratio of 17dB could be obtained at 150kHz in pitch-catch on a 5 mm-thick aluminium plate, and

experimental measurement showed that a S0/A0 mode power flow ratio of 21dB was obtained on a plate of the same thickness. If the same transducer is excited at 200kHz this ratio drops to 8dB. Experimental measurements of temperature stability showed that this transducer shows only small phase shifts in the frequency region from 120-240kHz, the only significant changes in the FRF being amplitude shifts which can easily be compensated for.

6.2.2 Signal processing and temperature compensation

The Optimal Baseline Subtraction method was evaluated experimentally, and it was shown that if this method is used alone, a large database, with a temperature gap close to 0.1°C in between baselines, is needed to obtain amplitude levels in the subtracted signal close to -40dB relative to the first arrival (which would allow detection of 1% reflections). The Optimal Stretch method when used alone is highly dependent on signal complexity and mode purity; on a simple structure with high mode purity it can compensate for a 5°C temperature difference in between a baseline and a current signal.

A temperature compensation strategy, consisting of the combination of the Optimal Baseline Subtraction and the Optimal Stretch methods, is proposed. This reduces the number of baselines necessary to ensure good sensitivity in comparison to that needed when the Optimal Baseline Subtraction technique is used alone. The reduction in the number of baselines in the database is limited by the maximum temperature gap between baselines which can be compensated for by the Optimal Stretch without loss of sensitivity; this is a function of mode purity, signal complexity and the maximum propagation distance required to cover the whole structure expressed in wavelengths. In some cases, especially when the signal complexity is high or when mode purity is insufficient, the temperature gap between baselines needed for good sensitivity can drop to as low as 0.5°C, as was seen for the airframe structure inspected. In this case, the signal processing strategy gave a residual of -38dB with a temperature gap of 0.5°C, when high mode purity was used. If the temperature gap was increased to 1°C the residual amplitude was worsened, to -34dB.

When this signal processing strategy was used to process signals obtained from undamaged plates and from the same plates with simulated damage, a first excursion above the residual level for the undamaged structure was seen at the expected position of the first reflection from the "defect". Large increases in later parts of the residual signals were also seen, indicating good sensitivity to changes in the structure. Defects as small as 2.5 mm were detected in a complex airframe structure, thus validating the efficiency of the signal processing strategy described in this chapter in inspecting a real structure.

6.2.3 Inspection of a real structure

A combination of the Optimal Baseline Subtraction and the Optimal Stretch methods was shown to be a robust means of compensating for temperature variations in a real complex metallic structure, a container door made of 2 mm-thick corrugated steel, in a non-laboratory environment subject to temperature fluctuations of up to 8°C and temperature gradients of 2°C within the structure.

Finite elements models were used to obtain angular-dependent reflection and transmission coefficients for the A0 and S0 mode when propagating across the main structural feature of the structure. It was shown that the S0 mode propagated better across the corrugations in the structure over a range of angles than the A0 mode so this mode was more suitable for sparse array guided wave SHM. 5 mm and 10 mm diameter holes were successfully detected and located within the region covered by a 9 element array on a rectangular 0.76 x 1.22 m grid. Both ellipse and hyperbola location schemes were used successfully and it was concluded that combining the results of the two methods would be useful in practice. A 10 mm hole could reliably be detected at a transmitter-defect- receiver distance exceeding 2 m confirming the practical applicability of guided wave systems of this type.

6.3 Suggestions of future work

For a SHM system to be commercially viable, transducers will have to be very reliable and robust and have excellent long-term stability. This is crucial in a system such as the one proposed in this thesis since baselines will have to remain valid for periods of years. Therefore, a considerable amount of work is needed on transducer attachment techniques and shock and wear resistant casings for the transducers proposed in Chapter 3. New transducers might have to be developed altogether. Transducers attached to the structure would also need to be calibrated if defect dimensions are to be adequately estimated.

To gain confidence and to test the reliability and robustness of the temperature compensation and imaging signal processing methods described in this thesis, it is important to apply the technique to a wider variety of structures, possibly in real operating conditions. It is important to investigate the possibility of monitoring structures where temperature is not the only factor affecting wave velocity, and where it might be necessary to integrate the SHM system with measurements of load (in most cases) or liquid level and viscosity (in the case of a storage tank), to ensure the test is performed always under the same conditions. An algorithm such as suggested in [55] would allow the system to avoid inspection when large temperature gradients are present.

Further work would also involve an algorithm which incorporates the sparse-array design method proposed in [9] with finite element-obtained incidence angle-dependent reflection coefficients from the main structural feature of the structure to be monitored. This algorithm would then calculate the optimal number and positioning of sensors in a specific structure in order to detect a given defect. Each structure would therefore need to have a specific sparse-array designed for its monitoring.

In mass produced structures where the same monitoring system design would be repeated many times, it could be worth investing time in creating a database of images obtained when a variety of common defects are present, which would be aimed at helping with precise defect characterisation.

The same techniques used in this thesis for monitoring of 2D complex structure could be applied to monitoring of pipes with permanently installed transducer rings, especially in regions of the pipe which have a high reflector density such as T-joints, welded supports, etc.

Appendix A

Material properties of piezoelectric ceramic Pz27

$\epsilon_{11}^S \setminus \epsilon_0$	1129.4
$\epsilon_{33}^S \setminus \epsilon_0$	914.8
$c_{11}^E(10^{10}N/m^2)$	14.7
c_{33}^E	11.3
c_{12}^E	10.5
c_{13}^E	9.37
c_{44}^E	2.12
c_{66}^E	2.3
$e_{11}(C/m^2)$	-3.09
e_{33}	16
e_{15}	11.64
$\rho(10^3Kg/m^3)$	7.7
ϵ_0 (dielectric constant of free space - $C.V^{-1}.m^{-1}$)	$8.854e-12$

Appendix B

Detailed experimental procedures

This appendix will describe the equipment, detailed data acquisition parameters and the steps taken during processing of the data acquired in the experiments of Chapters 3,4 and 5. Initially, two different sets of equipment which were used to record all the results presented throughout this thesis will be described; depending on the experiment, these were used in combination with different amplifiers and transducers or sensors, which will be described separately. Also, for each experiment, slightly different data acquisition parameters and signal processing routines were used, and these will be presented associated with the chapter and section in which the final results are shown in the thesis.

B.1 Data recording equipment

Equipment 1

This was the equipment used to obtain results in Chapter 3 and 4. It consisted of a National Instruments (E-series board with NI BNC 2110 interface) computer-based oscilloscope with 12-bit data acquisition resolution capability, which was controlled always by the same Labview routine, which ensured that the full resolution was always used independent of the read voltage peak-to-peak amplitude. The sam-

pling frequency was always 10 MHz and the number of points was adjusted in each experiment to obtain the required signal length. Averaging was used to eliminate incoherent noise, which was not measured since it was satisfactorily low in all cases, and a usual number of averages was 100.

Equipment 2

This was the equipment used to obtain results in Chapter 5. It consisted of a Waverunner 6030 LeCroy oscilloscope, with 8-bit resolution. Signals were recorded through a Labview routine running on a computer connected to the oscilloscope. The computer was also connected to a multiplexer and the Labview routine was used to control its channel selection. The system did not allow the operator to adjust the dynamic range of the oscilloscope for each time-trace obtained from an array of transducers. This meant that the full resolution of the oscilloscope was set to the time-trace of the transducer pair with the highest peak-to-peak amplitude. In this equipment the number of points was fixed at 50000 points and different signals lengths were used in each experiment, giving different sampling frequencies. All signals were averaged 100 times, and incoherent noise was not measured since it was satisfactorily low in all cases.

B.2 Results in Chapter 3

Results in Section 3.2.4

Transducers with 5 and 10 mm diameter, 6 mm long backing mass, 2 mm thick PZT and 2 mm thick SiC interlayer were excited with a 5-cycle Hanning-windowed toneburst which was centered at frequencies between 10 kHz and 100 kHz, with 1kHz steps. These were uploaded from a PC to an arbitrary function generator (Agilent 33220) and driven through a power amplifier (Krohn-Hite 7602) which gave 55V peak-to-peak signal. A laser vibrometer (Polytec) measuring out-of-plane velocity was focused at 5 mm from the transducer (see Figure 3.15) and Equipment 1 was

used to record velocity time-traces. The peak amplitude of the signal obtained at each excitation frequency was then used to plot the velocity FRF; the displacement FRF in Figures 3.16 and 3.17 was obtained by dividing each of the points of the velocity FRF by its corresponding frequency value.

Results in Section 3.2.5

Results in Figures 3.18 and 3.19 were obtained by exciting a 5 mm-diameter transducer, with a 6 mm long backing mass, 2 mm thick PZT and 2 mm thick SiC interlayer, attached to a 5 mm-thick aluminium plate, with 5-cycle Hanning windowed tonebursts with centre frequencies of 20, 30 and 50 kHz, while varying the temperature of the system with a hotplate as described in section 3.2.5. These signals were uploaded from a PC to an arbitrary function generator (Agilent 33220) and driven through a power amplifier (Krohn-Hite 7602) which gave 55V peak-to-peak signal. Equipment 1 was used to acquire velocity time-traces from a laser interferometer (Polytec) measuring the out-of-plane velocity on the backing mass of the transducer. The FFT of the velocity time-trace at each excitation frequency was divided by the corresponding input signal and the magnitude and phase of the FRF obtained for each excitation frequency were combined and plotted for each temperature value.

Results in Section 3.2.6

A 5 mm-diameter transducer, with a 6 mm long backing mass, 2 mm thick PZT and 2 mm thick SiC interlayer, was attached to a 3 mm-thick aluminium plate. A 5-cycle Hanning windowed toneburst centered at 35 kHz was uploaded from a PC to an arbitrary function generator (Agilent 33220) and driven through a power amplifier (Krohn-Hite 7602) which gave a 55V peak-to-peak signal. Two different laser interferometer systems (Polytec) were used to obtain signals at 40 cm from the transducers, one consisting of a single laser head measuring out-of-plane velocity, and one of two laser heads whose combined signal gave in-plane velocity. Equipment 1 was used to acquire all velocity time-traces. The velocity time-traces of Figures 3.21

and 3.22 were processed to obtain mode ratios. Cosine tapered windows were used to isolate the first arrivals of the A0 and S0 modes. The FFT of the windowed time-traces was obtained and the maximum magnitude of the spectra, which occurred at 35 kHz, was divided by this frequency to obtain displacement values. Power flow normalised displacement values from DISPERSE [2] were used to obtain the A0/S0 mode power flow ratios described in section 3.2.6.

Results in Section 3.3.2

In Figure 3.25, signals from the S0 mode transducer were recorded with Equipment 1 combined with a laser interferometer (Polytec) measuring out-of-plane velocity at 30 cm from the transducer when it was attached to a 5 mm-thick aluminium plate. A 5-cycle Hanning windowed toneburst centered at 150 or 200 kHz was uploaded from a PC to an arbitrary function generator (Agilent 33220) and driven through a power amplifier (Krohn-Hite 7602) which gave a 20V peak-to-peak signal. Again, to obtain mode ratios from these figures, cosine tapered windows were used to isolate the first arrivals of the A0 and S0 modes. The FFT of the windowed time-traces was obtained and the magnitude values of the spectra at 150 and 200 kHz were divided by these frequencies to obtain displacement values. Power flow normalised displacement values from DISPERSE [2] were used to obtain the S0/A0 mode power flow ratios described in section 3.3.2.

Figures 3.26 and 3.27 were obtained by processing the signals obtained with a laser interferometer measuring out-of-plane displacement on the back of the S0 mode transducer using the same setup described in section B.2, although in this case only one input signal was used, a 3-cycle Hanning windowed toneburst at 170 kHz.

B.3 Results in Chapter 4

Experiments on simple plates

The two systems shown in Figure 4.7 (large and small plate) were placed in a temperature controlled environment where the temperature was gradually increased by 10°C and then cooled back to ambient temperature, signals being acquired at 0.1°C steps. This cycle was repeated with an interval of a day and signals obtained during the first cycle were used as baselines while signals from the second cycle were considered current signals. The temperature was monitored by type-K thermocouples soldered to the plate next to the transducers. Temperature was read to a precision of 0.1°C.

Equipment 1 was used to record signals from transducer pairs in the large and small plates described in section 4.4.1. A PC was used to upload input signals to an arbitrary function generator (Agilent 33220) which was connected through an amplifier (Krohn-Hite 7602) to the emitting transducer, driving the A0 mode transducer at 55V and the S0 mode transducer at 20V peak-to-peak. The signal from the receiver was pre-amplified (Krohn-Hite 3988).

In all results, the coherent noise remaining after baseline subtraction was measured and displayed in the following format: the envelope of the residual signal obtained after baseline subtraction, in the form of the absolute value of the Hilbert transform of the signal, was shown on a dB scale relative to the amplitude of the envelope of the first arrival between the two transducers in pitch-catch.

All results were also compensated for beam spreading according to Equation 4.9.

Signal processing in Section 4.4.3

In this section only the Optimal Baseline Subtraction method was applied. The controlling parameter for the technique was the rms of the residual signal. The full database was used initially, and then a subset of baseline with a temperature gap of

0.3°C in between baselines was chosen.

Signal processing in Section 4.4.4

In this section only the Optimal Stretch method was applied, following the methodology described in section 4.3.2, with the rms of the subtracted signal in the time domain being the controlling parameter, and the bandpass filter described in section 4.3.3 was also used. As the input signal was a 5-cycle Hanning windowed toneburst at the chosen centre frequency, the bandpass filter used was a 7-cycle Hanning windowed toneburst centred at the same frequency. As shown in section 4.4.2, initially a 5°C temperature difference in between the reference signal and the current signal was tested both for the large and the small plate signals. This temperature difference was then reduced to 2°C and 1°C for signals from the small plate.

Signal processing in Section 4.4.6

This section aims to evaluate the efficiency of the combination of the Optimal Baseline Subtraction and the Optimal Stretch methods in detecting a simulated defect in the plate in the form of a cylindrical 5mm-diameter, 6mm-long brass mass attached to the surface of the plate with gel couplant.

Both for the large and the small plate cases, initially the Optimal Baseline Subtraction method was applied to a signal taken from the "damaged" and the undamaged structure, and a subset of baselines with a temperature gap of 0.5°C was used. The controlling parameter was the rms of the subtracted signal. When the Optimal Baseline had been selected, the Optimal Stretch was applied; for this the frequency content of the signal from the "damaged" or undamaged structure was expanded to match the baseline as described in section 4.3.2, the controlling parameter being the rms of the residual signal in time, and the bandpass filter described in section 4.3.3 was also used. The subtracted signals obtained after processing for the undamaged and "damaged" case were compared in the figures of this section.

Signal processing in Section 4.6.1

The panel was instrumented with 3 low-frequency A0 mode transducers as shown in Figure 4.23; in the results shown in this section transducer 3 was used as an emitter and transducers 2 and 1 as receivers. The system was placed in a room with no temperature control where temperature variations of up to 4-5°C were common. The acquisition system consisted essentially of the same equipment used for previous experiments, the only difference being the use of a multiplexer to switch between receiving channels. Signals were acquired every 2 hours over 3 weeks and this supplied a set of baselines in which temperature gaps between signals never exceeded 0.3°C.

Signals from the undamaged structure were then processed with the Optimal Baseline Subtraction only, with the full database being used. These results were compared to the ones obtained when the combined Optimal Baseline Subtraction and Optimal Stretch methods were applied, with a subset of baselines which had a temperature gap of 0.5°C. The sequence of steps was the same as described above for section 4.4.6.

Signal processing in Section 4.6.2

The signals taken from the damaged panel were also processed with the combination of the Optimal Baseline Subtraction and Optimal Stretch methods and the same subset of baselines, with a temperature gap of 0.5°C, was used, as in section 4.4.6. The residual signal for the undamaged panel was compared to the residual signals obtained when holes of 1,2.5 and 5mm-diameter were present in the panel.

B.4 Results in Chapter 5

The container panel was placed in the goods inwards area of the building close to a large roller door and was subjected to uncontrolled temperature swings. The

temperature was monitored at each transducer by type-K thermocouples measuring relative temperature variations to a precision of 0.1°C; during the 9 week period in which the experiment was performed, ambient temperature differences of 8°C were measured. Temperature gradients of up to 2°C between sensors were commonly seen; at night, when the temperature of the storage room was relatively constant due to the large access door to the storage room being closed, gradients were smaller than 0.2°C. This suggests that the gradients of around 2°C seen at other times are genuine, and not solely due to thermocouple calibration errors.

A PC was used to upload input signals to an arbitrary function generator (Agilent 33220) which was connected through an amplifier (Krohn-Hite 7602) to a custom built multiplexer. Received signals were pre-amplified (Krohn-Hite 3988) before returning to the multiplexer. A Labview routine was used to control the emitter-receiver channel selection of the multiplexer, and to save the signals displayed on an oscilloscope (LeCroy 9310A) set to 100 averages.

Only pitch-catch measurements were performed with the transducers of the S0 mode array shown in Figures 5.1(a) and 5.1(b); because of the symmetry of the transmitter-receiver matrix, only half of the combinations were acquired, leading to 36 measurements for each test. The total time necessary for collection of all signals was around 15 minutes. One set of baselines was acquired for all transmit-receive combinations; this was done over 3 weeks at 2-hour intervals and this procedure guaranteed a comprehensive database, with no temperature gaps larger than 0.3°C in between baselines. One week later, a set of 10 signals from the undamaged structure was taken, before a defect in the form of a drilled hole was introduced to the panel at point "A" in Figure 5.1(b). The initial diameter of the hole was 1 mm; this was later increased to 2.5, 5 and 10 mm. For each hole drilled, 10 signals were acquired for all transmitter-receiver combinations, over a period of one day. After these measurements were performed, the system was left idle for 4 weeks; in the fifth week the same drilling procedure was applied to point "B" in Figure 5.1(b), 10 signals again being acquired over a period of one day for each hole size.

The signals were processed with the combined Optimal Baseline Subtraction and

Optimal Stretch methods and the full database of baselines was used. The procedure was the same as was used in section 4.4.6. All subtracted signals were compensated for beam spreading with Equation 4.9. After this the imaging algorithms described in section 5.4 was applied to the signals.

References

[1] *Nondestructive testing handbook, 2nd edition*, volume 5. American Society for Nondestructive Testing, USA, 1987.

[2] M. J. S. Lowe. Matrix techniques for modeling ultrasonic waves in multilayered media. *IEEE Trans. Ultrason. Ferroelectr. Freq. Control*, 42(4):525–542, 1995.

[3] T. Clarke, F. Simonetti, S. Rokhlin, and P. Cawley. Evaluation of the temperature stability of a low frequency a_0 mode transducer developed for shm applications. In D. O. Thompson and D. E. Chimenti, editors, *Review of Progress in Quantitative NDE*, volume 27A, pages 910–917. American Institute of Physics, 2008.

[4] D. N. Alleyne, B. Pavlakovic, M. J. S. Lowe, and P. Cawley. Rapid, long range inspection of chemical plant pipework using guided waves. *Insight*, 43:93–96,101, 2001.

[5] Z. Sun, L. Zhang, and J.L. Rose. Flexural torsional guided wave mechanics and focusing in pipe. *Journal of Pressure Vessel Technology*, 127:471–478, 2005.

[6] P.D. Wilcox, M. Evans, B. Pavlakovic, D. N. Alleyne, K. Vine, P. Cawley, and M. J. S. Lowe. Guided wave testing of rail. *Insight*, 45(6):413–420, 2003.

[7] P. Cawley, M. J. S Lowe, D. N Alleyne, B. Pavlakovic, and P. Wilcox. Practical long range guided wave testing: application to pipes and rail. *Materials Evaluation*, 61(1):66–74, 2003.

[8] S. K. Arora and A. M. Manekar. Precise determination of epicenters and origin times of surface focus seismic events. *Bulletin of the Seismological Society of America*, 59(2):777–788, 1969.

[9] A. J. Croxford, P. D. Wilcox, B. W. Drinkwater, and G. Konstantinidis. Strategies for guided-wave structural health monitoring. *Proc. Royal Society A*, 463:2961–2981, 2007.

[10] P. Rye, A. Starr, K. Schaff, and S. Nemat-Nasser. Integration of eletronic sensing in composite materials for structural health monitoring. In *Proc. of the 5th International Workshop on Structural Health Monitoring*, page 756. Stanford University, 2005.

[11] P. Capoluongo, C. Ambrosino, S. Campopiano, A. Cutolo, M. Giordano, I. Bovio, I. L. Lecce, and A. Cusano. Modal analysis and damage detection by fiber bragg grating sensors. *Sensors and Actuators A: Physical*, 133(2):415–424, 2007.

[12] C. P. Frizten. Recent developments in vibration-based structural health monitoring. In *Proc. of the 5th International Workshop on Structural Health Monitoring*, page 42. Stanford University, 2005.

[13] B. Fernandes, P. Gaydecki, and F. Burdekin. An intelligent sensor system for monitoring fatigue damage in welded steel components. In D. O. Thompson and D. E. Chimenti, editors, *Review of Progress in Quantitative NDE*, volume 24B, pages 1817–1825. American Institute of Physics, 2004.

[14] J. H. Shih and J. K. Mal. Acoustic emission from impact damage in cross-ply composites. In *Proc. of the 2th International Workshop on Structural Health Monitoring*, page 209. Stanford University, 1999.

[15] M. Malkin. Structural health monitoring for bonded repairs: Complex structure testing. In *Proc. of the 5th International Workshop on Structural Health Monitoring*, page 470. Stanford University, 2005.

[16] K. F. Voss and K. H. Wanser. Fiber sensors for monitoring structural strain and cracks. In A. McDonach and P. T. Gardiner, editors, *Proc. 2nd European Conference on Smart Structures and Materials*, pages 144–147. SPIE, 1994.

[17] C. K Lee, J. J. Scholey, P. D. Wilcox, M. R. Wisnom, Friswell M. I., and B. W. Drinkwater. Guided wave acoustic emission from fatigue crack growth in aluminium plate. *Advanced Materials Research*, 13-14:23–28, 2006.

[18] C. R. Farrar and S. W. Doebling. An overview of modal-based damage identification methods. In *Proc. of DAMAS Conference, Sheffield, UK*, 1997.

[19] B. Yang, A. K. Suh, and A. K. Chan. Characterization and detection of crack-induced rotary instability. *Trans. of the ASME*, 124:40–48, 2002.

[20] Scott W. Doebling, Charles R. Farrar, and Michael B. Prime. A summary review of vibration-based damage identification methods. *Identification Methods, The Shock and Vibration Digest*, 30:91–105, 1998.

[21] P. Cawley. The detection of delaminations using flexural waves. *NDT&E International*, 23:207 – 213, 1990.

[22] X. P. Qing, H. L. Chen, S. J. Beard, and A. Kumar. An active diagnostic system for structural health monitoring of rocket engines. *J. of Intelligent Material Systems and Strucutres*, 17:619–628, 2006.

[23] A. V. Baukulin, S. N. Isaev, and A. P. Tishkin. Acoustic-emission location of corrosion centers. *NDT&E International*, 27(4):217, 1994.

[24] J. M. Carlyle. Acoustic emission testing the f111. *NDT&E International*, 22(2):67–73, 1989.

[25] J. H. Odell. Monitored proof testing: a method of insuring structural integrity. *Air Clues*, 13-14:416, 1991.

[26] R. P. Dalton, P. Cawley, and M. J. S. Lowe. Propagation of acoustic emission signals in metallic fuselage structure. *IEEE Proc. Sci. Meas. Technol.*, 148(4):169, 2001.

[27] W. J. Staszewski and Holford. K. M. Wavelet signal processing of acoustic emission data. *Key engineering materials*, 204-205:351–358, 2001.

[28] M. R. Gorman. Plate waves acoustic emission. *J. Acoust. Soc. Am.*, 90(1):358, 1991.

[29] B. N. Pavlakovic, M. J. S. Lowe, D. N. Alleyne, and P. Cawley. Disperse: A general purpose program for creating dispersion curves. In D. O. Thompson and D. E. Chimenti, editors, *Review of Progress in Quantitative NDE*, volume 16, pages 185–192. Plenum Press, New York, 1997.

[30] P.D. Wilcox. A signal processing technique to remove the effect of dispersion from guided wave signals. *IEEE Trans. Ultrason. Ferroelectr. Freq. Control*, 50(4):419–427, 2003.

[31] D. N. Alleyne and P. Cawley. Optimization of lamb wave inspection techniques. *NDT&E International*, 25(1):11–22, 1992.

[32] R. S. C. Monkhouse, P. D. Wilcox, and P. Cawley. Flexible interdigital pvdf transducers for the generation of lamb waves in structures. *Ultrasonics*, 35(1):489–498, 1997.

[33] P. D. Wilcox, M. J. S. Lowe, and P. Cawley. The excitation and detection of lamb waves with planar coil electromagnetic acoustic transducers. *IEEE Trans. Ultrason. Ferroelectr. Freq. Control*, 52(12):2371–2383, 2005.

[34] P.D. Wilcox, M. J. S. Lowe, and P. Cawley. An emat array for the rapid inspection of large structures using guided waves. In D. O. Thompson and D. E. Chimenti, editors, *Review of Progress in Quantitative NDE*, volume 22A, pages 814–821. Plenum Press, New York, 2003.

[35] P. Fromme, P. Wilcox, M. J. S. Lowe, and P. Cawley. On the development and testing of a guided ultrasonic wave array for structural health monitoring. *IEEE Trans. Ultrason. Ferroelectr. Freq. Control*, 53(4):777–785, 2006.

[36] H. Gao, M. J. Guers, J. L. Rose, G. Zhao, and C. Kwan. Ultrasonic guided wave annular array transducers for structural health monitoring. In D. O.

Thompson and D. E. Chimenti, editors, *Review of Progress in Quantitative NDE*, volume 25, page 16801. Plenum Press, New York, 2006.

[37] M. Lin, X. Qing, A. Kumar, and S. J. Beard. Smart layer and smart suitcase for structural health monitoring applications. In D. O. Thompson and D. E. Chimenti, editors, *Proc. SPIE on Smart Structures and Materials*, volume 4332. SPIE Optical Engineering Press, 2001.

[38] J. E. Michaels. Detection, localization and characterization of damage in plates with an *in situ* array of spatially distributed ultrasonic sensors. *Smart Materials and Structures*, 17(3):035035 (15pp), 2008.

[39] X. Zhao, H. Gao, G. Zhang, B. Ayhan, F. Yan, C. Kwan, and J. L. Rose. Active health monitoring of an aircraft wing with embedded piezoelectric sensor/actuator network: I. defect detection, localization and growth monitoring. *Smart Materials and Structures*, 16(1):1208–1217, 2007.

[40] J. B. Ihn and F. K. Chang. Pitch-catch active sensing methods in structural health monitoring. *Structural Health Monitoring*, 7(1):5–19, 2008.

[41] M. Lemistre and D. Balageas. Structural helth monitoring system based on diffracted lamb wave analysis by multiresolution processing. *Smart Materials and Structures*, 10(1):504–511, 2001.

[42] S. Grondel, J. Assad, C. Delabarre, and E. Moulin. Health monitoring of a composite wingbox structure. *Ultrasonics*, 42(1):819–824, 2004.

[43] B. Xu and V. Giurgiutiu. Single mode tunning effects on lamb wave time reversal with piezoelectric wafer active sensors for structural health monitoring. *Journal of Nondestructive Evaluation*, 26(1):123–134, 2007.

[44] H. W. Park, H. Sohn, K. H. Law, and C. R. Farrar. Time reversal active sensing for health monitoring of a composite plate. *Journal of Sound and Vibration*, 302(1):50–66, 2007.

[45] G. Konstantinidis, P. D. Wilcox, and B. W. Drinkwater. An investigation into the temperature stability of a guided wave structural health monitoring system using permanently attached sensors. *IEEE Sensors Journal*, 7(5):905–912, 2007.

[46] T. Clarke, F. Simonetti, and P. Cawley. Guided wave health monitoring of complex structures by sparse array sistems: influence of temperature changes on performance. *Journal of Sound and Vibration,* in press, 2009.

[47] P. Fromme. Structural health monitoring of stiffened plates using guided ultrasonic waves. In D. O. Thompson and D. E. Chimenti, editors, *Review of Progress in Quantitative NDE*, volume 28, pages 998–1005. American Institute of Physics, 2009.

[48] K. Worden, C. R. Farrar, G. Manson, and G. Park. The fundamental axioms of structural health monitoring. *Proceedings of the Royal Society A*, 463(1):1639–1664, 2007.

[49] A. J. Croxford, P. D. Wilcox, G. Konstantinidis, and B. W. Drinkwater. Strategies for overcoming the effect of temperature on guided wave structural health monitoring. In *Proceedings of SPIE*, volume 6532, pages 65321T–1 – 65321T–10. SPIE, 2007.

[50] J. E. Michaels and T. E. Michaels. Detection of structural damage from the local temporal coherence of diffuse ultrasonic signals. *IEEE Trans. Ultrason. Ferroelectr. Freq. Control*, 52(10):1769–1782, 2005.

[51] R. L. Weaver and O. L. Lobkis. Diffuse fields in ultrasonics and seismology. *Geophysics*, 71(4):S15–S19, 2006.

[52] A. J. Croxford, P. D. Wilcox, Y. Lu, J. Michaels, and Drinkwater B. W. Quantification of environmental compensation strategies for guided wave structural health monitoring. In *Proceedings of SPIE, Health Monitoring of Structural and Biological Systems II*, volume 6935, pages 69351T–1 – 69351T–10. AIP, 2008.

[53] T. E. Michaels, J. E. Michaels, and A. C. Cobb. Simultaneous ultrasonic monitoring of crack growth and dynamic loads during full scale fatigue tests of

aircraft wings. In D. O. Thompson and D. E. Chimenti, editors, *Review of Progress in Quantitative NDE*, volume 28, pages 1458–1465. Plenum Press, New York, 2009.

[54] T. Cicero, P. Cawley, M. J. S. Lowe, and F. Simonetti. Effects of liquid loading and degradation of adhesive joints on subtraction techniques for structural health monitoring. In D. O. Thompson and D. E. Chimenti, editors, *Review of Progress in Quantitative NDE*, volume 28, pages 1006–1013. Plenum Press, New York, 2008.

[55] R. S. Martin, J. E. Michaels, and T. E. Michaels. Ultrasonic characterization of thermal gradients in a homogeneous plate. In D. O. Thompson and D. E. Chimenti, editors, *Review of Progress in Quantitative NDE*, volume 27, pages 1199–1206. Plenum Press, New York, 2008.

[56] C. W. Wang, J. T. Rose, and F. K. Chang. A synthetic time-reversal imaging method for structural health monitoring. *Smart Mater. Struct.*, 13:415–423, 2004.

[57] J. E. Michaels and T. E. Michaels. Enhanced differential methods for guided wave phased array imaging using spatially distributed piezoelectric transducers. In D. O. Thompson and D. E. Chimenti, editors, *Review of Progress in Quantitative NDE*, volume 25, pages 837–844. Plenum Press, New York, 2006.

[58] P. D. Wilcox, G. Konstantinidis, and B. W. Drinkwater. Structural health monitoring using sparse distributed networks of guided wave sensors. In T. Kundu, editor, *Proceedings of SPIE*, volume 6173, page 6173L, 2006.

[59] A. J. Croxford, P. D. Wilcox, G. Konstantinidis, and Drinkwater B. W. Guided wave shm with a distributed sensor network. In *Proceedings of SPIE*, volume 69350T, pages 69350T–1 – 69350T–10. AIP, 2008.

[60] J. E. Michaels, A. J. Croxford, and P. D. Wilcox. Imaging algorithms for locating damage via in situ ultrasonic sensors. In *Sensors Applications Symposium*, pages 63–67. IEEE, 2008.

[61] T. Clarke, F. Simonetti, S. Rohklin, and P. Cawley. Development of a low-frequency high purity a_0 mode transducer for shm applications. *IEEE Trans. Ultrason. Ferroelectr. Freq. Control*, 56(7):1457–1468, 2009.

[62] T. E. Michaels and J. E. Michaels. Damage localization in inhomogeneous plates using a sparse array of ultrasonic transducers. In D. O. Thompson and D. E. Chimenti, editors, *Review of Progress in Quantitative NDE*, volume 26A, pages 846–853. Plenum Press, New York, 2007.

[63] X. Zhao, H. Gao, G. Zhang, B. Ayhan, F. Yan, C. Kwan, and J. L. Rose. Active health monitoring of an aircraft wing with embedded piezoelectric sensor/actuator network: I. defect detection, localization and growth monitoring. *Smart Mater. Struct.*, 16:1208–1217, 2007.

[64] K. Worden and A. P. Burrows. Optimal sensor placement for fault detection. *Engineering Structures*, 23:885–901, 2001.

[65] H. Gao and J. L. Rose. Ultrasonic sensor placement optimization in structural health monitoring using evolutionary strategy. In D. O. Thompson and D. E. Chimenti, editors, *Review of Progress in Quantitative NDE*, volume 25, pages 1687–1696. Plenum Press, New York, 2006.

[66] H. Y. Guo, L. Zhang, L. L. Zhang, and J. X. Zhou. Optimal placement of sensors for structural health monitoring using improved genetic algorithms. *Smart Mater. Struct.*, 13:528–534, 2004.

[67] N. Hu, T. Shimomukai, H. Fukunaga, and Z. Su. Damage identification of metallic structures using a_0 mode of lamb waves. *Structural Health Monitoring*, 7(3):271–285, 2008.

[68] P. D. Wilcox. Omni-directional guided wave transducer arrays for the rapid inspection of large areas of plate structures. *IEEE Trans. Ultrason. Ferroelectr. Freq. Control*, 50(6):699–708, 2003.

[69] T. Clarke, F. Simonetti, and P. Cawley. Evaluation of a strategy to minimise temperature effects during sparse-array guided wave shm of real complex struc-

tures. In D. O. Thompson and D. E. Chimenti, editors, *Review of Progress in Quantitative NDE*, volume 28, pages 958–965. American Institute of Physics, 2009.

[70] T. Clarke, P. Cawley, P. D. Wilcox, and A. Croxford. Evaluation of the damage detection capability of a sparse-array guided wave shm system applied to a real structure. submitted to *IEEE Trans. Ultrason. Ferroelectr. Freq. Control*, 2009.

[71] M.B. Drozdz. *Efficient finite element modeling of ultrasound waves in elastic media*. PhD thesis, University of London, 2007.

[72] Abaqus documentation. *http://abaqus.cc.ic.ac.uk/v6.5/index.html*, 2009.

[73] G. W. C. Kaye and T. H. Laby. *Tables of Physical and Chemical Constants*. Longman, Essex, England, 1995.

[74] R. Ramesham and R. Ghaffarian. Challenges in interconnection and packaging of micromechanical systems (mems). In *Proceedings of the 50th Electronic Components and Technology Conference*, volume 50, pages 666–675. IEEE, 2000.

[75] M. G. Silk. *Ultrasonic Transducers For Nondestructive Testing*. Adam Hilger Ltd., Bristol, England, 1984.

[76] P. A. Payne. Ultrasonic transducers: design, construction and applications. *International journal of materials and product technology*, 9(4-6):403–427, 1994.

[77] V. Giurgiutiu. Tuned lamb wave excitation and detection with piezoelectric wafer active sensors for structural health monitoring. *Journal of Intelligent Material Systems and Structures*, 16(4):291–305, 2005.

[78] M. J. S. Lowe, P. Cawley, J. Y. Kao, and O. Diligent. The low frequency reflection characteristics of the fundamental antisymmetric lamb wave a_0 from a rectangular notch in a plate. *J. Acoust. Soc. Am.*, 112(6):2612–2622, 2002.

[79] O. Diligent, T. Grahn, A. Boström, P. Cawley, and M. Lowe. The low-frequency reflection and scattering of the s_0 Lamb mode from a circular through-thickness hole in a plate: Finite element, analytical and experimental studies. *J. Acoust. Soc. Am.*, 112(6):2589–2601, 2002.

[80] O. Diligent, M. J. S. Lowe, P. Cawley, and P. Wilcox. Reflection of the s_0 lamb mode from a part-depth circular defect in a plate when the incident wave is created by a small source. In D. O. Thompson and D. E. Chimenti, editors, *Review of Progress in Quantitative NDE*, volume 22, pages 197–204. American Institute of Physics, 2003.

[81] A. Demma, P. Cawley, and M. Lowe. Scattering of the fundamental shear horizontal mode from steps and notches in plates. *J. Acoust. Soc. Am.*, 113(4):1880–1891, 2003.

[82] Y. Lu and J. E. Michaels. A methodology for structural health monitoring with diffuse ultrasonic waves in the presence of temperature variations. *Ultrasonics*, 43(9):717–731, 2005.

[83] O. I. Lobkis and R. L. Weaver. Coda-wave interferometry in finite solids: Recovery of p-to-s conversions rates in an elastodynamic billiard. *Physical Review Letters*, 90(1):254302–1 – 254302–4, 2003.

[84] P. M. Sutton. The variation of the elastic constants of crystalline aluminum with temperature between 63°k and 773°k. *Physical Review*, 91(4):816–821, 1953.

[85] R. W. Hill. The elastic behaviour of a crystalline aggregate. *Proceedings of the Physical Society of London*, A65:349–354, 1952.

[86] O. L. Anderson. *Physical Acoustics*, volume IIIB. Academic, New York, 1965.

[87] S. I. Rokhlin. An ultrasonic bridge for the study of viscoelastic properties of thin interface films. *J. Acoust. Soc. Am.*, 73:1619–1623, 1983.

[88] P. J. Torvik. Reflection of wave trains in semi-infinite plates. *J. Acoust. Soc. Am.*, 41(2):346–353, 1967.

[89] J. Zhang, B. W. Drinkwater, and P. D. Wilcox. Defect characterisation using an ultrasonic array to measure the scattering coefficient matrix. *IEEE Trans. Ultrason. Ferroelectr. Freq. Control*, 55(10):2254–2265, 2008.

[90] J. Davies. *Inspection of pipes using low frequency focused guided waves.* PhD thesis, University of London, 2008.

List of Publications

[P1] T. Clarke, F. Simonetti and P. Cawley. Guided wave health monitoring of complex structures by sparse array sistems: influence of temperature changes on performance. Journal of Sound and Vibration. In press.

[P2] T. Clarke, F. Simonetti, S. Rohklin and P. Cawley. Development of a low-frequency high purity A0 mode transducer for SHM applications. IEEE Trans. Ultrason. Ferroelectr. Freq. Control. vol. 56 (7), 2009, pp. 1457-1468.

[P3] T. Clarke, P. Cawley, P. Wilcox and A. Croxford. Evaluation of the damage detection capability of a sparse-array guided wave SHM system applied to a real structure. Submitted to IEEE Trans. Ultrason. Ferroelectr. Freq. Control.

[P4] T. Clarke, F. Simonetti, S. Rohklin and P. Cawley. Evaluation of the temperature stability of a low frequency A0 mode transducer developed for SHM applications. In D. O. Thompson and D. E. Chimenti, editors, *Review of Progress in Quantitative NDE*, volume 27A, pages 910-917. American Institute of Physics, Melville, New York, 2008.

[P5] T. Clarke, F. Simonetti and P. Cawley. Evaluation of a strategy to minimise temperature effects during sparse-array guided wave SHM of real complex structures. In D. O. Thompson and D. E. Chimenti, editors, *Review of Progress in Quantitative NDE*, volume 28, pages 958-965. American Institute of Physics, Melville, New York, 2009.

[P6] T. Clarke and P. Cawley. Monitoring of Complex Structures using Guided Waves. In T. Uhl, W. Ostachowicz and J. HolnickiSzulc, editors, *4th European Workshop on Structural Health Monitoring*, volume 4332, pages 673 - 681. Destech Publications, Inc., 439 Duke Street, Lancaster, PA 17602-4967 USA, 2008.